Journal of Materials Chemistry A

REVIEW

View Article Online
View Journal | View Issue

Cite this: J. Mater. Chem. A, 2019, 7, 23679

Real-time monitoring of stress development during electrochemical cycling of electrode materials for Li-ion batteries: overview and perspectives

Manoj K. Jangid and Amartya Mukhopadhyay *

One of the major issues associated with Li-ion batteries is the stress development in electrode materials. Such stresses arise primarily from dimensional changes, structural/phase transformations and development of Li-concentration gradients in electrode materials during electrochemical cycling. These cause drastic fade in the Li-storage capacity due to fracture/disintegration of the electrodes, especially those which possess greater Li-storage capacity. They also negatively influence some of the other electrochemical performances, such as voltage hysteresis and kinetics of Li-storage. Accordingly, such stresses lead to compromise in the energy density, power density and cycle stability of Li-ion batteries. However, evaluating and understanding the above electro-chemo-mechanical aspects *via ex situ* experiments are neither feasible nor reliable, because the stress state depends critically on the state-of-charge (*viz.*, Li-content) and the surrounding conditions of the concerned electrode. Thus, *in situ* experiments are needed for evaluating/understanding them and eventually addressing them in comprehensive terms. In this context, over the last decade, extensive efforts have been directed towards measuring/monitoring the stress development in different electrode materials/types/architectures in real-time during electrochemical cycling. For the same, the more commonly used techniques have been based on a substrate curvature methodology, which allows fairly direct measurement of the stresses. Additionally, a host of other *in situ* techniques have been employed, which provide valuable

Received 17th June 2019
Accepted 5th September 2019

DOI: 10.1039/c9ta06474e

rsc.li/materials-a

High Temperature and Energy Materials Laboratory, Department of Metallurgical Engineering and Materials Science, Indian Institute of Technology Bombay, Mumbai, India. E-mail: amartya_mukhopadhyay@iitb.ac.in; Tel: +91-22-25767612

Presently, a research scholar (pursuing PhD) at the Department of Metallurgical Engineering and Materials Science, Indian Institute of Technology (IIT) Bombay, India, Manoj K. Jangid received his Bachelors' and Masters' degrees (with honours) in 'Nanotechnology and Nanomaterials' in 2012 from the Centre for Converging Technologies, University of Rajasthan, India. As a Masters' student, he conducted research, as part of his Master's dissertation, at CSIR-National Chemical Laboratory, India, in the area of organic field effect transistors. His current areas of research include understanding the stress developments in electrode materials, development-cum-understanding of high performance electrode materials for Li-/Na/K-ion and Li–S batteries and interface engineering.

Presently, Associate Professor at the Department of Metallurgical Engineering and Materials Science, IIT Bombay, India, Amartya Mukhopadhyay completed his Doctoral in Materials research from the University of Oxford, UK, in 2009. He performed his post-doctoral Research at Brown University, USA, for a couple of years. His research interests include materials for electro-chemical energy storage and engineering ceramics. Among his major recognitions so far, he has been awarded with the 'INAE Young Engineer Award 2016', 'ASM-IIM North America Visiting Lectureship 2016', 'IIT Bombay Young Investigator Award 2014' and 'Dr R. L. Thakur Memorial Award' (as Young Scientist) by the 'Indian Ceramic Society' in 2013.

complementary information on the electrode strains/stresses. The success of all the above has led to some vital understandings on the electro-chemo-mechanical aspects, which now enable the development of electrode architectures possessing enhanced integrity upon repeated electrochemical cycling. In this context, the present review introduces the types and mechanistic aspects of the concerned stresses for the first time. This is followed by details on the *in situ* monitoring of the stress development *via* variants of the substrate curvature methodology, focussing on the mechanistic aspects and different anode/cathode materials, as well as electrode architectures. The complementary information obtained from other *in situ* techniques is then discussed, which is followed by discussion on the inferences obtained on aspects other than the integrity of the electrodes. Finally, some of the aspects/issues that need further attention have been discussed, while summarizing the important information obtained so far from such *in situ* studies.

1. Introduction

The ever increasing environmental pollution and depletion of fossil fuels necessitate sustained usage of renewable energy sources for the production of electricity and development of electric vehicles. The above, coupled with increased demand for sophisticated consumer electronic devices, renders it imperative to develop advanced electrochemical energy storage technologies. Among the various electrochemical energy storage technologies that are presently in use, Li-ion batteries possess the highest energy density; *i.e.*, the capability to store more energy per unit mass or volume. Nevertheless, the other important criteria towards successful usage in 'advanced' or 'heavy duty' applications (such as electric vehicles or grid/renewable energy storage) include enhanced stability over multiple discharge/charge cycles (*i.e.*, cycle life) and the ability to take-up/release energy at a rapid rate (*i.e.*, power density). In other words, the capacity or energy density of a battery needs to be maintained over many repeated charge/discharge cycles, sometimes under stringent operating conditions that include very fast charge/discharge rates (more precisely, at high current densities).

In this regard, one of the major reasons for 'cycle instability' or rapid reduction of Li-storage capacity upon repeated cycling is the stress development and concomitant fracture/disintegration of the active electrode materials.[1–4] Such stresses arise primarily from dimensional changes (along with concentration gradients), structural changes, phase transformations and undesirable surface reactions that take place during insertion/removal of the 'guest' Li-ions into/from the 'host' electrode structures/lattices.[1–27,30] Such stresses are particularly severe in the cases of higher capacity electrode materials (*viz.*, those which can host more Li per unit mass per volume) and at faster charge/discharge rates.[1–6,8,9,11–13,15,16,27–32] Accordingly, not only do the stresses reduce the cycle life for most of the electrode materials used, but also render the successful usage of very high capacity electrode materials (such as Si or Sn based anodes) difficult, thus leading to compromise on the energy density, as well. Additionally, the structural instabilities, stress development and concomitant degradations limit the current densities (that is the charge/discharge rates and concomitantly, the power densities) and also in some cases limit the practically useable capacities (*viz.*, the maximum amount of Li that can be inserted/removed without causing instability).[1–4,33–38] On a different note, the inability to use 'alloying reaction' based anode materials, such as Si and Sn, due to the above stress related issues necessitates the continued usage of graphitic carbon based anode materials, which is a compromise on the safety aspects of Li-ion cells.

Accordingly, there have been extensive efforts over the last couple of decades across various research groups world-wide to understand the causes, magnitudes and evolution patterns of such stresses under various conditions and minimize the same (or at least the associated negative impacts) *via* innovative materials/electrode designs and optimization of the electrochemical cycling conditions.[39–47] However, basic electrochemical characterization methods and basic structural/morphological characterization methods alone are not sufficient to lead to in-depth understanding of the mechanistic aspects associated with the various phenomena occurring during electrochemical cycling of electrode materials (*viz.*, charge storage mechanism, phase/structural/dimensional changes, stress development, side-reactions, reaction kinetics *etc.*). Accordingly, in-depth understanding of the interrelations between the complex processes involving electrode structure/composition – electrochemical phenomena, Li-concentration profiles, phase assemblage/transformation, structural changes, stress development, impact of such stresses – could only be achieved upon development of technique(s) that can monitor the dimensional/structural changes and stress development in the electrode materials in real-time (*i.e.*, *in situ*) during electrochemical cycling. The techniques that have been used more commonly for the real-time monitoring of stress development during electrochemical cycling have been based on the substrate curvature methodology, in various forms,[1,6,22,48–50] which have been applied to simple film electrodes and the more usual 'porous composite' electrodes (*viz.*, those having binders and conducting additives).[5,27,32] Such *in situ* investigations have provided first-hand information on the magnitudes of stresses, behavioral patterns of stress development and associated integrities of electrodes as functions of state-of charge, electrochemical conditions and number of cycles.[5–7,11–13,17–20,22,23,27,30–32,50–56] Furthermore, various other important information-cum-understandings, especially those related to Li-diffusivity, structural/phase changes, electrochemical potential, voltage hysteresis *etc.*, have also been obtained from such studies.[6,17,26,30,57–75] Overall, the results and inferences based on these innovative research studies are

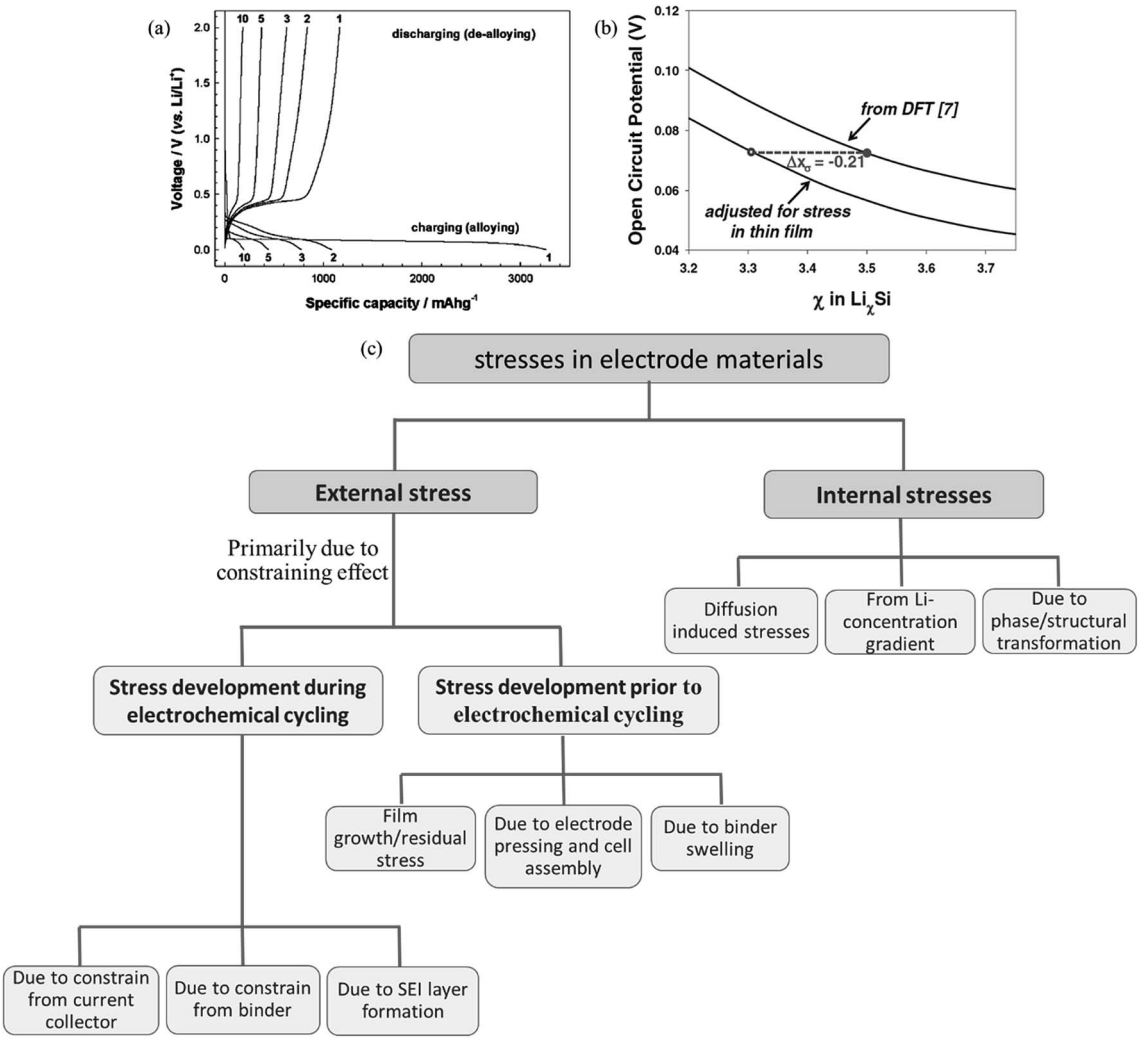

Fig. 1 Voltage *vs.* capacity profiles obtained during galvanostatic cycling of Si in a Li 'half cell' for the 1st, 2nd, 3rd, 5th and 10th cycles, showing drastic fade in the Li-storage capacity.[8,262] (Reproduced with permission.[262] Copyright 2004, The Electrochemical Society). (b) Drop in the open circuit potential (OCV) at a given state-of-charge due to the presence of stress in the electrode (here Si film) (reproduced with permission.[58] Copyright 2011, The Electrochemical Society). (c) Flow diagram depicting the types and origin of stresses in electrodes for Li-ion batteries and beyond.

already contributing immensely towards the development of electrode materials and engineering of electrode/electrolyte interfaces for achieving considerably enhanced cycle stability and power density.

In the above context, after this brief introduction to the importance and scope of the associated research (as in Section 1), Section 2 discusses in detail the mechanistic aspects concerning the development of stresses in electrode materials, including the effects of electrode composition, structure, state-of-charge, phase/structural transformations and electrochemical parameters towards stress development. Following this, Section 3 elucidates the basic principles and assumptions underlying the substrate curvature methodology for stress measurement, which is the methodology more commonly used for monitoring the stress development in electrodes. The concerned experimental set-ups developed have also been described, highlighting their suitability, advantages and drawbacks. Sections 4 and 5 provide detailed surveys of the literature concerning monitoring of stress development during electrochemical lithiation/delithiation of various electrode materials for Li-ion batteries and beyond (sub-divided as anode and cathode materials). Subsequently, Section 6 discusses the interesting aspects associated with stress development due to irreversible surface phenomena, involving solvated-ion intercalation and the formation of the irreversible surface 'passivation' layer (called the solid electrolyte interface or SEI). Section 7 presents a discussion on the complementary information provided by the other types of *in situ* investigations conducted during electrochemical cycling, highlighting the comprehensive understanding on the electro-chemo-mechanical aspects of electrodes which have been made possible by a combination of results and inferences obtained from all such investigations. Subsequently, *i.e.*, in Section 8, the additional inferences beyond stresses and electrode integrity which have been

obtained from such *in situ* studies, *viz.*, in terms of mass transport, electrode/electrolyte interfaces, electrochemical processes and phase transformations, will be discussed. Finally, Section 9 summarizes the important findings and understandings developed based on such innovative research, while pointing out the grey areas that necessitate further attention.

2. Stress development in electrode materials

As introduced briefly in the previous section, stress development in electrode materials is a major issue because it not only leads to drastic fade in the capacity during electrochemical cycling due to cracking/disintegration of the electrodes (see Fig. 1a), but also influences the basic electrochemical behavior (such as suppressing Li-transport and enhancing hysteresis loss) (see Fig. 1b). These issues will be further discussed with the help of relevant examples in the subsequent sections. Additionally, upon pulverization due to stresses, the newly formed 'active' electrode particles cause 'microstructural inhomogeneity' within the electrode, which, in turn, leads to non-uniformity in the current/charge density across the electrode; *viz.*, the charge/current density being higher at pointed/sharp edges. These often lead to a differential local state-of-charge (SOC), non-uniform accumulation of stress/strain, over-charging, Li-plating *etc.*

In the present section, the causes for stress development will be introduced in a fairly generic sense. These will again be revisited in the subsequent sections focused on the real-time measurements and concomitant understanding of various aspects of such stresses. The mechanistic aspects associated with stress development in a generic sense, as well as with respect to typical scenarios for different electrode materials, have been discussed in more comprehensive terms in other review articles, focused primarily on the above.[1,3,39]

2.1. Classification of electrode stresses

Broadly, based on the origin, the stresses in electrode materials can be classified as 'external stresses' or 'internal stresses' (see Fig. 1c). The 'external stresses' arise primarily due to constraining effects of the surroundings (*viz.*, other electrode particles, current collector, binder *etc.*) towards changes in dimensions. These may be further sub-divided into two sub-categories based on when they get developed; *viz.*, (i) prior to electrochemical cycling and (ii) during electrochemical cycling. By contrast, the 'internal stresses' include stresses due to the Li-concentration gradient, occurrence of structural changes and phase transformations, which typically occur during electrochemical cycling (*i.e.*, Li-insertion/removal).

2.2. Stresses due to the constraining effect or 'external stresses'

2.2.1. Stress development during electrochemical cycling. Battery electrodes are either in the form of a uniform dense film of active electrode materials deposited/coated on the current collector (usually, Cu or Al foil/film) or in the form of a 'porous composite' having particles of the active material, along with some conducting additive (such as carbon black) and polymeric binder (such as PVDF, CMC, and Na-alginate), prepared by casting the associated slurries on the current collector. In addition to connecting the electrode to the external circuit, the current collector also acts as a support for the active electrode film.

During Li-insertion, the volume of most electrode materials either increases (as for graphitic carbon, Si Sn, Ge *etc.*)[1–4,6,8–10,12,15,16,18,20,22,31,32,67,76] or decreases[1,24,27,33–38] (as for $LiCoO_2$, $LiNi_xMn_yCo_{1-x-y}O_2$ *etc.*), of course, in varying degrees depending on the material under consideration and the progress of lithiation. The reverse takes place during Li-removal, and the change may or may not be fully reversible.[11,15–17,31,77–79] However, the other 'inactive' components of the electrode, such as the underlying current collector or the binder, provide constraint to the aforementioned dimensional changes of the 'active' electrode particles/films. In the case of particle-based 'porous composite' electrodes, the surrounding 'active' particles also constrain the increase in volume when they come into contact with each other during dilation. All the above lead to the development of stresses in the 'active' electrode materials.[1,11,15,18,22,31,67]

In addition to constraining effects from the current collector, binder and surrounding particles, irreversible surface phenomena taking place on the electrodes during the initial lithiation/delithiation cycles, *viz.*, SEI layer formation, also contribute to stress development in the electrodes.[20,21,53,54,80–82] SEI layer formation can be considered akin to electrochemical deposition of a 'film' on a 'substrate', with the SEI layer being the 'film' here and the electrode the 'substrate'. Accordingly, the stress development due to SEI layer formation can be comprehended in terms of the 'growth stresses' occurring during film deposition.[21,48,83]

2.2.2. Stress development prior to electrochemical cycling. While the above 'external stresses' get developed during electrochemical cycling, the as-prepared electrodes themselves, to start with, may also not be free from stresses that may get developed prior to electrochemical cycling, *viz.*, during electrode preparation, cell assembly and initial conditioning. In the case of film electrodes, where the 'active' electrode films are directly deposited onto the current collector (also acting as the substrate), usually at temperatures higher than the ambient temperature, 'growth' (or residual) stresses are likely to get developed due to mismatch in the lattice parameters and co-efficient of thermal expansion between the 'active' material and the substrate.[17,22,48,55,83] Additionally, in the case of 'porous composite' electrodes, even though not usually considered, the process of casting of the electrode slurry, followed by drying and pressing (typically by passing the electrode in-between two rollers), is also likely to lead to some built-in 'residual' stresses. Of note are the reported observations concerning the adoption of a strong (003) texture by $LiCoO_2$ particles in such electrodes after the pressing step.[33,84]

Another source of stress development during cell assembly or conditioning is the swelling of the polymeric binder polymer, when soaked in the electrolyte. Such irreversible swelling can

increase the volume of the binder by 50% upon absorption of the electrolyte.[85] In this context, even though often neglected, Sethuraman *et al.*[27] experimentally measured a compressive stress of ~(−)2 MPa associated with binder swelling. In this review (−) denotes compressive stress, while (+) denotes tensile stress.

2.3. The 'internal stresses'

During Li-insertion/removal into/from the active electrode particles/films, Li-concentration gradients get developed within the particle/film, which tend to become more non-uniform/steeper with the increase in particle size (or film thickness), increase in current density used for electrochemical lithiation/delithiation (*i.e.*, C-rate) and decrease in Li-diffusivity of the electrode material. In general, during the progress of lithiation, the Li-concentration decreases from the outer surface to the core of the 'active' electrode particle (or from the film surface to the film/current collector interface in the case of a film electrode). If volume expansion takes place during lithiation, the molar volume of the outer lithiated 'shell' becomes greater, as compared to the relatively 'unlithiated' core. This leads to a situation where different regions within the same particle/film (*i.e.*, continuum) possess molar volumes. In such a scenario (neglecting the occurrence of any real phase transformation, say as for amorphous Si), the outer surface is likely to experience compressive hoop stress, whereas tensile hoop stress is likely to get developed in the interior of the particle. By contrast, in the case of two-phase lithiation, as in the case of crystalline Si, where both the lithiated and unlithiated regions are separated by a sharp reaction front, it was found that the outer lithiated shell and the unlithiated core experience tensile hoop stress and compressive hoop stress, respectively.[61,86,87] Overall, the development of such 'diffusion induced stresses' during lithiation/delithiation not only depends on the Li-diffusivity and molar volumes of the lithiated and unlithiated regions, but also on the occurrence/non-occurrence of phase transformation, crystallographic orientation, particle/electrode form/shape/dimension, electrode porosity *etc.* Nevertheless, a fairly good understanding of such 'internal stresses' has been obtained due to the modelling efforts by various groups worldwide.[1,13,39,88–93] As mentioned upfront, the severity of such a diffusion induced stress increases with the decrease in Li-diffusivity and increase in the C-rate, which has also been demonstrated for different electrode materials, such as Si-based anode[13] and $LiMn_2O_4$-based cathode[28] materials.

Another source of the development of 'internal stresses' is the change in the structure and phase during Li-insertion/removal into/from crystalline electrode materials. In the case of occurrence of nucleation-growth induced 1st order phase transformations, the formation of a new phase, having a different molar volume with respect to the parent phase, within the volume of the parent phase, leads to the development of Eigen strain. The magnitude of this Eigen strain increases with the difference in the molar volume between the new and parent phases. It is this Eigen strain which is the source of the 'internal stress' in the new, as well as the parent, phase and leads to mechanical instability, including plastic deformation and fracture.[18,19,24,55] Furthermore, sharp changes in the structure, mechanical properties (primarily, stiffness) and Li-concentration across the interface between the new and parent phases also cause preferential build-up of the stress at the interface during the progress of the phase transformation front. In fact, in electrode materials that are lithiated/delithiated *via* the propagation of the phase transformation front, mechanical instability, including cracking, has been noted primarily close to the interface between the new and parent phases.[94–97]

3. Substrate curvature method for monitoring stress development in real-time

3.1. Basic principle, Stoney's equation and associated modifications

In the case of a film–substrate system, if there is a change in the dimension of the film with respect to the substrate, provided the adhesion at the film/substrate interface is maintained, a curvature is induced in the system. This is because the substrate tries to constrain the relative dimensional change of the film, in turn, causing stress development in the same. In such a case, without even disturbing or probing the active film, if the change in the radius of curvature of the substrate (R) is measured, the in-plane bi-axial stress in the film (σ) can be estimated based on Stoney's equation;[98] the basic form of which is mentioned in the following:

$$\sigma = \frac{E h_s^{\,2}}{6(1-\nu)\, h_f R} \tag{1}$$

where, E, h_s and ν are the Young's modulus, thickness and Poisson's ratio of the substrate, respectively, and h_f is the thickness of the film.

There are certain assumptions involved in the above 'Stoney's equation', with the most important ones being mentioned below. More details concerning the formulation of the equation and the assumptions can be found elsewhere, such as in ref. 83 and 98–100. The above equation is valid only when the thickness of the film (h_f) under consideration is less than the thickness (h_s) of the substrate, with both being less than the radius (or the in-plane dimension, r) of the substrate/film, *viz.*, $h_f \ll h_s \ll r$. Furthermore, both the film and substrate should remain elastic during the course of the measurement. Later in this article (*i.e.*, in sections 4 and 5), the deviations that occur when the film undergoes plastic deformation will be discussed, with examples. Finally, for very reliable estimation of the film stresses based on eqn (1), the film needs to be void/pore free and the dimensional changes should be isotropic.

Stoney's equation, in this original form, was extensively used for *ex situ* and *in situ* measurements of stresses developed during the deposition/growth of films on substrates, including *via* physical vapor deposition and electrodeposition.[48,98] For the systems under consideration here, *viz.*, electrochemical Li-insertion/removal into/from active electrode materials, if the

dimension of the electrode changes as a function of the Li-content/state-of-charge, while the 'inactive' substrate (which also includes the current collector) provides constraint to the same, the curvature of the film–substrate system changes with the progress of Li-insertion/removal. As a more specific example, during lithiation of a Si film present on a thicker stiff substrate, the dilation of the Si film gets constrained by the substrate, causing the development of compressive stress in Si and the substrate curvature to become concave. The reverse takes place during delithiation, depending on the extent of reversibility of lithiation, occurrence of any irreversible side reaction and also change(s) in the nature/properties of the film during lithiation/delithiation. More detailed discussion on these aspects, with examples,[5–7,11–13,17,30,31,49,50,66,87,101–103] will be provided in sections 4–6.

While the basic Stoney's equation [*i.e.*, eqn (1) here] is directly applicable to simple thin film electrode systems, it has been modified to render it better suited to the bulkier 'porous composite' electrode architecture consisting of a binder and conducting additive, in addition to particles of the active material. For such a 'porous composite' electrode architecture having multiple constituents and also porosity, one of the forms of the modified Stoney' equation that has been used for estimating the in-plane stress (σ) from the substrate curvature can be written as[104]

$$\sigma = \frac{M_s {h_s}^2}{6 h_f R f(h_i, M_i)} \tag{2}$$

$$f(h_i, M_i) = \left(1 + \frac{h_f}{h_s}\left[1 + 4\frac{h_f}{h_s}\frac{M_f}{M_s} + 6\frac{{h_f}^2}{{h_s}^2}\frac{M_f}{M_s} + 4\frac{{h_f}^3}{{h_s}^3}\frac{M_f}{M_s} + \frac{{h_f}^4}{{h_s}^4}\frac{{M_f}^2}{{M_s}^2}\right]\right)^{-1} \tag{3}$$

$$M_f = \frac{E_f}{1-\nu_f} = \frac{\varnothing_{electrode} E_{electrode} + \varnothing_b E_b + \varnothing_c E_c}{1 - (\varnothing_{electrode} \nu_{electrode} + \varnothing_b \nu_b + \varnothing_c \nu_c)} \tag{4}$$

where M_s is the biaxial modulus of the substrate [*i.e.*, $E/(1-\nu)$], h_s is the thickness of the substrate (usually a thicker stiff substrate on which the current collector foil is attached), h_f is the thickness of the active film, M_f is the biaxial modulus of the composite film, E_f is the Young's modulus of the composite film, ν_f is the Poisson's ratio of the composite film, $f(h_i,M_i)$ is a factor developed for estimation with such thick composite electrodes, $\varnothing$ is volume fraction, ν is Poisson's ratio, and subscripts b and c stand for the binder and conductive additive, respectively.

Again, while eqn (1) pertains to continuous (void/pore free) thin films, in case the film architecture is in the form of regular (patterned) islands, modifications need to be done to the basic Stoney's equation for obtaining more valid stress measurements. In this context, the expression for substrate curvature κ (*i.e.*, $1/R$) for a film composed of three dimensional circular patterns (or 'islands') can be written as;[49]

$$\kappa = \frac{6\,\tau_0 r\,(1-\nu_s)}{E_s {h_s}^2} \frac{\pi r^2}{4(r+s)^2}\left(\frac{1}{3} - \frac{\tilde{r}_p^{\,3}}{3}\right)\mathrm{sign}(\sigma_f) \tag{5}$$

where τ_0 is the interfacial sliding strength of the substrate, r is the radius of the circular pattern/island, ν_s is the Poisson's ratio of the substrate, E_s is the Young's modulus of the substrate, h_s is the substrate thickness, s is half of the gap between two patterns/islands, and r_p is the radial distance from the edge of the pattern to the point where $\tau_{int}(x)$ becomes equal to τ_0. For another architecture of the patterned film, *viz.*, three dimensional square patterns/islands having length $2l$, the expression

Table 1 Comparisons between the laser beam position detector (LBPS; cantilever-based) and multi-beam optical stress sensor (MOSS) methods of measurement of in-plane stress in the film *via* measurement of the substrate curvature

Laser beam position detector (LBPS) or cantilever method	Multi-beam optical stress sensor (MOSS)
Geometry of the film–substrate system is rectangular (as for a cantilever)	Geometry of the film–substrate system is usually circular
The cantilever is fixed at one end while the other end remains free for deflection/bending upon changes in the in-plane dimension(s) of the film w.r.t. the substrate	The film–substrate system is simply placed without additional support (or fixing), such that the entire circular film–substrate system is free to bend and, thus, usually experiences uniform curvature development upon changes in the in-plane dimension of the film w.r.t. the substrate
It is usually based on single point illumination and detection, *viz.*, only one laser beam is focused onto and deflected from the back side of the substrate. Thus, measurements made using this methodology can be sensitive to mechanical vibrations, leading to possible errors/artefacts	It is usually based on multi-point illumination and detection, *viz.*, multiple laser beams are focused onto and deflected from the back side of the substrate. Thus, measurements made using this methodology have almost negligible sensitivity to mechanical vibrations
The reflected laser beam is detected by a laser beam position detector (LBPS)	The reflected laser beam is detected by a CCD camera, which is passed onto the associated software as laser 'spots'. It is the change in spacing between the multiple reflected spots (and not the position of a single laser beam/spot), which is monitored in order to obtain a reliable estimate for the associated change in the substrate curvature
The rectangular geometry and the fixture at one end may sometimes lead to uneven change in curvature along the length of the cantilever, which may render the estimation of the change in the substrate curvature (and the associated stress) a bit more complex	Due to the circular geometry of the film–substrate system, the change in the curvature is usually uniform in all the 'in-plane' directions
For reliable estimation, the deflection of the cantilever has to be smaller than the length of the cantilever	The change in curvature (and not truly deflection) of the film–substrate system is of interest here, where such limitations associated with the magnitude of change are not stringent

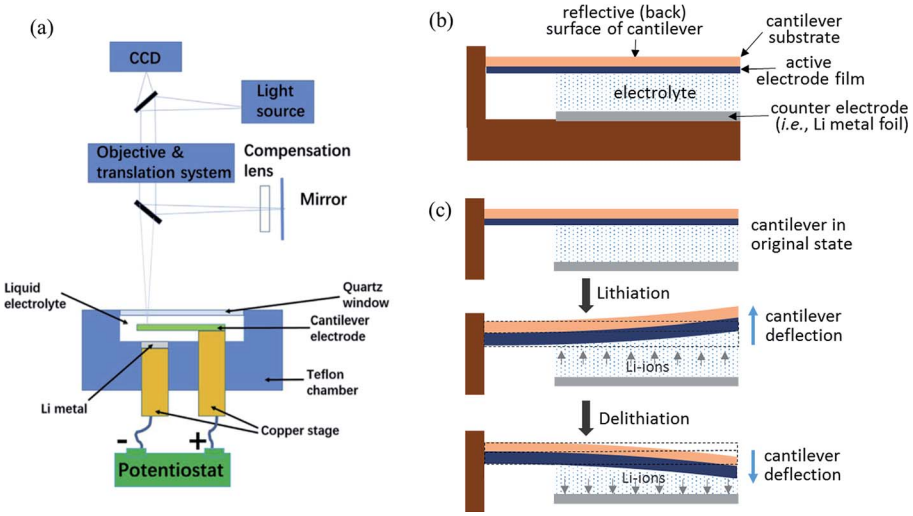

Fig. 2 Schematic illustrations of the (a) set-up used for *in situ* monitoring of the stress development in electrodes *via* the cantilever method. Overall, it consists of a light interferometry set-up and a custom-made electrochemical cell (which contains the active electrode mounted on a cantilever), connected to a galvanostat/potentiostat (reproduced with permission.[105] Copyright 2018, Elsevier); (b) custom-made electrochemical cell showing the different components; (c) deflection caused in the cantilever during the lithiation and delithiation processes.

for substrate curvature κ for the modified Stoney's equation can be written as[49]

$$\kappa = \frac{6\tau_0 R_{eq}\,(1-\nu_s)}{E_s {h_s}^2}\left(\frac{l}{l+s}\right)^2\left(\frac{1}{3}-\frac{\tilde{r}_p^{\,3}}{3}\right)\mathrm{sign}(\sigma_f) \qquad (6)$$

where R_{eq} is the equivalent radius of the pattern/island, such that $R_{eq} = l\tilde{R}_{eq}(\tilde{\sigma}_f)$, with all the other symbols retaining the meanings as defined earlier.

3.2. The commonly used techniques based on the substrate curvature method

The more commonly used techniques for measuring the film stress based on the curvature method invoke the deflection (*viz.*, change in the angle of reflection) of laser beam(s) reflected from the back side of the substrate to gauge the change in the curvature of the film–substrate system upon dimensional change of the film with respect to the substrate. This is particularly useful in the context of measuring/monitoring the stress development in electrode materials upon/during electrochemical lithiation/delithiation because the 'active' film side remains in contact with the electrolyte. On the basis of the methodology used for the detection of deflected beam(s) by a detector, the number of laser beams focused on the back side of the substrate (*viz.*, single or multiple) and the concerned geometry of the film–substrate system, the techniques can be further classified into two sub-categories as discussed in the following text. The two curvature based techniques have been compared and contrasted, in explicit terms, as shown in Table 1.

3.2.1. Laser beam position detector (LBPS) or cantilever method. In this technique, the change in the curvature of the film–substrate system (*i.e.*, electrode), in the form of a cantilever, is measured using a laser light interferometry set-up (as shown in Fig. 2a). This technique usually uses a single laser beam focused onto and reflected from the back side of the substrate, whose deflection (or change in position) is detected. Of course, in the case of *in situ* monitoring of stress development in electrodes during electrochemical cycling, custom-designed electrochemical cells are used (as shown in Fig. 2a). In general, such a electrochemical cell has an outer wall made of stainless-steel or Teflon and has a suitable position for a reference/counter electrode (usually Li-metal placed at the bottom) and a working electrode mounted on a rectangular cantilever. Both the electrodes are placed as close to each other as possible, but with due care to avoid short-circuiting, usually by the use of a separator. The back surface of the cantilever, which faces a properly designed optical window, is made reflective in order to facilitate the reflection of the incident beam. One end of the cantilever is fixed with a rigid support while the other end remains free for movement/deflection (see Fig. 2a and b). An optical window of quartz provides the passage to the incident and reflected light beam in and out of the electrochemical cell. The entire cell assembly is made in a controlled atmosphere (*i.e.*, in an inert atmosphere, with oxygen and moisture contents below ~1 ppm) and properly sealed using O-rings and screws.

During the lithiation/delithiation cycle, the dimensions of the electrode change, which, however, gets constrained by the rigid substrate. In the case of in-plane dilation of the electrode film, upward bending of the cantilever (*i.e.*, away from the reference/counter electrode) takes place (see Fig. 2c). The reverse takes place in the case of in-plane contraction of the electrode film. The change(s) in position of the laser beam reflected from the back-side of the substrate, as detected by the LBPS, is used to gauge the change in substrate curvature (and, accordingly, the stress in the active electrode material). The use of this *in situ* technique during electrochemical cycling has led to significant contributions towards the understanding of chemo-mechanical stress responses in various electrode

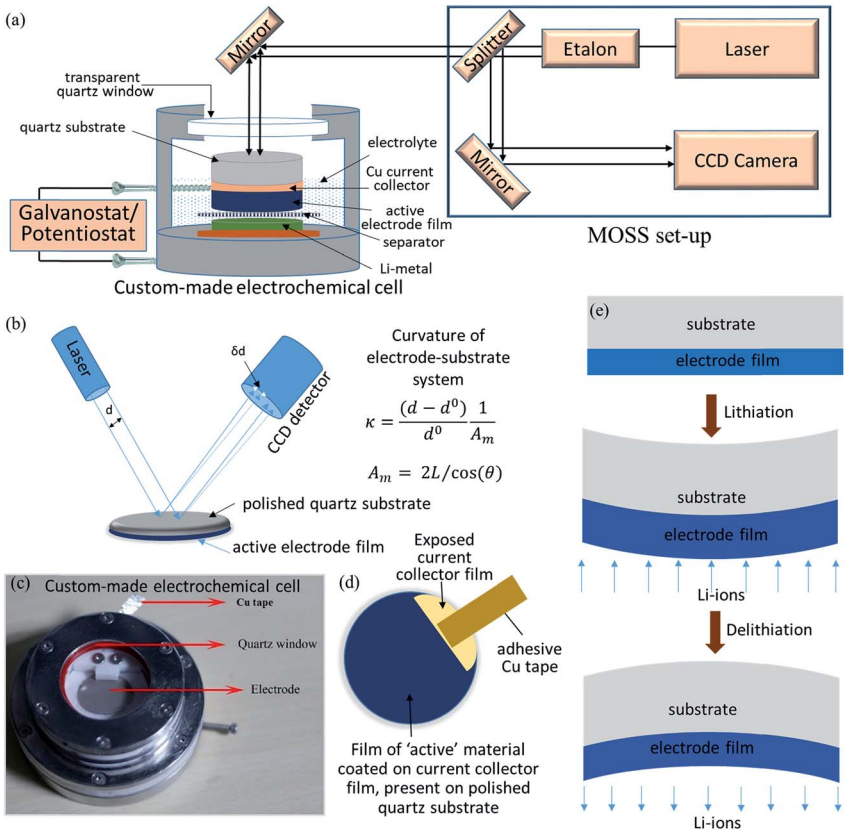

Fig. 3 Schematic representations of the (a) experimental set-up consisting of the multi-beam optical stress sensor (MOSS) and custom-made electrochemical cell, as connected to a potentiostat/galvanostat, for monitoring the stress development in electrodes *in situ* during electrochemical cycling; (b) ray-diagram showing the incident laser beam, which is focused onto and reflected back from the polished (back) surface of the quartz wafer and collected by the CCD camera. The relations used for estimation of the curvature of the electrode–substrate system based on the concerned geometry have also been presented. (c) Digital photograph of one of the types of custom-made electrochemical cells used for the *in situ* stress measurements. Schematic representations of the (d) electrical connection to the electrode, as aided by a Cu tape attached to the partially exposed current collector film present in-between the substrate and the active electrode film and (e) evolution of the curvature of the electrode–substrate system during lithiation and delithiation processes.

materials,[5,6,11,18,20,22,23,30,51,66,76] including measurements of the associated dimensional changes (*i.e.*, strain),[105] estimation of 'electrochemical stiffness' *via* simultaneous measurements of stress–strain[106] and also inferences on electro-deposition/stripping of Mg on/from a Mg metallic electrode as the anode material for upcoming Mg-ion battery systems.[107]

3.2.2. Multi-beam optical stress sensors (MOSSs). As developed by researchers at Brown University,[48] USA, a multi-beam optical stress sensor (MOSS) uses more than one laser beam, *i.e.*, an array of parallel laser beams, focused onto the reflective back side of the substrate. In this system, it is the change in spacing of the reflected beams, as captured using a CCD camera in the form of laser 'spots', which is measured/monitored for estimating the change in substrate curvature, and accordingly, the stress in the film. Schematic representation of the MOSS set-up and the associated ray-diagram has been presented in Fig. 3a and b. The curvature of the substrate (κ) is estimated based on the following relation:[5–7,11–13,30,31,50,61,66,87]

$$\kappa = \frac{(d-d^0)}{d^0}\frac{1}{A_m} \quad (7)$$

where d is the distance between two adjacent reflected laser beams (*viz.*, spots), as captured using the CCD camera, d^0 is the initial distance and A_m is the mirror constant, where $A_m = 2L/\cos(\theta)$, with L being the optical path length between the substrate and the CCD camera and θ being the incident angle of the laser beam on the substrate (see Fig. 3a and b).

Unlike the cantilever-based substrate curvature measurement technique, where the film–substrate system needs to have a rectangular geometry (as mentioned in the previous subsection), the film–substrate system for use with a MOSS usually has a thin and circular geometry. For monitoring the stress development in electrode materials in real-time during electrochemical cycling, the fabricated circular electrode–substrate system is assembled inside a custom-made electrochemical cell (as shown in Fig. 3c), which is similar, in principle, to the type of cell used with the cantilever-based technique, but with subtle differences to better suit the use of the MOSS. In this case, the custom-made cell usually has a Teflon chamber, which is externally supported by stainless steel lining. Again, the counter/reference electrode (*i.e.*, Li metal foil), preferably mounted on a stainless steel plate, is placed at

the bottom of the cell compartment, followed by a separator soaked in the electrolyte and, finally, the working electrode 'on top', with the reflective/polished surface (*i.e.*, the back side) of the substrate facing a quartz window. The connection to the reference-cum-counter electrode is made *via* the bottom stainless steel plate with the use of connecting stainless steel screws protruding to the exterior, while that to the working electrode film is made with the use of Cu tape attached to the partially exposed current collector film present in-between the substrate and the active electrode film (as schematically depicted in Fig. 3d). Again, the cell is assembled in a controlled (inert) atmosphere chamber, with O_2 and moisture ppm levels maintained below ~1. Silicone O-rings and sufficient screws allow proper sealing of the electrochemical cell after assembly to prevent leakage and exposure to atmospheric species during electrochemical cycling.

A typical evolution of curvature of the substrate, say during Li-insertion/removal into/from the active electrode film, is schematically presented in Fig. 3e. During Li-insertion, if the electrode film dilates in the in-plane direction, due to constraint from the stiff substrate the entire substrate–electrode system develops a negative curvature, with the reverse happening during Li-removal. It is this change in curvature which is monitored *via* the change in spacing of the array of reflected laser beams, as per eqn (7) and then converted to in-plane stress in the active electrode film, as per the basic or modified Stoney's equation(s), as applicable.

The demonstration pertaining to the possibility of using MOSSs for monitoring the stress development in electrode materials (anodes, to start with) for Li-ion batteries *in situ* during electrochemical cycling was made at Brown University (in 2010–11).[7,12,22] Since then researchers of different groups world-wide have extensively used this technique towards monitoring of the stress development in different electrodes in real-time and deciphering important information on many associated aspects, such as viscous flow during lithiation/delithiation of Si,[5–7,11–13,17,30,31,50,61,87,101,102,108] instability caused by phase transformations[18,19,24,54] and structural changes[25] in electrodes, effects of the presence of graphene-based buffer interlayers[17] and stress development due to irreversible surface reactions (such as SEI layer formation).[20–23,54] More detailed discussions on the findings, upon the usage of MOSSs, as well as the cantilever method, appear in Sections 4–7.

3.3. Advantages and challenges associated with the substrate curvature methodology

As already mentioned in a more generic sense in Section 3.1, one of the advantages of the substrate curvature technique is that the active electrode material does not need to be exposed/used for the stress measurements, which can be done solely by (optical) gaining access to the 'back-side' of the substrate. This protects the active material from any laser induced damage. More importantly, this, in turn, facilitates conducting measurements in real-time (*i.e.*, *in operando*) during electrochemical cycling because the active electrode material is wetted by the electrolyte and faces the counter electrode and, thus, is not easily accessible for extraneous measurements, whereas the 'back-side' or substrate side is. Furthermore, measurements can be made irrespective of the electrode (or the substrate) being crystalline or amorphous in nature (unlike the X-ray diffraction method of measuring internal stresses, which is limited only to crystalline materials). Additionally, sample preparation and cell design/assembly required for conducting the *in situ* stress measurements based on the substrate curvature technique are relatively simpler, as compared to those for other *in situ* characterization techniques (such as *in situ* TEM, AFM *etc.*). The practical difficulties and limitations associated with the different *in situ* techniques have been explicitly mentioned in Table 2.

In addition to the above advantages offered by the substrate curvature methodology, in general, certain specific advantages of the MOSS system, in particular, can be highlighted, as in the following.

(i) Multi-point illumination and detection (*i.e.*, usage of more than one laser beams) reduce the sensitivity to ambient vibrations. In simpler terms, if all the laser beams change position together in response to any vibration, the measurement is not affected because it depends only on the relative spacing between the reflected laser beams and not on the exact position of the individual beams (unlike the situation when the position/deflection of a single laser beam is tracked).

(ii) Measurements can be made with substrates having a curvature radius of at least as large as 4 km, which provides a good resolution towards curvature measurement (and accordingly, in-plane stress). In principle, for an active film of thickness ~100 nm, the usage of MOSSs can allow the measurement of a stress level down to ~1 MPa.[48]

(iii) The MOSS does not have any moving part, with the optical alignment being fairly simple.

On a different note, in contrast to the use of the MOSS set-up and the associated custom-made cell-type, one of the advantages associated with the use of the cantilever-type set-up for monitoring the in-plane stress development is the possibility to simultaneously monitor the change in dimensions (or strain) of the electrode (as described in ref. 106). Nevertheless, there are a few practical challenges associated with the aforementioned techniques based on substrate curvature. First of all, care must be taken that the back-side of the substrate of the working electrode is reflective enough for the laser beams to be detected post reflection. On similar lines, the amount of electrolyte used in the custom-made electrochemical cell for such measurements needs to be carefully optimized to ensure good wetting of the separator and electrodes, while at the same time prevent any spill-over to the back side of the substrate (to prevent loss of reflectivity and 'artificial' creation of apparent curvatures). Furthermore, ensuring good connectivity to the electrodes and proper sealing of custom-made cells are always challenging (as compared to standard cell geometries). On a different note, estimation of the correct value of the in-plane stress necessitates the use of the right equations for the concerned electrode types (as detailed in Section 3.1) and also ensuring that Stoney's law and the corresponding equations are valid under the given

Table 2 Comparisons of the practical difficulties and possible limitations associated with the various *in situ* techniques discussed in this manuscript

Type of *in situ* methodology/technique	Practical difficulties	Limitations
Substrate curvature	• The back-side of the film–substrate system must be polished and reflective	• Cannot be used for very thick electrode films
	• For 'porous composite' electrode materials, the contributions from the various constituents (*viz.*, binder, conductive additive, buffer *etc.*) and porosity must be taken into account for estimating/analyzing the stress development	• Stiffness of the substrate should be higher than that of the film
	• For 'porous composite' electrodes, modified Stoney's equation is used which involves tedious calculations	• The substrate should not undergo plastic deformation over the entire course of the measurement
	• Cantilever-based method is sensitive to mechanical vibrations	
	• The mechanical properties of the electrodes do not remain constant over the entire electrochemical cycling, which need to be taken into account while analyzing/estimating the stress development	
Transmission electron microscopy (TEM)	• Complex micro-electrochemical cell design and sample (electrode) preparation needed	• Limited to samples (*i.e.*, electrode materials) with dimension (or thickness) $\leq$100 nm (*viz.*, thickness limit for being electron transparent)
	• The sample (electrode material) under consideration should be stable under very high vacuum condition	• Prolonged exposure of the sample (electrode material) to an electron beam may alter the properties
	• The window of the micro-electrochemical cell should be enough thin and electron transparent	• The electrolyte/electrode interfacial region, from where the diffusion of Li/Na into/out of the electrode takes place, is extremely small unlike in the case of a real battery electrode. This may lead to some inconsistencies and artefacts
	• Application of current and voltage bias to the electrodes under consideration is very critical, which may, in turn, get disturbed during the electrochemical cycling	• Unlike for real batteries, various events, such as SEI layer formation (*viz.*, reaction with the liquid electrolyte), may get bypassed due to the usage of solid electrolytes (such as Li_2O) in *in situ* TEM cells
		• If a liquid electrolyte is used, the SEI layer that may be formed is usually sensitive to a high energy electron beam
		• The high energy electron beam can also lead to breakdown of electrolyte/solvent molecules
		• The application of high bias and high charge transfer resistance may interfere with the results
Atomic force microscopy (AFM)	• Complex design of the electrochemical cell. Both the AFM set-up and the electrochemical cell (which is usually open) need to be kept inside the glove-box	• Surface roughness increased due to SEI layer formation during the electrochemical cycling and may lead to artefacts
	• AFM is very sensitive to mechanical vibrations and require a vibration cancellation stage	• AFM is limited to topographic features only
X-ray diffraction (XRD)	• The electrochemical cell must have a durable, chemically inert and X-ray transparent window membrane	• Direct estimation of strain/stress (or micro-strain/micro-stress) is difficult, with the strain/stress often being estimated from just a localized region (may or may not be representative of the entire electrode)
	• The usually used Be window is not stable for cathodes electrochemically active beyond $\sim$4.0 V (*vs.* Li/Li^+)	• The other cell components may either contribute additional/undesired signals or reduce the intensity of the incident X-ray and transmitted radiation
	• The incident X-rays need to have good intensity because they and the diffracted X-rays have to travel through a few different materials (*viz.*, window, current collectors, separator *etc.*) present in the cell prior to being detected. Hence, absorption and concomitantly low intensity for the X-rays that get detected are the issues	• The availability and cost of high energy X-ray radiation are critical
	• Accordingly, high energy X-ray (*viz.*, synchrotron radiation) is desirable for obtaining good quality signal	• XRD is limited to crystalline and semi-crystalline materials and cannot be used for amorphous electrode materials

Table 2 (*Contd.*)

Type of *in situ* methodology/technique	Practical difficulties	Limitations
Raman spectroscopy	• Prolonged exposure to the laser source may 'burn'/damage the active material	• Properties of the active electrode may get altered due to heating from the incident laser source
	• The transparent window of the electrochemical cell should be either Raman insensitive or it has to be taken care that the signals from the window do not interfere with the signals from the active material	• Due to the fluorescence in some active materials, the Raman signals are masked
	• Additional filters or microscopes are usually required to enhance the weak Raman signals	• The SEI layer formed on the surface of the active materials decreases the intensity of Raman signals, which sometimes get totally annihilated
	• As compared to SEM and TEM, the electrochemical cell used for Raman measurements is simpler, but leakage and sealing are some of the major challenges	• Raman spectroscopy can only be applied to those active materials which are Raman active
Digital image correlation (DIC)	• The complex electrochemical cell with a transparent window needed to observe electrode surface	• The estimated strain/stress is merely an average
	• The experimental set-up is sensitive to mechanical vibrations	
	• In the experimental set-up, the electrode should be parallel to and face the digital image recording device	
	• To obtain good quality results, a laser illumination source and high resolution camera are needed	
	• Requires advance numerical computation and image processing skills to estimate the strain/stress	
Scanning electron microscopy (SEM) and focused-ion beam (FIB)	• SEM and FIB are operated under very high vacuum	• Usually, the resolution is limited to ~1–10 nm
	• Hence, SEM or FIB cannot usually be performed with a liquid electrolyte	• With the use of solid or vapor electrolytes, performance of an electrode and the associated electro-chemo-mechanical response may be different from those with a liquid electrolyte
	• Ideally, the sample under consideration should be conducting in nature	• Direct estimation of the strain/stress is not possible
	• A complex experimental set-up and miniature electrochemical cell are required to avoid environment contamination	
X-ray absorption spectroscopy	• The practical challenges for *in situ* XAS are similar to those of XRD	• Analysis and fitting of the XAS signal is complicated and tedious
		• Estimation of strain/stress is not possible
Mössbauer spectroscopy	• Requires a high energy γ-radiation source	• The Mössbauer effect is absent for Li, C, H, O, F, P *etc.* Accordingly, it is not suitable for studying the electrolyte, SEI layer or Li-dendrites
	• The electrochemical cell design and the associated challenges are similar to those for *in situ* XRD and XAS measurements	
Dilatometry	• Complex electrochemical cell design, with the entire experimental set-up being needed to be placed inside an Ar-filled glove-box	• Separation of the expansion of anode and cathode individually is usually not possible
		• The actual pressure on the electrode surface cannot be estimated
		• For a 'porous composite' electrode, porosity may change during electrochemical cycling, which is usually not taken into account
Nanoindentation	• The active material and the nano-indenter need to be submerged in a fluid cell environment	• Volumetric changes, structural degradation and SEI layer formation/growth during electrochemical cycling may interfere during the nanoindentation measurements
	• The electrochemical cell and the nano-indenter need to be placed inside a controlled Ar-filled glove-box	• Contribution from the fluid environment needs to be eliminated
	• The active material should get inserted into the fluid used for submerging the active material	

conditions. Additionally, correct interpretation of the stress responses and associating the same to the actual physical/chemical phenomena occurring at the electrode (such as phase transformation, plastic deformation, SEI layer formation *etc.*) necessitate detailed knowledge-cum-experience of the various phenomena that take place in the concerned electrochemical cell(s) and electrode(s) at different states-of-charges and voltage windows.

4. Real-time monitoring of stresses and associated instabilities in anode materials

Considering that some of the 'alloying reaction' based anode materials, such as Si, Sn, Ge, undergo colossal dimensional changes upon lithiation/delithiation (up to even 400%, as for Si), extensive research has been done to monitor the stress development in such electrodes *in situ* during electrochemical cycling using both the substrate curvature based techniques, *viz.*, MOSS, and cantilever methods (as described in detail in the previous section). Nevertheless, quite a few such studies have also been conducted with graphitic and graphenic carbon based electrodes, which have resulted in unravelling some unknown aspects associated with stress development even in such cases. In these contexts, the following sub-sections will provide detailed discussion on the as-reported electro-chemo-mechanical responses of various anode materials.

4.1. For Si-based electrodes

The first few reported studies on *in situ* monitoring of stress development with Si film electrodes (in custom-made Li 'half cells') using the MOSS set-up[6,7,12,30] confirmed the development of compressive stress during Li-insertion into an amorphous Si (a-Si) matrix (as also mentioned in Section 3). The more interesting-cum-important observation was that after an initial monotonous compressive stress build-up during lithiation up to between ~(−)1.2 and 1.7 GPa (depending on the current density and film thickness used), flattening of the stress response, followed by stress relaxation, occurred due to viscous flow (or plastic deformation) in Si beyond the aforementioned 'elastic limit' (see Fig. 4a and b). During the delithiation half cycle, the overall compressive stress was observed to first get rapidly reversed towards the tensile direction, followed by a similar viscous flow upon attaining a net tensile stress of ~(+)1 GPa. The (−) and (+) signs here indicate compressive and tensile stresses, respectively. With regard to the magnitude of the 'elastic limit' of Si during lithiation, Zhao *et al.*[102] reported the same to be ~(−)2 GPa, which was slightly greater than those reported in earlier studies. A similar magnitude for the 'elastic limit' [*i.e.*, ~(−)2.5 GPa] was also observed by us during the first lithiation half cycle of a-Si film,[17] but it decreased to ~(−)1 GPa in the very next cycle. The spread in the observed magnitude for the 'elastic limit' is likely to be partly influenced by the Si film thickness (often varying inversely with the thickness, due to diffusion limited Li-storage[7,13]), growth stress developed during deposition,[7,11,48] current density used, irreversible surface reactions (including SEI layer formation[17,21]) and specific features of the set-up used (including possible aberration due to multiple refraction of the laser[6,12,30,31] and the equations used). Nevertheless, the very observation/information concerning the occurrence of viscous flow (or plastic deformation) of Si during lithiation/delithiation was made possible only by such *in situ* stress measurements.

In the above context, considering that viscous/plastic flow in an electrode material during lithiation/delithiation is extremely detrimental towards the integrity of the same, efforts were

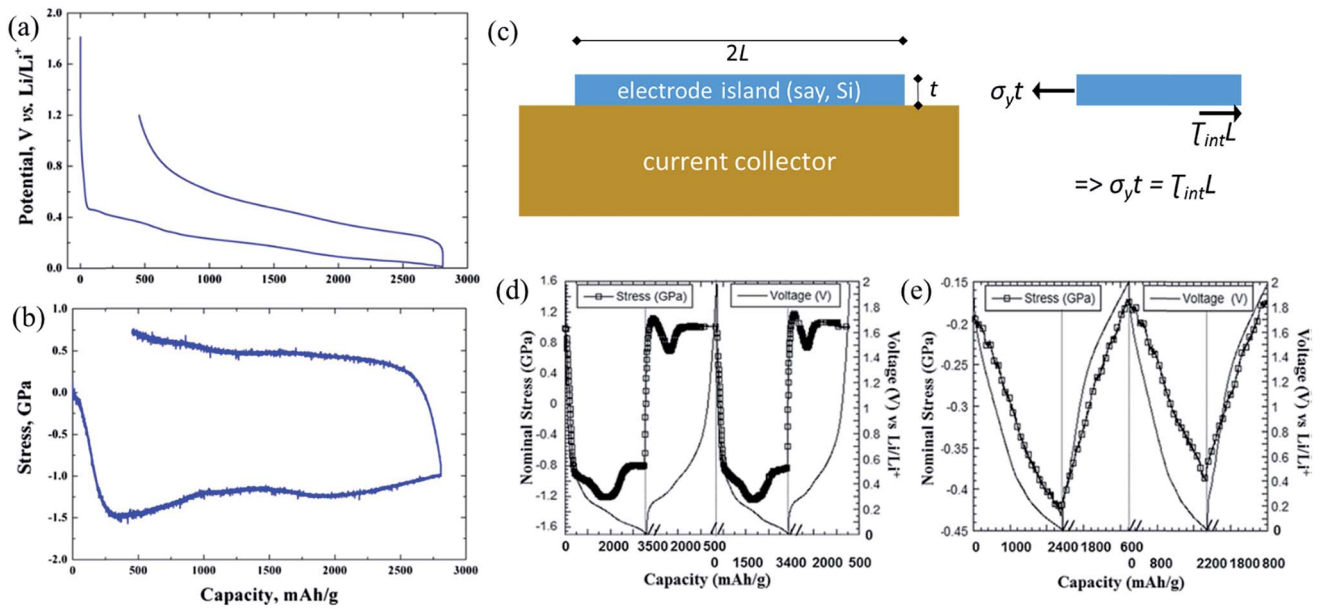

Fig. 4 (a) Potential and (b) *in situ* stress profiles obtained with 250 nm thick a-Si film when galvanostatically cycled between 1.2 and 0.01 V *vs.* Li/Li$^+$ at a current density equivalent to C/4 (reproduced with permission.[30] Copyright 2010, The Electrochemical Society). (c) Schematic representation of a (lithiated) Si island on the current collector and free body diagram of half the Si island showing the force balance (adapted from ref. 50). Variations of the in-plane 'nominal' stress (black line with square symbols) and voltage (thin black line) with the capacity during the 2nd and 3rd galvanostatic cycles (between 0.05 and 2.0 V *vs.* Li/Li$^+$ at C/20) of 50 nm thick (d) continuous a-Si film and (e) patterned a-Si (island-type) film (pattern dimension of 7 × 7 μm) electrodes. In contrast to that of the continuous film, the stress evolution in the patterned a-Si film electrode is monotonous (reproduced with permission.[50] Copyright 2011, The Electrochemical Society).

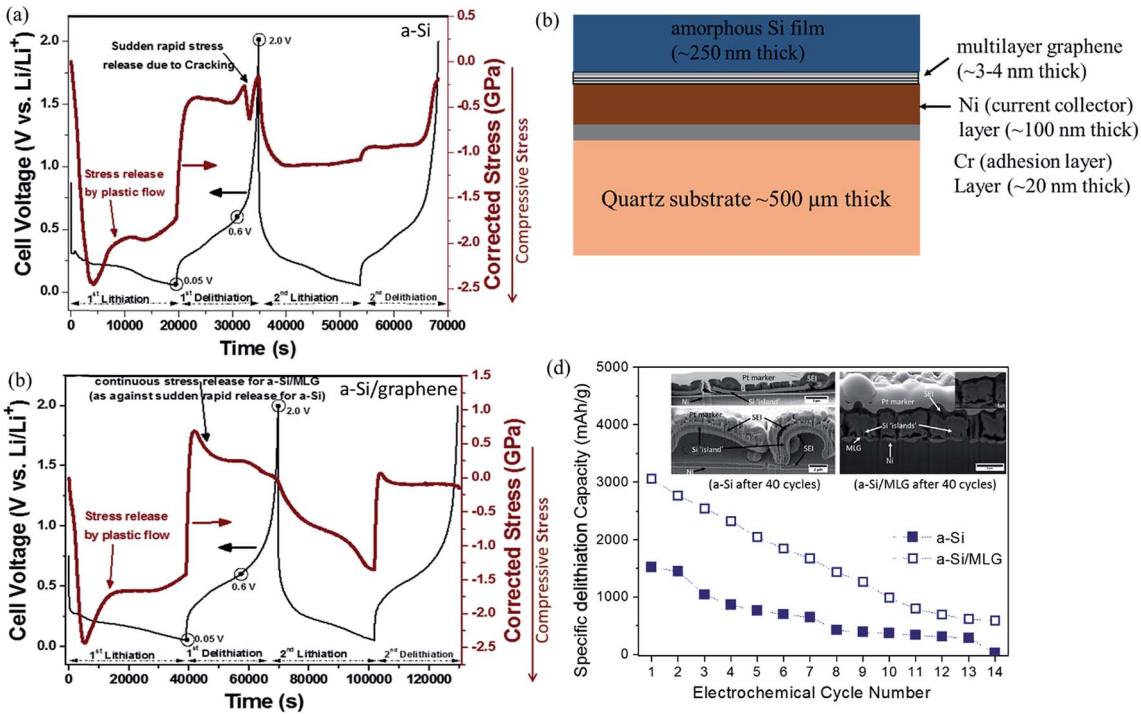

Fig. 5 (a) Stress response (as monitored *in situ*) and voltage profiles for a 250 nm thick a-Si film electrode when subjected to electrochemical lithiation and delithiation (*via* galvanostatic cycling). A sharp 'dip' in the stress profile towards the end of the first delithiation cycle is an indication of stress release due to fracture of the Si film. (b) Schematic representation of the composite a-Si film electrode having a thin multi-layered graphene film sandwiched between the Ni current collector and 'active' a-Si film. (c) The *in situ* stress and voltage profiles for the 250 nm thick a-Si film electrode, in the presence of the MLG 'buffer' interlayer, showing the absence of the sudden sharp dip during the 1st delithiation half cycle. (d) Variations of the delithiation capacities (*i.e.*, reversible Li-storage capacities) with the electrochemical cycle number for the a-Si film electrodes, in the absence and presence of the MLG interlayer, with the insets showing cross-sectional SEM images obtained after electrochemical cycling (reproduced with permission.[17] Copyright 2016, Elsevier).

directed towards suppressing the flow in Si electrodes. Pioneering studies by Soni *et al.*[50] and Haftbaradaran *et al.*[49] indicated that reducing the in-plane dimension of Si films by developing 'patterned films', consisting of Si islands, enhances the structural and (thus) electrochemical/cycle stabilities of the Si film electrode, especially when the in-plane dimensions of the islands are below a 'critical size'. In fact, *in situ* stress measurements of patterned a-Si films having island dimensions ≤ 7 μm indicated nearly complete suppression of plastic flow during lithiation/delithiation.[50] Based on the consideration that the stress in the electrode film/island is balanced by the shear resistance at the interface between the island and the current collector, a manifestation of the shear lag model[50,109] was used to predict the critical lateral size (*i.e.*, lateral or in-plane dimension) of the a-Si islands (L_{cr}), as per the following relation (as schematically depicted in Fig. 4c):

$$L_{cr} \approx 2\sigma_y t/\tau_{int} \quad (8)$$

where σ_y is the elastic limit (or yield strength) of Si, t is the out-of-plane film thickness and τ_{int} is the interfacial shear strength. τ_{int} takes the value of either the interfacial friction/adhesion strength at the electrode–collector interface or the shear yield strength of the current collector (or any interlayer between the current collector and electrode film, as the case may be), whichever is lesser. In the case of the a-Si film electrode on Cu and Ti current collectors, the above model predicted a critical Si island size of between ~5 and 9 μm (depending on τ_{int} and film thickness, between 50 and 100 nm) for nearly completely suppressing the plastic flow and concomitantly suppressing cracking of the a-Si film upon lithiation/delithiation to a considerable extent.[50,109] It was encouraging that the estimated values agreed with the observations based on the *in situ* stress measurements (see Fig. 4d and e) and also post-cycling SEM.

Looking beyond the occurrence of plastic flow in Si, *in situ* stress measurements with a continuous crystalline Si (c-Si) film by Chon *et al.*[31] and amorphous Si film by us[17] showed a sudden and sharp 'dip' in the otherwise flattened stress profile towards the later stages of delithiation in the first cycle itself (see Fig. 5a). Coupling this with SEM observations indicated that the sudden 'dip' in the stress profile is caused due to cracking of the Si films, usually in the form of 'channel type cracks'.[11,17,101] With respect to the occurrence of cracking, an important inference from the work by Soni *et al.*[13] for the a-Si film electrode is that the fairly slow diffusion of Li in Si (*viz.*, $\sim 3 \times 10^{-13}$ cm^2 s^{-1}) causes the average stress in the film (as measured *in situ* using the MOSS) to get reduced with increasing current density (or C-rate) due to the suppressed degree of lithiation, but causes severe local stress concentrations due to steep concentration gradients (and associated differential expansion/contraction),

which leads to cracking. Furthermore, the *in situ* stress observations facilitated the estimation of the fracture energy (Γ) of Si, which was found to be fairly invariant with the degree of lithiation, *viz.*, $\Gamma = 8.5 \pm 4.3$ J m^{-2} for amorphous $Li_{0.7}Si$, $\Gamma = 5.4 \pm 2.2$ to 6.9 ± 1.9 J m^{-2} for amorphous $Li_{2.8}Si$ and $\Gamma = 5$–14 J m^{-2} for c-Si.[11,101] In addition to the findings and understanding related to stress development during electrochemical lithiation/delithiation and the associated mechanical integrity of Si-based electrodes, *in situ* stress measurements with Si film electrodes using the MOSS have also provided important insights associated with the effects of stresses on the thermodynamics, potential hysteresis and kinetics of the lithiation/delithiation process.[17,30,58,62] These aspects will be detailed later in this review (*viz.*, in Section 8).

In order to understand the influence of a graphenic carbon based interlayer between a-Si and current collector on the structural and electrochemical stabilities of a-Si upon repeated lithiation/delithiation, we performed *in situ* monitoring of stress development during electrochemical cycling of the a-Si film electrode having a well-ordered multi-layer graphene film (MLG; ~10 graphene layers) between the a-Si and current collector (see Fig. 5b–d).[17] The magnitude of compressive stress developed during lithiation was suppressed to a good extent in the presence of the MLG 'buffer' interlayer (*viz.*, by ~100% per degree of lithiation). More importantly, the MLG interlayer suppressed the occurrence of plastic flow of Si during lithiation from the 2nd cycle onwards and also minimized cracking during delithiation, as noted by the absence of the sudden 'dip' in the stress profile towards the end of delithiation half cycles (in contrast to that of a-Si, sans MLG). The suppression of plastic flow of a-Si during lithiation of the a-Si/MLG electrode was associated with the weaker adhesion (*i.e.*, τ_{int}) at the Si/graphene interface and, accordingly, the L_{cr} for plastic flow [according to eqn (8)] being greater than the lateral dimensions of the fractured a-Si 'islands' post the first cycle. Furthermore, the possible contribution from reversible sliding between the constituent graphene layers of MLG in response to the in-plane dimensional changes of Si, as well as from sliding at the Si/graphene interface, towards the 'buffering/accommodation' of the stresses was not ruled out. Overall, the above mechanisms considerably improved the mechanical integrity, including near complete suppression of delamination from the current collector, and concomitantly the cycle stability upon repeated lithiation/delithiation of the Si-based electrodes, in the presence of the MLG interlayer, in complete contrast to that of the a-Si electrode, sans the MLG interlayer (Fig. 5d).

In situ monitoring of stress development in Si-based electrodes has also been performed with porous 'composite' electrodes (*i.e.*, those having binders and conducting additives), using a suitable version of modified Stoney's equation for estimating the stresses from the curvature (as mentioned in Section 3).[14,32] Not surprisingly, in the presence of pores and

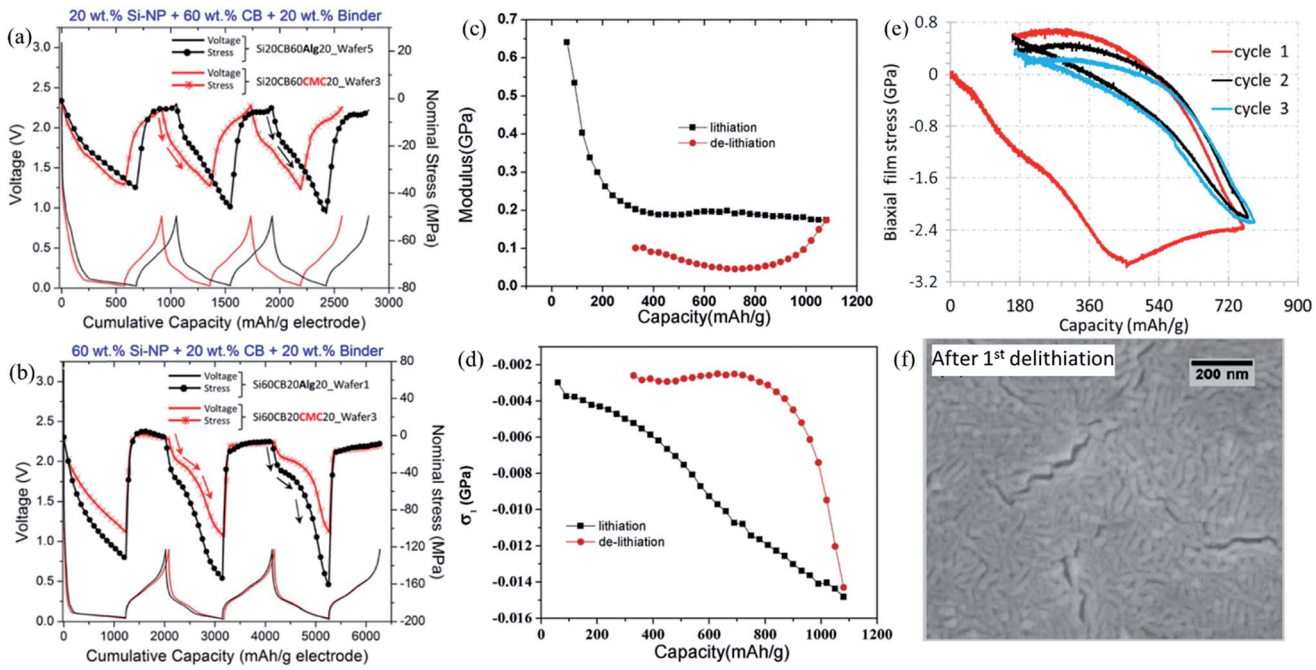

Fig. 6 Effects of the % loading of active materials (*i.e.*, Si nanoparticles) and two types of binders (*i.e.*, carboxymethyl cellulose (CMC) and sodium alginate) on the stress response during lithiation/delithiation of composite Si electrodes, with (a) 20 wt%, and (b) 60 wt% Si loadings (reproduced with permission.[14] Copyright 2016, The Electrochemical Society). The variations of (c) elastic modulus and (d) stress development, as measured *via* the cantilever deflection method *in situ* during the 2nd galvanostatic cycle of the Si-based composite electrode between 0.01 and 2.0 V *vs.* Li/Li$^+$ (reproduced with permission.[110] Copyright 2017, Elsevier). (e) Biaxial stress development during the first three galvanostatic lithiation/delithiation cycles (between 0.01 V and 3.0 V *vs.* Li/Li$^+$) for a 100 nm thick amorphous SiO_2 film electrode. (f) A SEM image obtained at the end of the 1st delithiation cycle, showing the presence of cracks in the amorphous SiO_2 film (reproduced with permission.[116] Copyright 2018, Society for Experimental Mechanics).

components having lower stiffness (especially, for polymeric binders), the overall magnitudes of stress developed during lithiation in such 'composite' electrodes were found to be significantly smaller than those of the continuous dense film electrodes, with the stress magnitudes increasing with increasing Si content, *viz.*, ∼(−)40 and ∼(−)150 MPa, respectively, for 20% and 60% Si loading (when using the stiffer Na-alginate binder) (Fig. 6a and b). Nevertheless, the *in situ* stress response still indicates the occurrence of a plastic flow, accompanied by considerable increase in the thickness (*i.e.*, out of plane dimension) of the electrode (in comparison to the change in the in-plane dimensions) and particle rearrangement.[14] Furthermore, across two studies,[14,32] the yield stress and the overall stress magnitude was observed to depend considerably on the binder used, *viz.*, increasing with the increase in binder stiffness, *i.e.*, polyvinylidene fluoride (PVDF) < carboxymethyl cellulose (CMC) < Na-alginate.

The cantilever method has also been used to perform *in situ* stress measurements during electrochemical cycling of composite Si electrodes.[62,104,110–112] Based on the inferences from the stress profile, Li *et al.*[110] reported that the composite Si electrode undergoes elastic softening and structural degradation during the first lithiation half cycle itself (see Fig. 6c and d). Furthermore, based on the *in situ* stress responses the elastic modulus of the composite Si electrode was estimated to decrease from ∼0.64 to ∼0.18 GPa with progress of lithiation. This trend agreed with that observed earlier by Sethuraman *et al.*[6,66] while estimating the bi-axial modulus of the Si film electrode (*viz.*, varying from ∼103 to ∼70 to ∼35 GPa for Si, $Li_{0.32}Si$ and Li_3Si, respectively) from *in situ* stress data (obtained using the MOSS) and also the theoretical predictions for elastic softening of Si upon lithiation.[113,114] Interestingly, the elastic modulus was observed to further decrease to ∼0.10 GPa midway during delithiation, which could be attributed solely to structural degradation, but with a slight increase to ∼0.20 GPa towards the end of delithiation. Hence, such *in situ* stress measurements are also capable of providing information concerning the changes in the materials properties (which also include flow stress[66] and fracture energy,[11,101] presenting similar trends as stiffness) with change in the chemical composition (*viz.*, degree of lithiation in this case). Nevertheless, with respect to stress development, the overall compressive stress build-up at the end of lithiation was found to be ∼(−)12 MPa (see Fig. 6d), which, again more or less agreed with the studies done using the MOSS. An interesting piece of inference obtained from another work with a Si-based composite electrode using the cantilever method is that the electrode deformation slows down with increasing Li-concentration in Si, which was attributed to 'slowing down' of the lithiation itself due to compressive stress development in the electrode.[62] In another work, *in situ* stress measurements with a multilayered composite cantilever consisting of single crystalline Si (as the working electrode), $LiAlF_4$ (as the solid electrolyte), Li_2WO_4 (as the Li reservoir) indicated the development of a compressive stress of greater than (−)1 GPa at the Si–Li_xSi reaction front.[111]

In addition to Si-based electrodes, *in situ* stress measurements during electrochemical lithiation/delithiation have also been conducted with SiO_x-based electrodes.[115–117] In this context, Rakshit *et al.*[116] observed isotropic volume expansion/contraction of the SiO_2 film during lithiation/delithiation, with compressive stress development [up to a peak value of ∼(−)3.1 GPa] during the lithiation half cycle and tensile stress development [up to a peak value ∼(+)0.7 GPa] during the delithiation half cycle. Similar to the case of Si, such a high compressive stress development in the SiO_2 film (which is in fact greater than the average stress recorded in Si) led to plastic deformation and fracture during the first cycle itself (Fig. 6e and f). Few other studies on *in situ* stress monitoring using the MOSS with 'composite' SiO_x electrode materials[115,117] have shown results similar to those for the composite Si electrode (as discussed above), with the overall stress magnitudes being considerably smaller than those of the SiO_x film electrodes.

However, it must be mentioned here that, to date, there has been no systematic study concerning the measurement of stress development during electrochemical lithiation/delithiation of Si electrodes having different contents and types of native Si-oxide(s) and Si-sub-oxide(s). This assumes very high importance, especially in light of our recently reported study indicating considerable influences of the presence/absence/types/contents/combinations of different Si-oxide(s)/sub-oxides (such as Si_2O, SiO, Si_2O_3, SiO_2) on the surface of Si towards not only the irreversible capacity loss, but also the cycle stability in Li 'half' and 'full' cells.[118]

4.2. For Sn-based electrodes

After Si, among the 'alloying reaction' based anode materials for Li-ion batteries, the Sn film electrode was used next for *in situ* monitoring of stress development during galvanostatic lithiation/delithiation using the MOSS, for the first time by our group.[18] Similar to the case of Si, the overall compressive stress was observed to get developed during the lithiation half cycle up to a peak average stress of ∼(−)1.4 GPa (when corrected for the change in film thickness with lithiation) with nearly complete reversal during the delithiation half cycle. The potential profile of Sn has distinct 'potential plateaus' corresponding to 1st order phase transformations between Sn and different Sn–Li intermetallic phases during the progress of lithiation and delithiation. It was very interesting to note that the stress profiles during lithiation, as well as delithiation, also showed flattening-cum-release (*i.e.*, 'stress plateaus') at almost exactly the same time (and duration) as the onset and progress of the phase transformations, *i.e.*, exactly coinciding with the 'potential plateaus' (see Fig. 7a and b), despite being fairly monotonous in nature during lithiation/delithiation in the single phase regions (*i.e.*, the solid solution regimes). Preliminary analysis based on internal stresses associated with the nucleation and growth of a new Sn–Li intermetallic phase(s) having different molar volumes (V_i) compared to the parent phase (V_m) (*i.e.*, Eigen strains or ε^*, as per $\varepsilon^* = [(V_i/V_m)^{1/3} - 1]\delta_{ij}$, where δ_{ij} is the Kronecker delta) indicated that huge internal stresses (as per $\sigma = B(S_I + 2S_{II} - 1)(3\varepsilon^*)\delta_{ij}$, B is the bulk modulus and S_I and S_{II} are Eshelby's tensors[18]) got developed during the phase

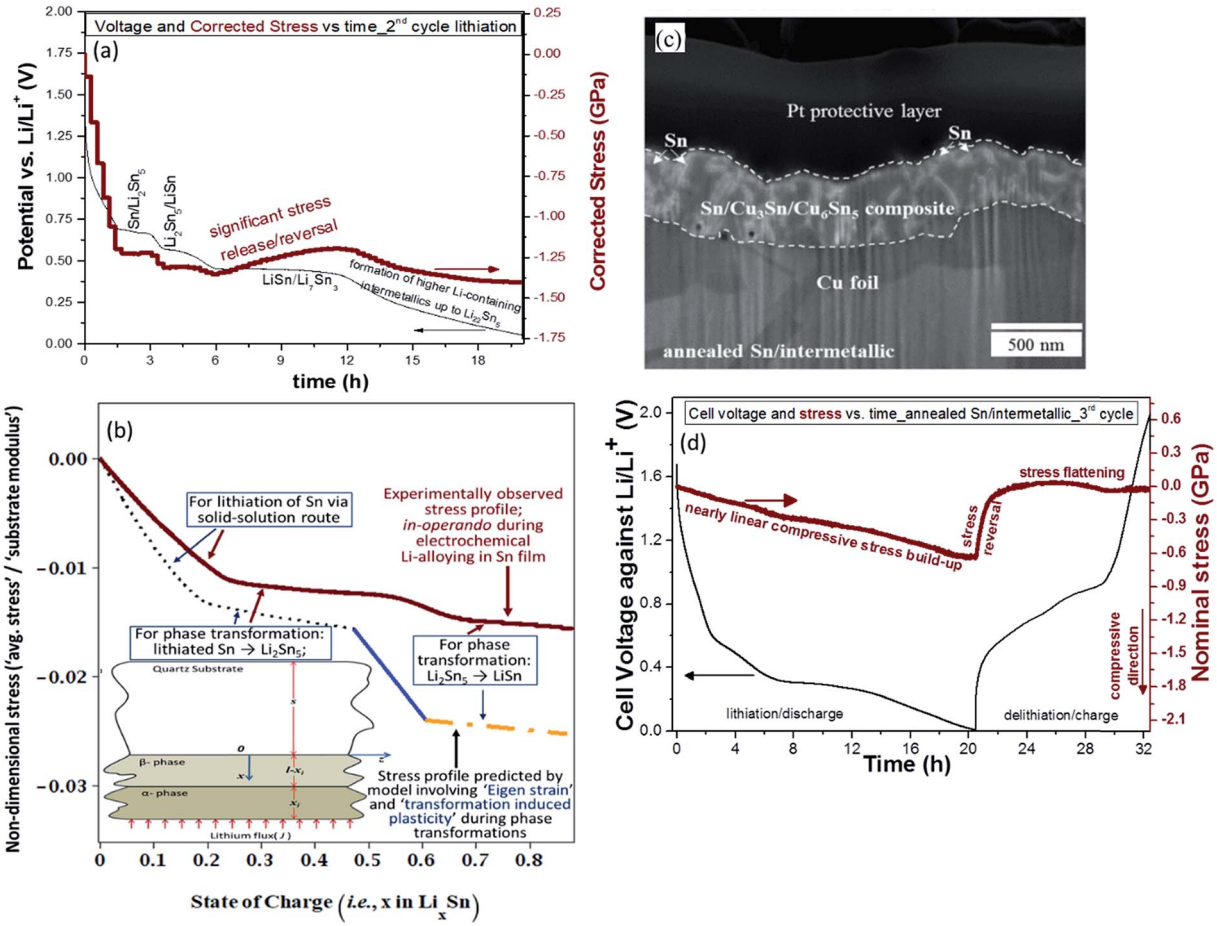

Fig. 7 (a) Voltage and in-plane stress profiles obtained for a 200 nm thick β-Sn film electrode during 2nd galvanostatic lithiation at C/20 between 0.02 and 1.5 V *vs.* Li/Li^+, showing the presence of 'stress plateaus' during the phase transformations between Sn and Sn–Li intermetallic phases (reproduced with permission.[18] Copyright 2014, Elsevier). (b) Fitting of the *in situ* stress profile with that obtained *via* mathematical modelling, which considered the influence of Eigen strains arising from phase transformations, leading to 'transformation induced plasticity', during electrochemical lithiation of the Sn film electrode (reproduced with permission.[19] Copyright 2018, American Chemical Society). (c) Cross-sectional SEM image (obtained by FIB-SEM) obtained with a heat treated Sn film (on the Cu current collector) leading to the formation of Cu_3Sn and Cu_6Sn_5 intermetallic phases, co-existing with Sn. (d) *In situ* stress profiles obtained during galvanostatic lithiation/delithiation (between 0.01 and 2.0 V *vs.* Li/Li^+ at C/20) of such a Sn/Sn–Cu film electrode, showing the absence of 'stress plateaus' (reproduced with permission.[56] Copyright 2016, Elsevier).

transformations. For example, the estimated internal stress based on the Eigen strain corresponding to the phase transformation [(4/3)Li + LiSn ↔ (1/3)Li_7Sn_3] was estimated to be up to ~(−)8.4 GPa, otherwise typically varying between ~(−)1–5 GPa for other phase transformations. Subsequently, detailed modelling of the bi-axial stress development in the Sn film during lithiation confirmed that the flattening of the stress response during the phase transformation regimes was indeed due to internal stresses caused by Eigen strains, leading to 'transformation induced plasticity'[19] and instabilities of a similar nature in the stress responses during the Sn → Li_2Sn_5 phase transformation upon potentiostatic lithiation of thicker Sn films were also reported. Overall, the *in situ* experiments provided important insights into the mechanical instability of Sn during lithiation/delithiation, which was noted to happen primarily during the phase transformation regimes. Apart from Sn-based electrodes, such an instability in the stress response during phase transformation has also been observed by us for other 'alloying reaction' based anode[55] and Li-T_M-oxide based cathode materials for Li-ion batteries,[24] as will be discussed later.

In situ stress measurements with a composite film electrode consisting of Sn and Sn–Cu intermetallic phases (*i.e.*, Cu_3Sn and Cu_6Sn_5 phases) (Fig. 7c), as obtained by annealing treatment of the Sn film deposited on Cu under optimized conditions, indicated that the 'stress plateaus' or instabilities associated with the 1st order phase transformations during lithiation/delithiation of the pure Sn phase can be alleviate to some extent (Fig. 7d).[56] Accordingly, such a 'phase assemblage' improved the structural and cycle stability of the Sn film electrodes upon repeated electrochemical lithiation/delithiation.

In another work with Sn-based intermetallic phases, Mukaibo *et al.*[119] reported the development of tensile stress in the Cu current collector/substrate initially (*via* the cantilever

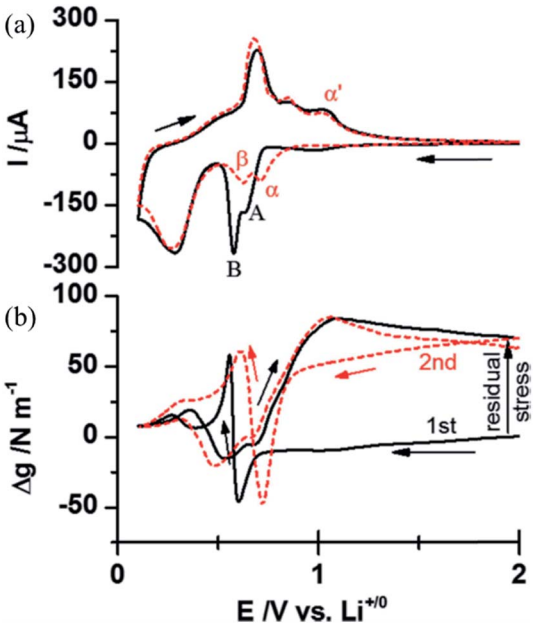

Fig. 8 (a) The first two cyclic voltammograms and (b) associated surface stress responses of the SnO_x film electrode, when scanned between 2.0 and 0.1 V *vs.* Li/Li^+ (reproduced with permission.[120] Copyright 2014, WILEY-VCH).

method) in response to the lithiation induced dilation of the pure Sn film electrode, which was followed by 'stress accommodation' and 'stress release' (between potentials of 0.24 and 0.19 V *vs.* Li/Li^+). By contrast, the signatures of 'stress accommodation' and 'stress release' were absent during lithiation of a $Ni_{0.62}Sn$ film, leading to an experimentally observed average overall stress development of ~(−)490 MPa, but which was apparently suppressed due to the 'stress release' phenomena to ~(−)52 MPa in the case of the pure Sn film electrode. In fact, during the delithiation half cycle, the occurrence of 'stress release' in the case of the pure Sn film electrode was seen to be associated with cracking. Such observations were in agreement with our aforementioned work on a Sn/Sn–Cu intermetallic film electrode.[56]

Gewirth and co-workers[120] studied the stress evolution during lithiation/delithiation of SnO_x film electrodes. In the case of SnO_x, during the cathodic scan of cyclic voltammetry, compressive stress build-up was initially noted at ~0.7 V (*vs.* Li/Li^+), which was followed by transition to a tensile nature (unlike Sn). This 'compressive-to-tensile' transition in the stress state during lithiation of SnO_x was attributed to the typicality of the conversion mechanism, where metallic Sn, having less volume (per Sn atom) by ~35% with respect to that of Sn-oxide, forms from the oxide. Of course the tensile stress subsides upon subsequent lithiation of metallic Sn. During the anodic scan (*i.e.*, delithiation), the as-developed tensile stress was found to become compressive fairly rapidly (in contrast to that for Sn). Nevertheless, at potentials greater than 0.5 V (*vs.* Li/Li^+), transition to tensile stress was noted, which was attributed to the formation of delithiated metallic Sn (and not SnO_x). Interestingly, continued anodic scan caused the tensile stress to increase until about 1 V (*vs.* Li/Li^+), which was tentatively attributed to the partial delithiation of Li_2O (Fig. 8a and b).

4.3. For carbon-based electrodes

In the first report on real-time monitoring of stress development during electrochemical lithiation/delithiation of graphitic carbon based electrodes using the MOSS set-up, Mukhopadhyay *et al.*[22] observed that a *c*-axis oriented graphitic carbon film (of ~200 nm thickness) experiences fairly low in-plane compressive stress development of ~(−)250 MPa due to Li-intercalation, which gets nearly completely reversed during Li-deintercalation (Fig. 9a). Such a stress level is considerably lower compared to those observed in the cases of the 'alloying reaction' based anode materials, as discussed in the previous subsections. In addition to the lower degree of dilation/contraction of the basal planes upon lithiation/delithiation (*viz.*, ~1%), possible reversible sliding between the constituent graphene layers of the well-ordered graphitic carbon film was tentatively associated with the low stress development. More importantly, no signature for flattening of the stress response due to plastic deformation or cracking could be observed in the *in situ* stress profiles. In fact, estimation based on simple thin film mechanics suggested that the low in-plane stress development might render it feasible to use continuous graphitic carbon films with a thickness of up to ~300 μm as the active material without problems related to delamination from stress development during lithiation/delithiation. This will allow the development of film-based electrodes of fairly high overall capacity for graphitic carbon. Such observations tie-up nicely with the good cycle stability of the presently used graphitic carbon based anode materials in Li-ion cells. However, some of the more interesting and significant observations include the development of irreversible compressive stresses associated with irreversible surface reactions (including the formation of the solid electrolyte interface or SEI layer[121–123]), in the initial few cycles of graphitic/graphenic carbon based electrodes.[20–23] Such observations, mechanisms and implications will be discussed in detail, later in Section 6.

In contrast to the stress magnitudes recorded with *c*-axis oriented graphitic carbon film based electrodes, in our more recent work with *c*-axis oriented well-ordered few layer graphene (FLG; ~7 layers) film based electrodes, a reversible compressive stress development of ~(−)10–12 GPa was recorded upon galvanostatic lithiation.[23] In fact, such a magnitude agrees very well with the expected in-plane stress based on a ~1% dilation along the nearly defect free graphene planes (considering in-plane elastic modulus of ~1 TPa). This indicates that the stress relaxation mechanisms are better operative in *c*-axis oriented graphitic/graphenic carbon films having greater thickness (*i.e.*, the number of constituent graphene layers). Another very interesting observation in the case of FLG was that of signatures of 'stress flattening' and 'stress release' in the *in situ* stress profiles within narrow voltage windows during the initial stages of lithiation and later stages of delithiation (Fig. 9b). Such signatures became more severe with increasing current density (as indicated in Fig. 9b). Detailed analysis indicated that the

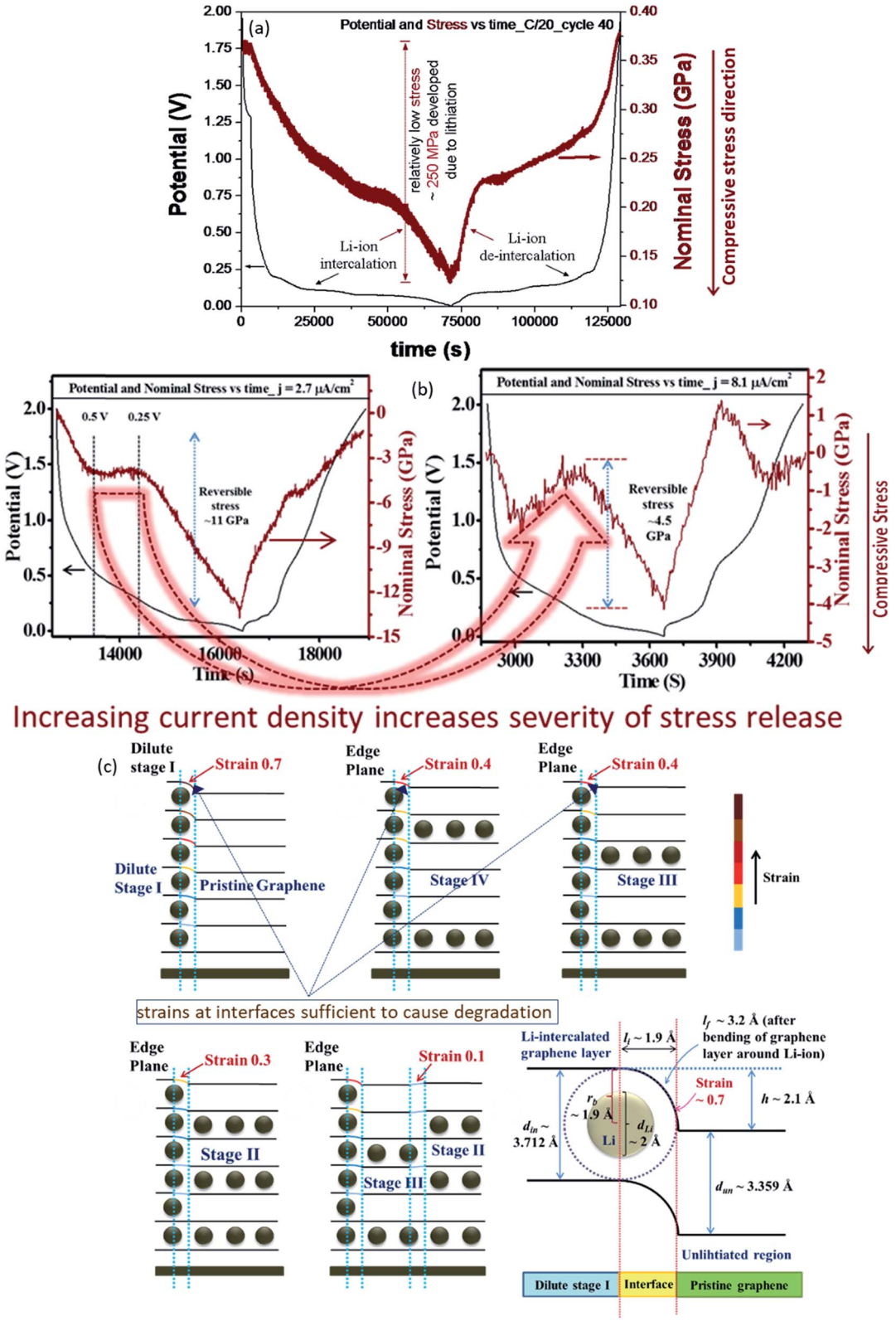

Fig. 9 Voltage and *in situ* stress profiles recorded during galvanostatic lithiation/delithiation of CVD-grown (a) graphitic carbon film (~200 nm thick) (reproduced with permission.[22] Copyright 2015, Elsevier) and (b) few layer graphene film (FLG; ~7 layers) electrodes (reproduced with permission.[23] Copyright 2015, Elsevier). In the case of the FLG film electrode (*i.e.*, b), 'stress plateaus' can be seen during lithiation (between 0.5 and 0.25 V *vs.* Li/Li^+) and delithiation (between 0.6 and 1.0 V) cycles when cycled at a current density of 2.7 μA cm^{-2}, which changed to signatures of stress release when cycled at a higher current density of 8.1 μA cm^{-2}. (c) Schematic representation of the stretching and bending of individual graphene layers around the Li-ion at the interfaces of the different co-existing Li-GICs (reproduced with permission.[23] Copyright 2015, Elsevier).

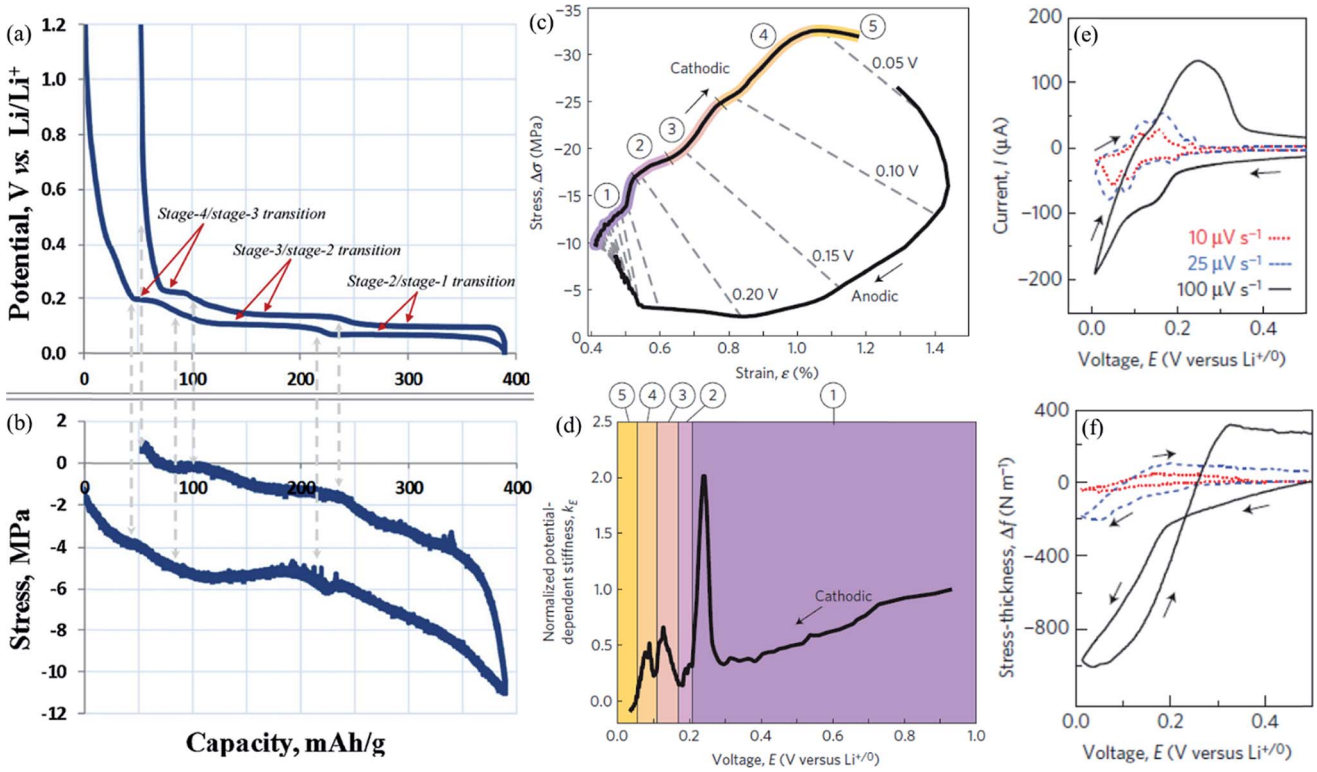

Fig. 10 (a) Potential and (b) *in situ* stress responses of the composite graphite electrode (having 92% graphite particles and 8% binder) during the 1st galvanostatic lithiation/delithiation cycle between 1.2 and 0.01 V *vs.* Li/Li^+ at a current density equivalent to C/36 (reproduced with permission.[5] Copyright 2012, Elsevier). (c) Developments of stress and strain during cyclic voltammetry of the composite graphite electrode in a Li 'half cell'. (d) Changes in the potential-dependent stiffness of the composite graphite electrode during the cathodic scan (*i.e.*, lithiation). (e) CV at different scan rates and (f) the corresponding stress response (N m^{-1}) of the composite graphite electrode (reproduced with permission.[106] Copyright 2016, Springer Nature).

stress instability was associated with mechanical degradation of the individual constituent graphene layers due to localized stretching beyond the fracture strain at interfaces between co-existing dilute stage I and stage IV Li-graphite intercalation compounds (Li-GICs) (see Fig. 9c). It may be pointed out here that, in addition to the lower stress magnitudes, signatures for such instabilities were also not apparent in the *in situ* stress profiles obtained with the thicker graphitic carbon film electrode.[22] Hence, further investigations concerning *in situ* stress measurements with well-ordered *c*-axis oriented graphenic/graphitic carbon films of systematically varied thicknesses are likely to allow better understanding of the above differences.

Moving ahead from film-based electrodes, Sethuraman *et al.*[5] monitored the stress development during electrochemical cycling of the more usual composite graphite electrode (having binders, conducting additives *etc.*) using the MOSS set-up. In this case, a maximum compressive stress of (−)12 MPa was measured during lithiation, with the *in situ* stress profile having signatures of intermediate 'stress plateaus', almost coinciding with the 'potential plateaus' corresponding to the transition between the different Li-GICs (Fig. 10a and b), an observation similar to that made for Sn-based electrodes (as discussed in Section 4.2).[18,19] Such measurements also showed that the binder swells up upon coming into contact with the electrolyte and this additionally contributes ~(−)1–2 MPa of compressive stress.

The cantilever method has been used by a few groups to monitor the stress (and also strain) responses of 'composite' graphite electrodes during electrochemical Li-storage.[105,106,124] In agreement with the inferences drawn from the studies done with film electrodes, Mickelson *et al.*[124] reported that the major sources of stress development in graphitic carbon electrodes are the classical Li-intercalation between the constituent graphene layers and SEI layer formation. The measured stress magnitudes due to lithiation and delithiation were ~(−)3.7 ± 0.4 and ~(+)1.9 ± 0.2 MPa, respectively. Similar to the observations made by Sethuraman *et al.*,[5] very faint signatures of 'stress plateaus' during the 'staging' transitions of graphitic carbon upon Li-intercalation/de-intercalation were seen even in the *in situ* stress profiles. This aspect needs better understanding in the case of graphitic carbon based electrodes. Nevertheless, the stress data were also used to estimate the in-plane 'composite' bi-axial modulus of the graphite electrode, which was found to be as low as ~2.3 ± 0.5 GPa due to the presence of voids, binders and conductive additives.

With regard to the stiffness, by monitoring the stress and strain responses simultaneously during electrochemical lithiation/delithiation, Tavassol *et al.*[106] indicated that the stiffness of graphitic carbon based composite electrodes

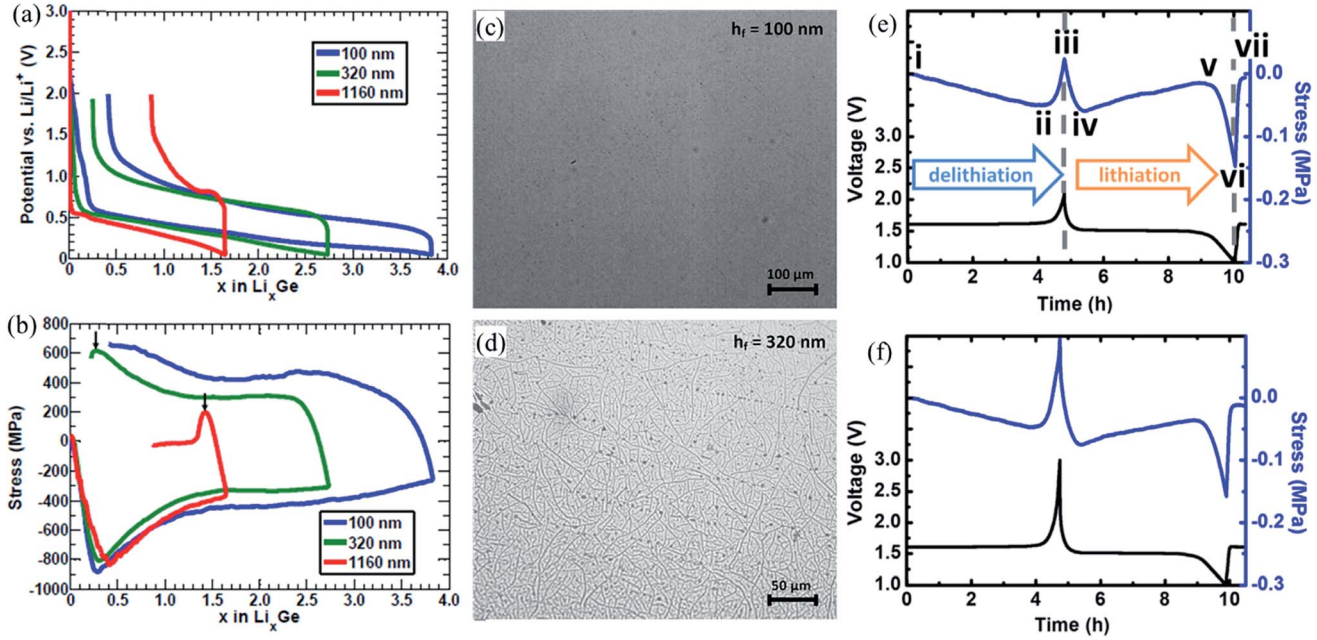

Fig. 11 (a) Voltage and (b) *in situ* stress responses of amorphous Ge films of different thicknesses during galvanostatic lithiation/delithiation cycles between 2.0 and 0.05 V *vs.* Li/Li^+ at a current density equivalent to C/16. The SEM images of the a-Ge films obtained after the 1st cycle, (c) showing no crack present for the 100 nm thick a-Ge film, (d) whereas cracks can be seen for the thicker a-Ge film (*viz.*, 320 nm thick) (reproduced with permission.[67] Copyright 2015, Elsevier). Voltage and *in situ* stress profiles of composite $Li_4Ti_5O_{12}$ (LTO) electrodes when galvanostatically cycled at C/5 between voltage ranges of (e) 1.02.1 V and (f) 1.0–3.0 V, *vs.* Li/Li^+ (reproduced with permission.[127] Copyright 2013, Elsevier).

changes with the degree of lithiation (referred to as 'electrochemical stiffness'). Initially, the formation of disordered dilute stage I of Li-GICs (*i.e.*, at ~0.3 V *vs.* Li/Li^+, during lithiation) resulted in lowering of the 'electrochemical stiffness'. By contrast, the formation of more ordered Li-GICs at ~0.24 (*i.e.*, stage IV Li-GIC), ~0.13 (*i.e.*, stage II Li-GIC) and ~0.08 V (*i.e.*, stage I Li-GIC) (*vs.* Li/Li^+) upon continued lithiation caused the 'electrochemical stiffness' to increase (see Fig. 10c–f). The steep increase in the 'electrochemical stiffness' just before the formation of the first ordered phase (*viz.*, stage IV Li-GIC) was associated with the hindrance to Li-ion transport, causing a considerable stress gradient. It was also found that the mechanical responses of graphitic carbon electrodes are rate dependent, with the stress magnitudes decreasing with decreasing voltage scan rates (in cyclic voltammetry) due to the strong dependence of Li-insertion/removal (and associated gradients) on kinetics, but with the strains increasing with decreasing scan rates due to more Li being inserted.

4.4. For other anode materials

Similar to the cases of Si (and also Sn), compressive stress development, followed by stress release due to plastic deformation, was observed during electrochemical Li-alloying of amorphous germanium (a-Ge) film electrodes.[63,67,76,112,125,126] However, the overall magnitude of the stress developed in the case of a-Ge was less than that for Si. Accordingly, plastic deformation of Ge films was found to occur at a relatively low compressive stress level of ~(−)0.76 GPa during lithiation (see Fig. 11a and b). Nevertheless, similar to that of Si, the elastic modulus of Ge was found to decrease upon lithiation from ~95 ± 10 GPa (pristine a-Ge film) to ~22–36 GPa (upon lithiation).[67]

With regard to cracking and degradation, discontinuity in the *in situ* stress profiles for thicker a-Ge films (*viz.*, 320 and 1160 nm thick films) indicates that thicker films get cracked during the first cycle itself, whereas the thinner film (*viz.*, 100 nm thick film) remains crack free (Fig. 11c and d). The stress development and cracking of a-Ge film electrodes were found to be sensitive to the rate of lithiation/delithiation (*via* the current density or C-rate),[76] similar to the case of Si film electrodes.[67] The fracture energies, estimated at different degrees of lithiation of the Ge film (*viz.*, 8.0 J m^{-2} and 5.6 J m^{-2} for a-$Li_{0.3}Ge$ and a-$Li_{1.6}Ge$, respectively), are indicative of brittle fracture and embrittlement upon lithiation[67,76] (similar to the case of Si[11,101]).

Observations similar to the case of Sn was made by us with aluminium (Al) film electrodes, such as the development of compressive stress initially during lithiation in the solid-solution regime, followed by flattening of the stress response and stress release due to plastic deformation and cracking during the 1st order phase transformation from Al to an Al–Li intermetallic phase.[55] More importantly, it was observed that inducing a pre-cycling tensile residual stress [of ~(+)1 GPa] was beneficial towards improving the structural integrity and electrochemical/cycle stability of Al film electrodes, with the signatures of 'stress release' in the *in situ* stress profiles getting suppressed in the presence of the pre-cycling residual stress. Furthermore, the tensile residual stress also reduced the

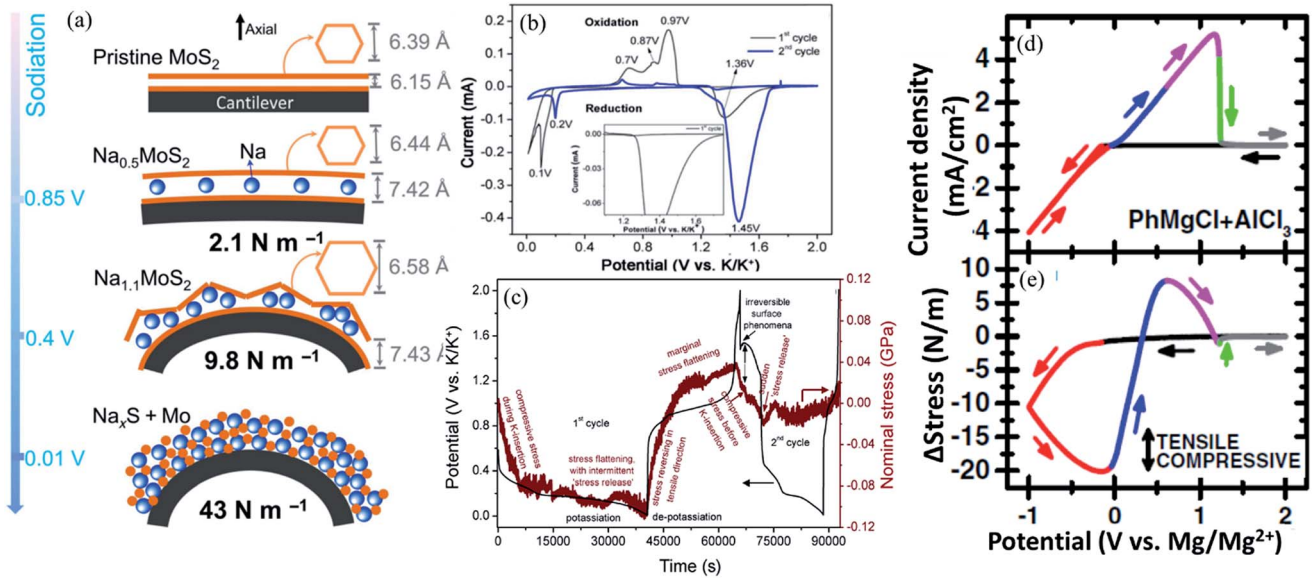

Fig. 12 (a) Schematic illustration of the various stages, corresponding inter-planar distances and stress evolution during sodiation of few layer MoS_2 (reproduced with permission.[128] Copyright 2019, The Authors, some rights reserved; exclusive licensee American Association for the Advancement of Science). (b) The first two cyclic voltammograms in a K 'half cell' for a 1 μm thick Sn film electrode, indicating the occurrence of irreversible surface reactions during anodic scans. (c) Voltage and *in situ* stress profiles obtained during the first two galvanostatic cycles (between 0.01 and 2.0 V *vs.* K/K^+) of the Sn film electrode (reproduced with permission.[54] Copyright 2017, The Electrochemical Society). (d) Cyclic voltammogram of the working Pt cantilever electrode against Mg foil (as the counter and reference electrode) during Mg-deposition/stripping using an 'all phenyl complex' electrolyte and (e) the corresponding evolution of surface stress response (reproduced with permission.[107] Copyright 2016, The Electrochemical Society).

overpotential needed for initiation of the Al → Al–Li phase transformation and hysteresis between the lithiation and delithiation potentials. This highlights the importance of engineering the initial stress state towards achieving improved electrochemical performance and cycle stability in an insertion electrode.

With respect to an oxide anode material, *viz.*, $Li_4Ti_5O_{12}$ (LTO), negating the erstwhile speculation as to it exhibiting 'zero strain' upon lithiation/delithiation, Choi *et al.*[127] reported the development of stresses during electrochemical cycling of LTO-based composite electrodes using the cantilever method. During lithiation and delithiation within a narrow voltage range of 1.45–1.65 V (*vs.* Li/Li^+), linear development of tensile and compressive stresses, respectively, was noted, which were due to contraction of the volume upon the formation of $Li_7Ti_5O_{12}$ during lithiation and reversal of the same, primarily during the potential plateau at ~1.55 V (*vs.* Li/Li^+). Of course, the overall stress magnitude was only ~50 kPa, which is significantly less compared to the other anode materials discussed above, and indicates that the lattice strain, even though not zero *per se*, is fairly small. However, much greater stress build-ups (up to even larger by a factor of ~70) were noted upon lithiation/delithiation beyond the plateau voltage due to volume expansion upon 'over-lithiation' past $Li_7Ti_5O_{12}$ (leading to compressive stress) and reverse upon 'under-lithiation' past $Li_4Ti_5O_{12}$ stoichiometries (see Fig. 11e and f). The above observations indicate that the integrity and cycle stability of LTO-based anode materials can suffer considerably upon going to potentials considerably away from the plateau potential.

4.5. For anode materials beyond the Li-ion chemistry

With a recent surge towards looking beyond the Li-ion battery system due to the localized and more expensive Li-precursors compared to Na-, K- and Mg-precursors, a few reports are available on the measurement of stress development in anode materials for the upcoming battery systems. For example, very recently Li *et al.*[128] monitored the stress development in 2H-MoS_2 based electrodes during electrochemical Na-insertion/removal using the cantilever method. The *in situ* experiments allowed stresses to be measured at different stages of sodiation, *viz.*, during Na-intercalation in-between the constituent MoS_2 layers at potential plateaus of ~0.85 and ~0.4 V *vs.* Na/Na^+ and conversion to Mo and Na_xS particles at ~0.1 V. While stress thicknesses corresponding to the compressive stress development during the first two stages were just ~(−)2.1 and ~(−)9.8 N m^{-1}, those associated with the conversion reaction were ~(−)43 N m^{-1} (see Fig. 12a). In fact, the well-defined potential plateau at ~0.1 V (*vs.* Na/Na^+) was not observed beyond the first sodiation half cycle, in complete contrast to the potential plateau at ~0.85 (*vs.* Na/Na^+). This indicates that the conversion reaction is likely to contribute primarily towards the mechanical/cycle instability of MoS_2-based electrodes for Na-ion cells.

With respect to the K-ion battery system, our work concerning *in situ* monitoring of the stress development during electrochemical K-alloying/de-alloying in Sn film electrodes indicated the occurrence of severe mechanical instability during 1st order phase transformations between Sn and Sn–K

intermetallic phases (*viz.*, K_4Sn_4), as well as during the irreversible surface reactions[54] (see Fig. 12b and c). The post-cycling observations confirmed the above inferences drawn from the *in situ* stress profile.

In the context of a 'Mg metal' battery system, Ha *et al.*[107] studied the mechanisms concerning electrochemical Mg deposition on and stripping from Mg metal (on different crystallographic planes) in the presence of different electrolytes *via* monitoring the stress development *in situ* using the cantilever technique (complemented by DFT calculations). It may be pointed out here that unlike in the case of Li- or Na-ion systems, the possibility of using Mg metal as the anode itself (due to less or negligible propensity towards dendrite formation under the concerned conditions), is promising in terms of the potential energy density of 'Mg metal' cells. With regard to the stress response, overall, a similar stress response was observed for all the four electrolytes. During the deposition half cycle (or cathodic scan), a slight compressive stress was developed due to adsorption of Mg-ion/anion/solvent complexes, followed by a steeper compressive stress development due to deposition of Mg in the form of nuclei (but sans crystallization). During the reverse scan, compressive stress continued to build up till the onset of Mg stripping, which, then caused the development of steep tensile stress, followed by compression (associated with the formation of MgO) and again tension, with the stress level ultimately returning to the level where it was prior to the start of the deposition process (see Fig. 12e and f).

5. Real-time monitoring of stresses and the associated instabilities in cathode materials

As compared to anode materials, investigations pertaining to *in situ* monitoring of stress development in cathode materials have been relatively sparse. This is possibly because it was believed that the relatively less lattice strains accompanying Li-extraction/insertion would not cause considerable mechanical degradation. However, it is often overlooked that even a much smaller strain (such as ~0.1%) may be considered fairly severe for brittle ceramic materials classes (such as oxides, phosphates *etc.*), which form the usual cathode materials,[1,33,129] unlike metallic materials and graphitic carbon, which form the usual anode materials. In fact, quite a few pieces of evidence indicate the development of deformation induced defect substructures and cracks in $LiCoO_2$,[130,131] $LiFePO_4$ (ref. 132) and $LiNi_xMn_yCo_{1-x-y}O_2$.[133–135] Furthermore, chemo-mechanical breakdown of layered Li-T_M-oxide based cathode materials due to phase transformation and oxygen release during Li-extraction has been recognized as one of the major issues with the concerned cathode materials.[133–135]

In the first reported work concerning *in situ* monitoring of stress development in cathode materials, we used a ~100 nm thick *c*-axis orientated $LiCoO_2$ (LCO) film electrode (as deposited *via* the pulsed laser deposition technique) and monitored

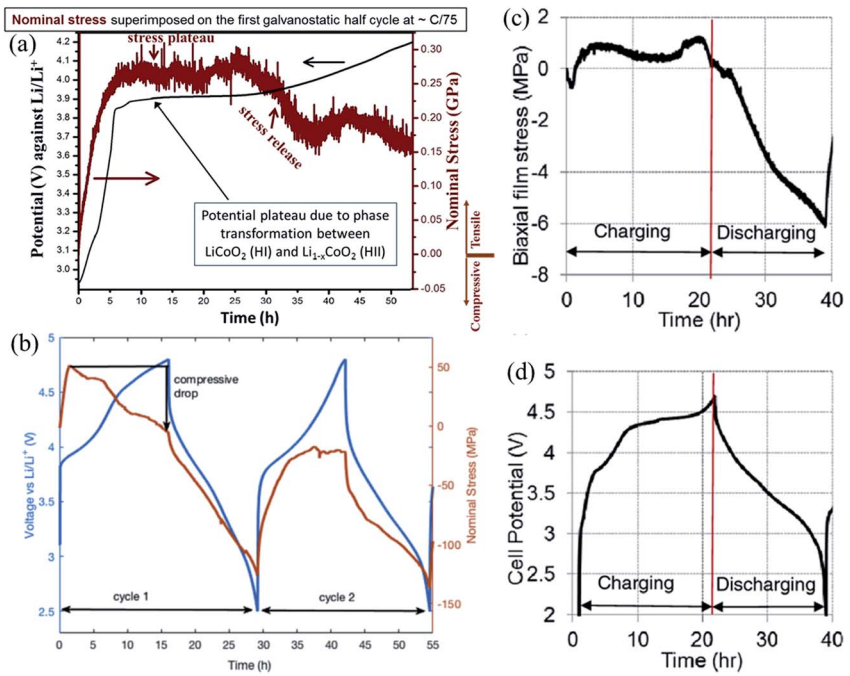

Fig. 13 Potential profiles and *in situ* stress obtained for (a) 100 nm thick $LiCoO_2$ film electrode during the 1st galvanostatic delithiation (or charging) half cycle (up to 4.2 V *vs.* Li/Li^+) at a current density equivalent to C/75 (reproduced with permission.[24] Copyright 2015, The Electrochemical Society) and (b) 1 μm thick Li-excess Li-transition metal oxide (Li-T_M-oxide; $Li_{1.2}Ni_{0.125}Mn_{0.55}Co_{0.125}O_2$) film electrode during the first two galvanostatic delithiation/lithiation cycles between 2.5 and 4.8 V *vs.* Li/Li^+ (reproduced with permission.[26] Copyright 2017, Elsevier). (c) *In situ* stress and (d) voltage profiles obtained with a slurry cast Li-excess Li-T_M-oxide composite cathode (*viz.*, $Li_{1.2}Ni_{0.15}Mn_{0.55}Co_{0.1}O_2$) when galvanostatically cycled at C/20 in the 'full cell' configuration against a composite graphite anode (reproduced with permission.[27] Copyright 2015, The Electrochemical Society).

the stresses during electrochemical delithiation and lithiation using the MOSS.[24] During the initial delithiation up to $x \sim 0.1$ for $Li_{1-x}CoO_2$, *i.e.*, until ~3.9 V (*vs.* Li/Li^+), fairly monotonous development of the tensile stress was noted up to ~(+)0.3 GPa due to contraction along the *a*-axis (*viz.*, the in-plane direction) by ~0.12% within the initial HI phase (where H stands for hexagonal) (see Fig. 13a). However, upon further delithiation (*i.e.*, from $x \sim 0.1$ to ~0.22 in $Li_{1-x}CoO_2$) when phase transformation from HI to HII takes place, 'flattening' of the stress response, followed by continuous 'stress release', was observed, until the upper cut-off potential of 4.2 V (*vs.* Li/Li^+) was reached (Fig. 13a). Such observations were attributed to mechanical instability (including cracking) in the film electrode during the two-phase co-existence, as also confirmed by *ex situ* SEM observations. Similar to the case of Sn film electrodes, as discussed in Section 5.2, the additional internal stress associated with the nucleation and growth of the 2nd phase during the phase transformation was believed to be the cause for such an instability.

Moving ahead from $LiCoO_2$, using a sputter deposited ~1 μm thick film of Li-excess Li-T_M-oxide having the composition $Li_{1.2}Ni_{0.125}Mn_{0.55}Co_{0.125}O_2$, Nation *et al.*[26] also observed a somewhat similar stress response. Again, in this case, monotonous development of the tensile stress [up to ~(+)150 MPa] was observed during the initial period of delithiation until ~4 V (*vs.* Li/Li^+), but which was followed by fairly monotonous 'stress release' over the entire remaining delithiation half cycle (till ~4.8 V; *vs.* Li/Li^+) (see Fig. 13b). In fact, the 'stress release' (or build-up of compressive stress) in this case was much steeper, as compared to that for LCO, resulting in the development of net average compressive bi-axial stress (by a few MPa) by the end of the delithiation half cycle. Unlike the proposed hypothesis for LCO, SEM observations ruled out cracking as the cause for the 'stress release' or the compressive stress build-up in the case of the $Li_{1.2}Ni_{0.125}Mn_{0.55}Co_{0.125}O_2$ film electrode. The formation of a surface spinel structure (which is, in fact, denser) and/or SEI layer would also not account for the observed compressive stress development in the 1st cycle. Nevertheless, the net expansion of the lattice due to oxygen release upon charging beyond 4.5 V (*vs.* Li/Li^+) was proposed as the cause for the irreversible compressive stress development during the first delithiation half cycle, which was also supported by DFT-based calculations. In a different work, *in situ* stress measurements by Nadimpalli *et al.*[27] with a Li-excess Li-T_M-oxide ($Li_{1.2}Ni_{0.15}Mn_{0.55}Co_{0.1}O_2$) based porous 'composite' electrode (*viz.*, having a binder and C black) in Li-ion 'full cells' (*viz.*, against graphitic carbon anode) again indicated instabilities in the stress response after the initial monotonic build-up of tensile stress up to a 'full cell' voltage of ~3.8 V during delithiation (see Fig. 13c and d). This was somewhat similar to the observations made earlier with the LCO[24] and later with Li-T_M-oxide[26] film electrodes. However, despite pronounced 'stress flattening', the 'stress release' towards the compressive direction was not pronounced at all, unlike the observations made with the Li-T_M-oxide film electrode.[26] In fact, a net average bi-axial tensile stress of ~(+) 1.5 MPa got developed at the end of the delithiation half cycle (*viz.*, at an upper cut-off 'full cell' voltage of 4.7 V). Nevertheless, fairly monotonous build-up of compressive stress was noted during the lithiation half cycle, with the net average bi-axial stress attaining a value of ~(−)6 MPa at the end (*viz.*, at a lower cut-off 'full cell' voltage of 2.0 V). Even though it is not clear as to what all may have caused the difference in the stress response during the delithiation half cycle between the studies by Nation *et al.*[26] and Nadimpalli *et al.*,[27] the type of electrode used (*viz.*, film *vs.* 'porous composite') and the crystallographic orientations with respect to the in-plane direction are definitely some of the factors. However, the type of electrode is expected to primarily influence the magnitude of the average bi-axial stress, rather than the nature of the stress profile.

While monitoring the stress development during electrochemical delithiation of the $LiMn_2O_4$ film electrode (prepared by spin coating of the corresponding sol), Sheth *et al.*[25] observed a fairly steady build-up of tensile stress up to ~(+) 1.45 GPa (at a potential of 4.05 V *vs.* Li/Li^+) due to lattice contraction, but which was followed by 'stress release' until the end of the first delithiation half cycle. Thus, the tensile stress level eventually decreased to ~(+)1.3 GPa at the end of

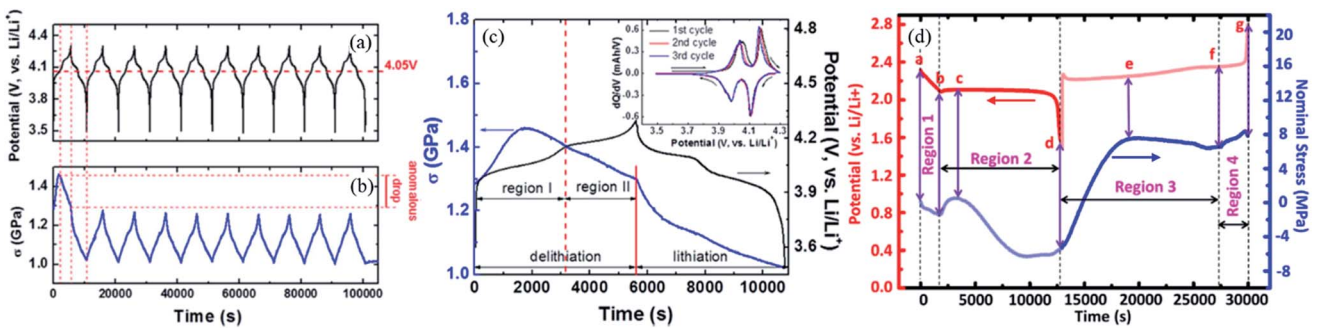

Fig. 14 (a) Voltage and (b) *in situ* stress profiles of a 150 nm thick $LiMn_2O_4$ film electrode during the first ten galvanostatic delithiation/lithiation cycles, along with (c) zoomed-in view of the voltage and stress profiles during the 1st cycle, showing steady build-up of tensile stress up to ~(+) 1.45 GPa until ~4.05 V *vs.* Li/Li^+, but continuous stress release after that until the end of delithiation (reproduced with permission.[25] Copyright 2016, The Electrochemical Society). (d) Potential and *in situ* stress profiles for a composite sulphur cathode (50% S, 40% conductive additive and 10% binder) during the 1st lithiation/delithiation cycle (reproduced with permission.[136] Copyright 2018, Elsevier).

the first delithiation half cycle (*viz.*, at 4.3 V; *vs.* Li/Li^+). Nevertheless, a fairly steady compressive stress build-up was noted during the lithiation half cycle, as expected based on the associated lattice expansion (see Fig. 14a–c). Qualitatively, such observations with the $LiMn_2O_4$ electrode are somewhat similar to those with the LCO and Li-excess Li-T_M-oxide electrode (as discussed earlier). In the absence of evidence concerning mechanical instabilities and the predominant influences of surface reactions, the anomalous 'stress release' during the first delithiation half cycle was attributed to irreversible changes in the bulk structure (*viz.*, oxygen loss and/or loss in crystallinity). Of course, post the first cycle, the stress build-up was fairly monotonous and reversible for $LiMn_2O_4$, being tensile and compressive during the delithiation and lithiation half cycles, respectively.

In possibly the only work concerning *in situ* stress measurements with S-based cathodes, Zhang *et al.*[136] used a spin-coated film electrode composed of a mixture of 50% S, 40% carbon (graphite + C black) and 10% binder. During the discharge or lithiation half cycle, monotonous compressive stress development was recorded during the initial conversion of S_8 to the soluble Li_2S_n ($n = 8$, 6 and 4) liquid polysulphides. The next step or the elongated potential plateau, which corresponds to the deposition of solid Li_2S_n and conversion to Li_2S (*via* intermediate Li_2S_2), first produced tensile stress, followed by compressive stress, somewhat akin to the nucleation and growth process of solid islands during film deposition. Part of the compressive stress was also attributed to 30% volume expansion during the $Li_2S_2 \rightarrow Li_2S$ transformation (see Fig. 14d). A flattening of the stress response, as seen towards the end of only the 1st lithiation half cycle, was tentatively attributed to either slowing down of deposition or plastic deformation of the Li-sulphide. During delithiation, dissolution of Li_2S caused the development of tensile stress, which was followed by almost no change in stress due to the subsequent conversions happening in the liquid state. Towards the end of delithiation, deposition of the higher order poly-sulphides caused development of tensile stress, followed by compressive stresses, again, akin to the nucleation-growth process during film deposition. Nevertheless, the complex nature of the conversions during lithiation/delithiation of the S electrode demands further studies pertaining to *in situ* stress measurements with different electrode types/morphologies in order to better understand the stress responses and the associated processes.

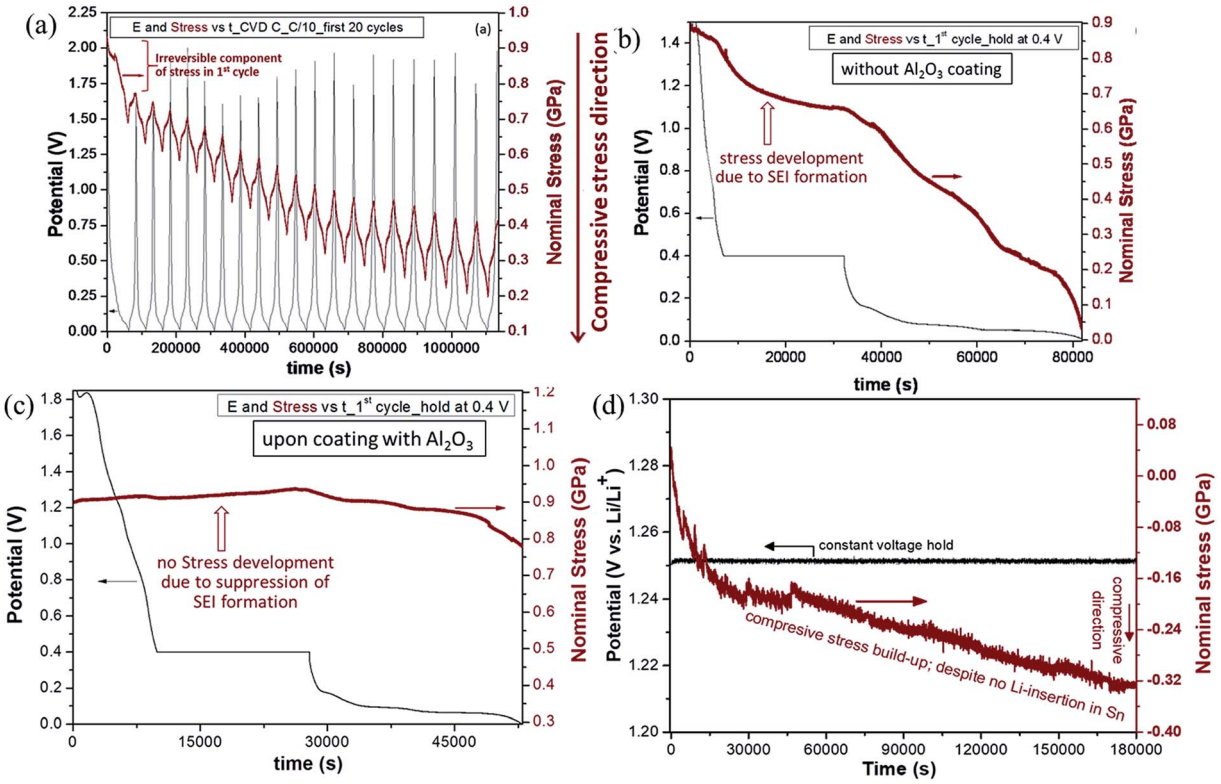

Fig. 15 A few examples for the detection of irreversible stress development due to SEI layer formation on electrodes during *in situ* monitoring stress development during galvanostatic lithiation/delithiation (in Li 'half cells'). The voltage and *in situ* stress profiles obtained with a ~200 nm thick (a) CVD-grown graphitic carbon film electrode during the first 20 cycles at C/10, (b) the same type of graphitic carbon film electrode during the 1st lithiation half cycle with an intermittent holding at 0.4 V *vs.* Li/Li^+ (*viz.*, where compressive stress development due to Li-intercalation is not expected), (c) the same type of graphitic carbon film electrode, but with a 0.5 nm thick Al_2O_3 coating (deposited *via* the atomic layer deposition technique), showing no compressive stress development during the 0.4 V hold, unlike that for the electrode sans the Al_2O_3 coating (reproduced with permission.[21] Copyright 2012, Elsevier) and (d) Sn film subjected to a constant voltage hold at 1.25 V *vs.* Li/Li^+ for 50 hours, showing continuous build-up of compressive stress (reproduced with permission.[54] Copyright 2017, The Electrochemical Society).

6. Real-time monitoring of stress development during irreversible surface reactions

The occurrence of irreversible surface reactions, including SEI layer formation, is one of the major problems in Li-ion cells, since it permanently consumes some fraction of the available Li-ions in the cell and also contributes towards capacity fade.[1–4,21,53,118,121–123,137,138] The irreversible surface reactions take place primarily during the 1st or first few cycles and start prior to Li-insertion in most anode materials.

As has been mentioned in Section 4.3, the compressive stress development during electrochemical Li-intercalation in *c*-axis oriented graphitic carbon based film electrodes was nearly completely reversed during the subsequent Li de-intercalation.[22] However, this was the case only from the 19th cycle onward, since prior to that the net compressive stress developed during the lithiation half cycle was not completely reversed during the delithiation half cycle, but remained 'locked-in' as irreversible compressive stress (see Fig. 15a and b).[21] In fact, a bulk of the irreversible compressive stress development took place during the very first cycle. It was also found that even though the irreversible compressive stress in the first cycle, as estimated by normalizing the stress-thickness (directly obtained from the substrate curvature; see Section 3) by the graphite film thickness, apparently decreased with increase in the film thickness, the stress-thickness values were actually the same irrespective of the film thickness. This indicated that that the irreversible compressive stress was not associated with the bulk of the 'active' graphite film, but was rather associated with the surface. Similar variations, but with opposite trends, of the irreversible stress and the 'coulombic efficiency' (known to be governed primarily by the irreversible surface processes) with the number of cycles and also the observation concerning initiation of the compressive stress from the electrochemical potentials where SEI formation is also known to get initiated indicated that the irreversible compressive stress was associated with SEI layer formation. Furthermore, coating of the graphitic carbon film with a very thin (<1 nm thick) layer of Al_2O_3 (*via* atomic layer deposition) prevented SEI formation and also the irreversible compressive stress development (see Fig. 15c). Accordingly, the above observations and supporting analysis of the electrochemical and associated stress profiles confirmed that the electrodeposition process leading to the formation of the SEI layer on the exposed basal plane of the graphite film leads to the development of the irreversible compressive stress. The overall magnitude of this irreversible compressive stress was found to be greater than that of the Li-intercalation induced compressive stress by factor of ~4 [*viz.*, ~(−)1 GPa for a 200 nm thick film]. A more detailed study indicated that disruption at the surface of the graphitic carbon film due to co-intercalation of solvent species, *viz.*, of a complex, composed of 1 Li^+, 0–2 PF_6^- (from $LiPF_6$ salt of the electrolyte) and 2–5 solvent ions (*i.e.*, EC and/or DEC) primarily during the 1st lithiation half cycle also partly contributes towards the irreversible component of stress.[53] In fact, the observations suggested that the stress associated with this disordered region formed close to the graphite surface may play a role in stabilizing the inorganic part of the SEI layer.

Similar to the graphitic carbon films, irreversible compressive stress build-up during the first 20 cycles with a net magnitude of ~(−)35 GPa nm of stress-thickness was recorded even with our *c*-axis oriented few layer graphene based electrodes (having ~7 constituent graphene layers). Such observations were also made in the case of multi-layered graphene film electrodes, having ~10 constituent graphene layers.[17] Again, with ~200 nm thick graphenic carbon films, having vertically aligned graphene layers, *i.e.*, *a*-axis oriented, development of irreversible compressive stress of ~(−)2 GPa was observed right in the first cycle.[20] This relatively greater magnitude of locked-in compressive stress associated with SEI formation on the edge planes (due to *a*-axis orientation), as compared to that on the basal planes (for the *c*-axis oriented graphitic carbon film[21]) for the same net film thickness, was believed to be due to the greater fraction of inorganic components in the SEI layer formed on the edge planes.[137] Hence, irrespective of the thickness and crystallographic orientation of the graphitic/graphenic carbon film, irreversible surface reactions, including SEI layer formation, result in the development of irreversible compressive stress. In fact, in a very recent work by Xie *et al.*,[138] even *in situ* Raman spectroscopic measurements with graphene nanoplatelets (GNPs) have indicated the development of compressive stress due to SEI layer formation (more details on such complementary *in situ* measurements will be presented in Section 7).

With 'porous composite' graphite electrodes (*viz.*, having a binder and conducting additive), Mickelson *et al.*[124] also observed initial overall compressive stress build-up prior to the onset of Li-intercalation, with SEI layer formation presumably contributing towards the same. However, in this work, the SEI layer itself was associated with a tensile stress of ~(+)1.6 MPa.

In the case of 'alloying reaction' based anode materials, like Si, Sn *etc.*, the colossal dimensional changes during electrochemical cycling render the SEI layer quite unstable such that it breaks and reforms at newly exposed electrode surfaces.[1–4] Hence, stresses associated with the SEI layer formation in such electrodes can have even greater implications towards the cycle stability. In a bid to remove the contribution from SEI layer formation towards the overall compressive stress development upon lithiation of Si film electrodes (where separating out stress development due to lithiation and SEI formation may be challenging), Nadimpalli *et al.*[11] first monitored the stress development due to SEI layer formation or growth during 'lithiation' of the Cu current collector film. It was found that the maximum stress-thickness associated with the SEI layer formed on the Cu film was ~(−)24 GPa nm. This implies that if the SEI layer on Si is similar to that on Cu, for a Si film electrode having a 100 nm thick SEI layer, the associated stress would be ~(−)240 MPa. This can be quite significant, especially considering that the SEI layer can grow even thicker due to continuous reformation.

In the case of Sn film electrodes, stress measurements during the initial lithiation *via* holding at 0.8 V (*vs.* Li/Li^+) for 20 h (*i.e.*, prior to Sn → Li_2Sn_5 phase transformation) showed a linear build-up of compressive stress up to an average compressive stress of ∼(−)16 MPa.[68] Nevertheless, further analysis suggested that the SEI layer formed was actually under a tensile stress of ∼(+)9 MPa, similar to the conclusion by Mickelson *et al.*[124] for composite graphite electrodes. By contrast, in one of our studies, *in situ* stress measurement during a constant voltage hold for 50 h at an even higher potential (*viz.*, ∼1.25 *vs.* Li/Li^+) indicated monotonous development of compressive stress [reaching ∼(−)0.3 GPa in 50 h] (see Fig. 15d).[54] This has to be associated with surface reactions, including SEI formation on the Sn film electrode, because Li-insertion into Sn at the concerned potential is not expected at all. In fact, as partly mentioned in Section 4.5, irreversible compressive stress development due to such surface reactions occurring at potentials between 1.5 and 1.2 V (*vs.* K/K^+) was found to be one of the primary reasons for the loss in mechanical integrity and cycle stability of Sn film electrodes during electrochemical K-alloying/de-alloying (as the anode material for upcoming K-ion battery systems). Here, it needs to be mentioned that despite irreversible surface reactions and SEI layer formation on the cathode side also influencing the electrochemical behavior of the same,[139–141] *in situ* monitoring of stress development is yet to be performed in that context.

7. Coupling with complementary information from other *in situ* techniques

In the previous sections, evaluation of various chemo-mechanical aspects associated with electrochemical cycling and stress development *via* curvature-based stress measurements conducted *in operando* has been discussed. Such measurements allow direct estimation of the magnitudes and observation of the behavioural patterns of stress development in electrodes during electrochemical cycling. However, various other *in situ* techniques have also been used to obtain complementary information pertaining to structural changes, deformation and evolution of strain (*i.e.*, dimensional changes) and integrity of electrode materials, often at micron- or nano-scale levels. In this context, inferences obtained from some of the more important and widely used techniques, such as *in situ* X-ray diffraction (XRD), Raman spectroscopy, transmission electron microscopy (TEM), scanning electron microscopy (SEM), focused ion beam (FIB), atomic force microscopy (AFM), and digital image correlation (DIC) have been discussed in the following.

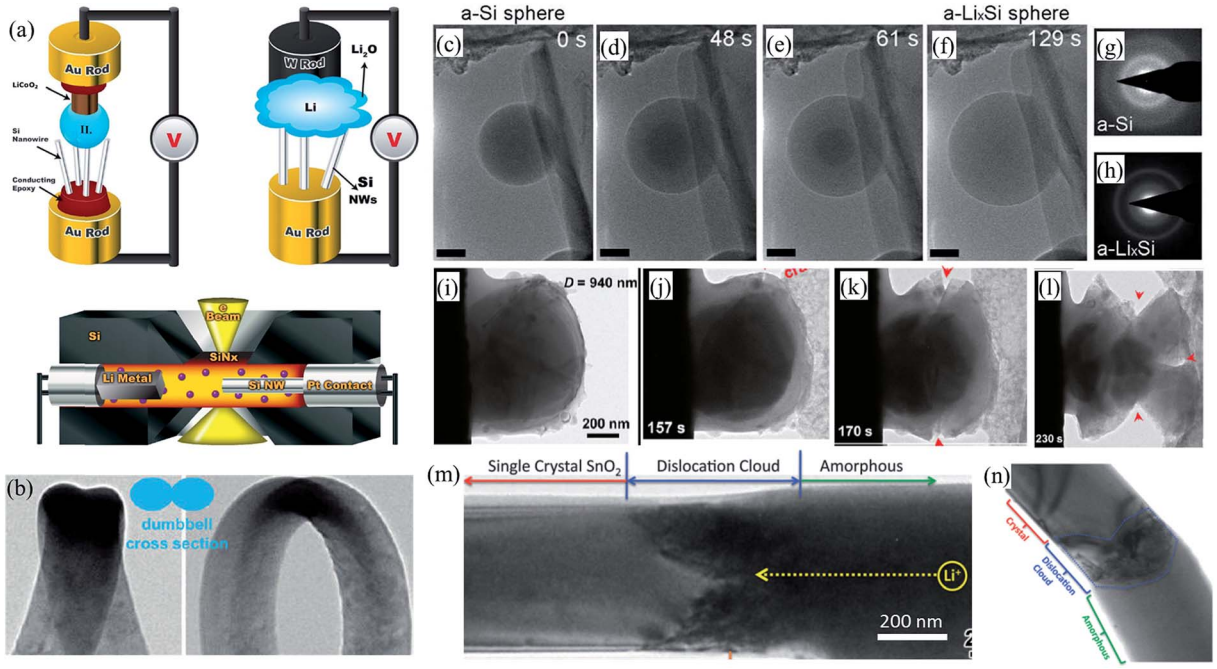

Fig. 16 (a) Schematic representations of a few types of electrochemical cells or 'micro-batteries' used for *in situ* TEM observations during electrochemical cycling (reproduced with permission.[263] Copyright 2013, American Chemical Society). (b) Dumb-bell shaped morphology evolution due to anisotropic lithiation of crystalline silicon (c-Si) nanowires (reproduced with permission.[142] Copyright 2011, American Chemical Society). (c)–(f) Morphological evolution of amorphous Si (a-Si) nanoparticles during lithiation (as observed during *in situ* TEM), showing the sequential disappearance of the unlithiated a-Si core, with SAED patterns obtained from the unlithiated and lithiated regions of the a-Si nanoparticle being presented in (g) and (h), respectively (reproduced with permission.[144] Copyright 2013, American Chemical Society). (i)–(l) Morphology evolution of c-Si particles of diameter 940 nm (*i.e.*, beyond the critical size of 150 nm for fracturing), showing anisotropic lithiation, onset of cracking and pulverization during lithiation (reproduced with permission.[86] Copyright 2012, American Chemical Society). (m) and (n) *In situ* TEM images of SnO_2 nanowires during lithiation, showing the migrating reaction front and 'dislocation cloud' at the reaction front, separating the crystalline unlithiated and lithiated amorphous regions[1,96] (reproduced with permission.[1] Copyright 2014, Elsevier).

7.1. *In situ* TEM

In situ TEM allows direct observations pertaining to the chemical/morphological/structural/phase changes taking place in an electrode material during electrochemical lithiation/delithiation, which can be helpful towards understanding the associated mechanistic/kinetic aspects and chemo-mechanical response. However, for such observations, the sample (*i.e.*, the electrode material) needs to be of a suitable (nano)dimension such that it is electron transparent and also the electrochemical lithiation/delithiation needs to be conducted inside a suitably modified TEM sample holder. Hence, specially designed electrochemical cells, usually containing the working electrode material either in the form of a single nanowire or nanosized particle, a miniature counter electrode, the electrolyte either in the form of a solid Li-oxide or liquid droplet and some mechanism to apply electrical bias to drive lithiation are used inside the TEM holder (see Fig. 16a).[96,143–153] Such investigations have been done extensively with the anode materials, such as Si,[142–146] SnO_2,[96,147,148] Sn,[149] Al,[150] Ge,[151] and TiO_2.[152,153]

While performing *in situ* TEM observations during electrochemical lithiation/delithiation of crystalline silicon (c-Si) nanowires, Liu *et al.*[142] observed the anisotropic lithiation behaviour of c-Si, with Li-diffusivity along the ⟨110⟩ direction being ~100 times faster than that along ⟨111⟩. Accordingly, upon lithiation the c-Si nanowires swelled more along the ⟨110⟩ direction (*viz.*, ~170% dilation in diameter), as compared to along ⟨111⟩ (*viz.*, only ~20% expansion) thus evolving into a dumbbell shape (see Fig. 16b). Such observations indicate that stress development during lithiation/delithiation of c-Si electrodes is also expected to be anisotropic, which is a matter of concern especially considering the magnitude of stress that gets developed in the case of Si. With respect to amorphous Si (a-Si), against the more common belief concerning single phase lithiation,[154,155] McDowell *et al.*[144] observed that the lithiation of a-Si nanoparticles during the first cycle takes place *via* a distinct two-phase process, as separated by the 'reaction' front between lithiated (*i.e.*, Li_xSi) and unlithiated a-Si (see Fig. 16c–h). In general, a closer look at the potential profiles recorded during lithiation of a-Si indicates that the profile corresponding to the first cycle is much flatter in appearance (with sharper features), as compared to that from the 2nd cycle onwards (see Fig. 5a and b). With regard to the mechanical integrity upon lithiation/delithiation of c-Si *vs.* a-Si, it was observed that while c-Si nanoparticles of ~150 nm diameter get fractured (Fig. 16i–l),[86] the critical size for getting fractured is much larger for a-Si particles, so much so that a-Si particles of up to 870 nm in diameter were not observed to get fractured. As already mentioned above, anisotropic lithiation in the case of c-Si is expected to negatively affect the mechanical integrity of the same. Furthermore, it was observed that the reaction front in the case of c-Si slows down drastically with increasing thickness of the lithiated portion, whereas that of a-Si does not slow down considerably with lithiation.[143] Thus the concentration gradient and hydrostatic stress are expected to be less in the case of a-Si.

The pioneering *in situ* TEM studies conducted during the lithiation of SnO_2 nanowires by Huang *et al.*[96] and Wang *et al.*[147] showed the progress of a reaction front from where the nanowire contacts the electrolyte to away from the nanowire/electrolyte interface, causing expansion in the radial, as well as longitudinal, direction of the nanowire getting lithiated. The reaction front was found to separate the unlithiated and lithiated regions of the SnO_2/Sn nanowires, leading to the formation of an amorphous/crystalline interface. It was adjacent to this interface that the unlithiated and lithiated regions were observed to experience large tensile and compressive stresses, respectively, which caused spontaneous nucleation of dislocations and associated plasticity (see Fig. 16m and n). This agrees with the observations made during *in situ* stress measurements of Sn-based electrodes, which indicated the occurrence of plastic deformation and loss in integrity primarily during the phase transformations[18,19,54,56] (as discussed in Section 4). In fact, the estimated dislocation density at the lithiation front, as per the *in situ* TEM observations, helped us estimate the flow stress of lithiated Sn (found to be ~1 GPa).[18,19] Furthermore, with increasing Li-concentration, the initially straight SnO_2 nanowires turned into bended, twisted and/or curled morphology, which is the indication of lithiation induced severe plastic deformation. Wang *et al.*[147] demonstrated that the dispersion of Li_xSn particles in the Li_yO matrix, as formed during lithiation, improves the structural integrity of the SnO_2 nanowires. With carbon coated Sn nanowires, *in situ* TEM observations by Li *et al.*[149] revealed that large grains of pristine Sn get converted into finer crystalline $Li_{22}Sn_5$ grains of a few nanometers in dimension, thus ruling out the formation of amorphous Li_xSn phases.[156] It was also observed that during the 1st lithiation Sn experienced ~324% volume expansion, but which could not be fully recovered after one complete cycle due to pulverization of lithiated Sn during delithiation.

In situ TEM has also been used to look into the structural evolutions during sodiation/desodiation of Sn. Wang *et al.*[157] observed that sodiation of Sn nanoparticles occurs in two steps. In the first step (*i.e.*, until $x = 0.5$ for Na_xSn), sodiation takes place *via* a two-phase mechanism, *viz.*, un-sodiated Sn and poorly sodiated amorphous Sn (*i.e.*, $NaSn_2$) being separated by a moving reaction front. Following this, the second step of sodiation (*i.e.*, till $x = 3.75$) takes place *via* sequential formation of various intermediate Na_xSn phases (*viz.*, amorphous Na_9Sn_4 and Na_3Sn) until the formation of crystalline $Na_{15}Sn_4$. More importantly, a huge overall volume change was observed during sodiation, with the volume change being ~60% during the first step and ~420% during the second step (which renders the latter detrimental towards the mechanical integrity of the electrode). Nevertheless, no signature of mechanical degradation of Sn nanoparticles could be observed in this work under the associated conditions, within the concerned time frame and for the particle size of Sn used.

During the lithiation of Al nanowires having a ~5 nm thick naturally grown native oxide (*i.e.*, Al_2O_3) layer, Liu *et al.*[150] observed that the native Al_2O_3 layer got lithiated prior to the Al. Due to the early lithiation of the Al_2O_3 layer, a Li–Al–O type glass sheath/tube is formed around Al, which provides structural stability to the nanowires undergoing the lithiation/delithiation. Unlike Si[142–146] and Ge[151] (as discussed later in

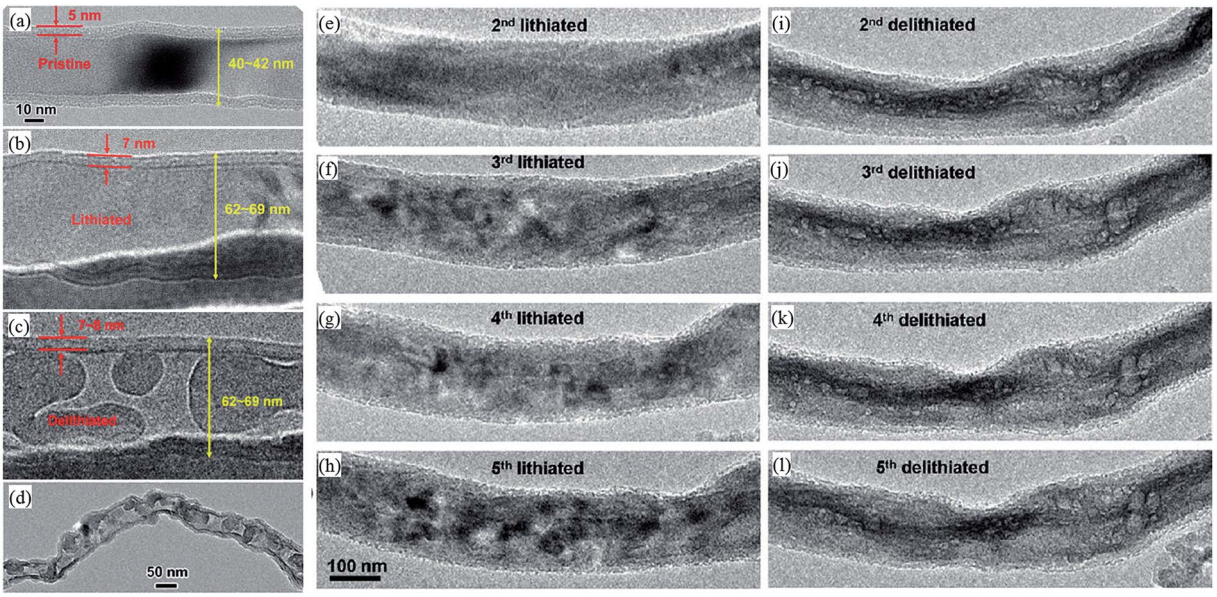

Fig. 17 A few examples of *in situ* TEM observation during electrochemical lithiation/delithiation of (a)–(d) Al nanowires (reproduced with permission.[150] Copyright 2011, American Chemical Society) and (e)–(l) a-Ge nanowires (reproduced with permission.[158] Copyright 2011, American Chemical Society). (a) Pristine Al nanowire having a native coating of Al_2O_3, (b) with the Al_2O_3 coating reacting first, followed by Al, during lithiation, (c and d) causing the appearance of voids and pulverization by the end of delithiation. (e)–(l) Ge nanowires showing the 'memory effect' of pores/void formation during electrochemical lithiation and delithiation, *viz.*, voids/pores disappearing during lithiation and reappearing with almost similar size and at same location during delithiation.

this section), Al nanowire electrodes did not undergo solid state amorphization but rather got converted into polycrystalline Li_xAl. However, during delithiation, nanosized voids were formed, whose population and size increased with the degree of delithiation, eventually leading to pulverization of the Al nanowires (Fig. 17a–d). Accordingly, *in situ* TEM observations confirmed that the loss in integrity happens primarily during the delithiation step.

In situ TEM observations made by Liu *et al.*[158] during lithiation of crystalline Ge (c-Ge) indicated that it undergoes lithiation *via* two phase transformations happening in sequence. Initially the c-Ge nanowire undergoes solid state amorphization, only to later get converted to crystalline $Li_{15}Ge_4$ (*viz.*, the most Li-rich phase of Ge). Similar to Si, the reaction front was observed to move from the surface to core, leading to the formation of a core–shell structure composed of a crystalline Ge core, surrounded by amorphous Li_xGe.[151] Again, similar to the case of Si,[142–146] the lithiation kinetics was observed to either slow down or cease with increasing degree of lithiation due to the large lithiation induced compressive stress. Similar to the case of Al, pores/voids were observed to form in the Ge nanowires during delithiation, bestowing it with a sponge-like appearance. Interestingly, due to the preferential and rapid Li-transport along the internal surfaces of the pores as compared to bulk Ge, a type of 'memory effect' was observed with regard to the formation of pores/voids in the subsequent cycles, with the pores/voids disappearing during lithiation and re-appearing (with similar size/shapes and at similar locations) during delithiation (see Fig. 17e–l).[158]

Even though not as extensively studied as the anode materials, *in situ* TEM observations during electrochemical cycling have also been made with a few cathode materials, such as $LiCoO_2$,[159] $Li_xNi_yMn_zCo_{1-y-z}O_2$ (Li-NMC),[160] and $LiFePO_4$.[161] Hwang *et al.*[160] investigated the critical role played by the stoichiometry of Li-NMC in the balance between thermal stability and energy density. It was found that in the discharged (or lithiated) state, Li-NMCs maintained their surface, crystallographic and electronic structures, irrespective of the composition, *viz.*, NMC811, NMC622 and NMC433, where the numbers denote the ratio of the transition metal elements present. For NMC811, despite possessing the maximum Li-storage capacity, thermal stability was found to be minimal during charging and it underwent changes in the surface, crystallographic and electronic structures at 100 °C. On the other hand, NMC622 exhibited excellent thermal stability. The inferences from this work further indicate that it will be interesting and informative to study the stress development during delithiation/lithiation of the different Li-NMCs as a function of temperature. Karakulina *et al.*[161] conducted *in situ* electron diffraction tomography using TEM to investigate the changes in the unit cell of $LiFePO_4$ in detail during electrochemical cycling. Additionally, electron irradiation induced phase transitions in $LiFePO_4$ and Li_2FeSiO_4 and the associated structural changes have been investigated using *in situ* TEM.[162]

7.2. *In situ* AFM

In situ AFM scans during electrochemical lithiation/delithiation have been used to investigate structural/mechanical changes occurring in the bulk (*viz.*, volume change, fracture/cracking

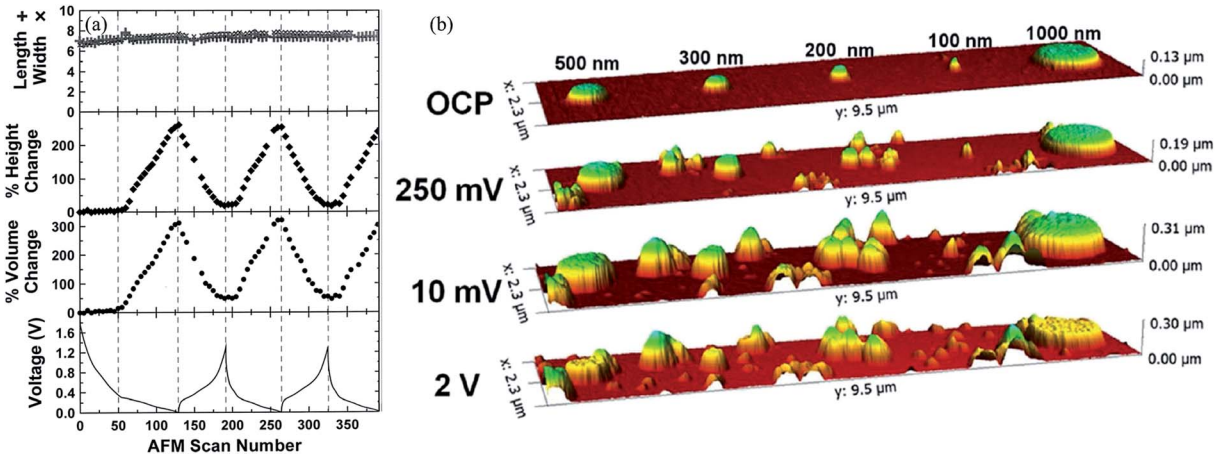

Fig. 18 (a) *In situ* AFM observations during electrochemical lithiation/delithiation, showing the variations in the length (+), width (×), % change in height and % change in volume for a-Si tower/island during the first two and a half cycles (reproduced with permission.[165] Copyright 2003, The Electrochemical Society). (b) 3D images as obtained *via in situ* AFM scans at different stages during lithiation and delithiation of Si nano-pillars of different diameters (*viz.*, 100, 200, 300, 500 and 1000 nm), showing lateral and vertical changes in diameter and height (reproduced with permission.[167] Copyright 2013, American Chemical Society).

etc.) and at the surface (*viz.*, SEI formation) of electrodes. In one of the earlier studies, using *in situ* AFM, Aurbach and Cohen[163] observed that a surface layer (now known as SEI layer) gets deposited on the Cu substrate at potentials higher than the potential of actual Li-deposition. Dahn and co-workers[164] detected the occurrence of surface corrugation/roughness during lithiation of Si–Sn alloy films. In another set of studies related to *in situ* AFM studies during lithiation/delithiation of a host of 'alloying reaction' based anode materials, it was observed by Beaulieu *et al.*[165] that the Si–Sb film gets cracked during delithiation, with the cracks getting more pronounced with repeated cycling. In the same work, for a-Si and amorphous $Si_{0.64}Sn_{0.36}$ (a-$Si_{0.64}Sn_{0.36}$) film electrodes, the volumetric and morphological changes were found to be reversible upon lithiation and delithiation (Fig. 18a). However, it was not the same for crystalline Al and Sn film electrodes, which exhibited inhomogeneous-cum-nonlinear and irreversible volume changes due to irreversible structural/morphological changes during lithiation and delithiation.[165,166] During electrochemical cycling, the average volume changes experienced by a-Si and a-$Si_{0.64}Sn_{0.36}$ were ~311% and ~289%, respectively. In another work by Dahn's group,[166] *in situ* AFM studies could correlate the observation of a voltage plateau at ~1.6 V (*vs.* Li/Li^+) during lithiation of Sn to SEI layer formation. Upon bypassing the formation of the surface layer by rapidly lowering the potential to ~0.8 V (*vs.* Li/Li^+), the dimensional changes occurring during lithiation/delithiation of Sn were monitored in fairly reliable terms. In fact, these results formed the basis for estimating the 'corrected stress' (*viz.*, those taking into account the changes in film thickness during lithiation) from the substrate curvature values obtained by us in real-time using the MOSS during lithiation of Sn film electrodes.[18,19] Overall, the ability to observe the dimensional changes in real-time in all directions (*i.e.*, in-plane and out-of-plane) and also the occurrence of cracking during electrochemical cycling *via in situ* AFM was thoroughly established from the above studies.

In situ AFM observations during electrochemical cycling of Si nano-pillars of constant height (~100 nm), but different diameters (varying from ~100 to ~1000 nm) revealed that those having diameter >~200 nm got fractured during continued electrochemical cycling (see Fig. 18b).[167] Interestingly, while the volume expansion upon lithiation, as observed with the 'thicker' nano-pillars, was ~300%, the expansion was only ~150% for the pillar having an initial diameter of ~100 nm. Nevertheless, all the pillars adopted a porous morphology after lithiation/delithiation, suggesting the loss in mechanical integrity. Again, it was this study by Becker *et al.*,[167] which, coupled with the *in situ* AFM observations made by Beaulieu *et al.*[165] and the results obtained by Jerliu *et al.*[168] from *in situ* neutron reflectometry studies during lithiation of a-Si film electrodes, allowed us to estimate the 'corrected stress' values from the *in situ* substrate curvature measurements in the case of lithiation/delithiation of Si and Si/graphene film electrodes.[17] He *et al.*[169] also recorded volume expansion/contraction by ~300% *via in situ* AFM during lithiation/delithiation of Si, which was also observed to change shape permanently from square shaped columns to 'domes' upon lithiation and 'bowls' upon delithiation. In addition to cracking, another important observation was the occurrence of aggregation or merging together of Si columns spaced less than 1 μm apart; which has also been speculated in other studies based on post-cycling SEM observations of Si.[17,164,167,170] With respect to the evolution of the surface of 'alloying reaction' based anode materials, *in situ* AFM studies revealed that the formation of the SEI is a continuous process in the sense that it forms, grows, breaks, and reforms.[81,171–173] In fact, Tokranov *et al.*[81] cautioned that the changes in lateral dimensions of Si-based structures, as observed with *in situ* AFM, might have some contributions from the build-up of the SEI layer. Overall, such observations may be

considered as proof for the unstable nature of the SEI that forms on 'alloying reaction' based anode materials, which can, in turn, be attributed to the colossal dimensional changes upon lithiation/delithiation.

In a pioneering study with a graphitic carbon electrode, Hirasawa *et al.*[174] had observed SEI layer formation at ~0.9 V (*vs.* Li/Li^+) during electrochemical lithiation *via in situ* AFM. The SEI layer was found to be composed of two types of layers, which agrees with other models proposed for the structure of the SEI.[80,121–123,175–178] On a different note, observations with *in situ* AFM indicated about 24 ± 7% irreversible increase in height after completion of the first CV scan of graphitic carbon, which was attributed primarily to SEI formation on the surface.[179] However, during the subsequent CV scans, ~17% change in height was observed due to Li-intercalation in graphite, which was reversible.

In situ AFM observations made during electrochemical cycling of $LiCoO_2$ (ref. 180) showed ~1.28–1.3% volume changes when x in Li_xCoO_2 changes from 1 to 0.35, which was considered to be fairly small to cause considerable mechanical degradation. This, however, does not agree with the inferences based on *in situ* stress measurements.[24]

7.3. *In situ* XRD

The *in situ* XRD technique allows fairly straightforward monitoring of the changes in the structure, phase and lattice dimensions of electrode materials taking place during electrochemical lithiation/delithiation, which in turn provides insights into the strains/stresses and possible causes of loss in integrity upon electrochemical cycling. In addition to looking into the reaction mechanisms, the structural changes and phase evolutions/transformations, micro-strain developed in electrode materials during electrochemical cycling can also be estimated using high resolution XRD. Based on Williamson–Hall analysis, the micro-strain (ε) and crystallite size (D) can be de-convoluted from the full width at half-maximum (β_{hkl}) (corrected for instrumental broadening) and diffraction angle (2θ) of a particular peak corresponding to a (hkl) plane, as per the following relations:[181,182]

$$\varepsilon = \beta_{hkl}/4 \tan \theta \quad (9)$$

$$D = K\lambda/\beta_{hkl} \cos \theta \quad (10)$$

where K is the crystallite shape factor and λ is the wavelength of the X-ray used. Lee *et al.*[181] reported on the estimations concerning the build-up of micro-strains in Li-T_M-oxide based cathode materials during electrochemical delithiation/lithiation (over multiple cycles) upon recording the diffraction patterns *ex situ*. Nevertheless, if performed based on *in situ* data, one may be able to obtain real-time and possibly additional information on the related aspects. Overall, *in situ* XRD is also much easier to perform and, in principle, electrodes of any form can be used. One just needs to ensure that the X-ray beam is incident on the concerned active material inside the sealed electrochemical cell (having a small hole, usually covered by Kapton tape or a beryllium window) and the diffracted beam is able to reach the detector. This technique has been used routinely for various electrode materials[24,54,156,183–211] and reviewing most of them here is beyond the scope of this manuscript.

In one of the pioneering studies, Reimer and Dahn[194] performed *in situ* XRD during electrochemical cycling of Li_xCoO_2 to reveal the changes in lattice parameters corresponding to the *a*- and *c*-axes, as well as the occurrence of three distinct phase transformations, during electrochemical cycling of $LiCoO_2$ (when x varies from 1 to 0.4). These inferences were invoked to explain the stress evolution during delithiation of $LiCoO_2$.[24]

In the context of upcoming greater Ni-containing layered Li-T_M-oxide based high capacity and high voltage cathode materials (such as $LiNi_{(1-x-y)}Co_xMn_yO_2$), *in situ* XRD has been

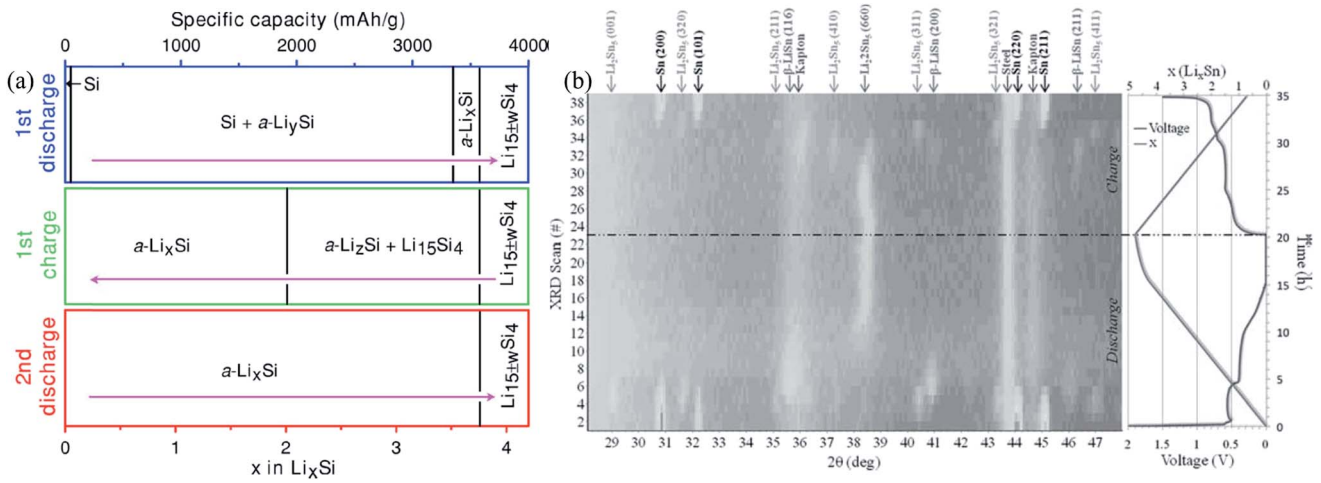

Fig. 19 (a) The phase evolutions during the 1st lithiation (discharge), 1st delithiation (charge) and 2nd lithiation (discharge) half cycles of c-Si particles, as inferred from the associated *in situ* XRD scans (reproduced with permission.[190] Copyright 2007, The Electrochemical Society). (b) Isoplot obtained from *in situ* XRD scans conducted during electrochemical lithiation and delithiation of the Sn film electrode (reproduced with permission.[156] Copyright 2012, The Electrochemical Society).

regularly used to 'observe' the rapid and anisotropic collapse of the layered structure (*i.e.*, shrinkage of the *c*-axis parameter) below a certain Li-content during electrochemical delithiation at the higher cell voltages.[201–203,205] In this context, a very recent study by Li *et al.*[201] indicated that the anisotropic shrinkage of the *c*-axis (by ~5%) takes place upon Li-extraction beyond 80% and is probably independent of the Ni content, unlike the more popular belief, which associates it with greater Ni content.[202,203,212] In another recent study, *in situ* XRD results, in combination with detailed electrochemical analysis, indicated that the presence of Co in high Ni-containing Li-T_M-oxide does not truly help in suppressing the deleterious phase transitions, structural distortions and safety aspects during electrochemical delithiation.[204] By contrast, Al, Mn and Mg, as substituents for Ni in amounts as low as even 5%, help with the above. On similar lines, Xie *et al.*[205] reported that the presence of just 2% Mg in $Li_{0.98}Mg_{0.02}Ni_{0.94}Co_{0.06}O_2$ suppressed the anisotropic lattice shrinkage, associated structural distortions and cracking of the particles at deep states of delithiation, along with raising the peak exothermic temperature by ~35 °C (*viz.*, improvement in safety aspects). It was believed that the presence of Mg^{2+} in the Li layers acts as pillars towards suppressing the contraction of the *c*-axis upon the removal of Li beyond ~60%. Additionally, this work also indicates that just the mere presence of Co does not help suppress the lattice distortions and the associated negative impacts. Looking beyond Li-ion battery systems, *in situ* XRD has also been more recently used to 'observe' and understand the occurrences/non-occurrences of the reversible/irreversible phase/structural changes during electrochemical desodiation/sodiation of Na-T_M-oxide based cathode materials,[206–211] where also Mg, Cu, Ti *etc.* have again been found to be some of the substituents that supress/delay some of the deleterious phase/structural transformations during electrochemical cycling.

In situ XRD studies during lithiation/delithiation of crystalline Si (c-Si) established that during lithiation pristine c-Si first transforms into amorphous Li_xSi (a-Li_xSi), but with further lithiation down to ~60 mV, (*vs.* Li/Li^+) a crystalline $Li_{15}Si_4$ phase (c-$Li_{15}Si_4$) is formed (see Fig. 19a), which is detrimental towards the integrity of Si-based electrodes.[188,190,191] In the case of lithiation of amorphous Si, the detrimental c-$Li_{15}Si_4$ phase forms at a slightly lower potential (*i.e.*, 30 mV *vs.* Li/Li^+).[188] Such findings help set the cut-off voltages to improve the cycle stability of Si-based electrodes.

In situ XRD measurements with Sn electrodes confirmed that lithiation/delithiation of Sn takes place *via* sequential formation of various Sn–Li intermetallic phases.[156,192] During lithiation of Sn, Rhodes *et al.*[156] found that Li_2Sn_5 is the 1st Sn–Li intermetallic phase that can be detected *via in situ* XRD, with β-LiSn and $Li_{22}Sn_5$ phases being detected upon further lithiation (see Fig. 19b). These phase transformations were found to be reversible upon delithiation. The volume changes associated with the formation of Li_xSn phases, *viz.*, Li_2Sn_5, β-LiSn and $Li_{22}Sn_5$, were estimated to be ~19%, ~50% and ~290%, respectively. In the above context, it may be recalled here that our *in situ* stress measurements have revealed the deleterious effects of such changes in volume during the phase transformations between different Sn–Li intermetallic phases.[18,19]

In the case of graphitic carbon, the formation of various lithium graphite intercalated compounds (Li-GICs) during electrochemical Li-insertion/de-insertion into/from the graphite anode was confirmed using *in situ* XRD.[187,195,196] Interestingly, when graphite was cycled either with higher current densities (*viz.*, C/3) or at higher temperatures (*viz.*, 47 °C), Li-intercalation in graphite was observed to be different from the classical Li-intercalation mechanism *via* the usual 'staging' phenomenon.[195,196] At higher temperature, several other phases were found to coexist.[196] Additionally, the change in the lattice parameter of graphite upon lithiation (*i.e.*, from graphite to LiC_6) was found to be greater (*i.e.*, ~10.605%) at 47 °C, as compared to the corresponding change at room temperature (*i.e.*, ~10.509%).

Due to the inability of graphitic carbon to intercalate Na-ions (unlike for Li-ions), 'alloying reaction' based anode materials,[213] in particular, Sb,[197] SbSn[198,199] and SbSn/graphene composites,[200] have been of interest. This, of course, has become exacerbated by the very good Na-storage capacity (~600–800 mA h g^{-1}) and safety aspects of the 'alloying reaction' based anode materials, as compared to hard carbon, where the sodiation potential is very close to that of Na plating.[213,214] However, similar to the case of Li-ion chemistry, cycle (in) stability is the major issue with 'alloying reaction' based anode materials in the Na-ion chemistry as well, due to volumetric changes and the associated loss in mechanical integrity during electrochemical sodiation/desodiation.

Nevertheless, in an interesting and informative piece of work, Darwiche *et al.*[197] reported better cycle stability for Sb upon repeated electrochemical sodiation/desodiation, as compared to lithiation/delithiation. *In situ* X-ray diffraction experiments conducted during electrochemical cycling suggested the formation of an intermediate amorphous Na_xSb phase during sodiation of crystalline Sb (followed by the formation of an interesting 'high pressure' cubic or hexagonal Na_3Sb) and nearly complete amorphization towards the end of desodiation. Based on the inputs from such measurements, it is believed here that the formation/transition/involvement of the amorphous phase perhaps leads to less build-up of internal stresses during the sodiation/desodiation cycles, as compared to those in the case of lithiation/delithiation, which proceeds *via* phase transformations in the crystalline form. This opens up another possibly interesting aspect to be investigated and better understood *via in situ* monitoring of stress development during electrochemical cycling. In another study with SbSn microparticles, Darwiche *et al.*[198] observed excellent cycle stability for at least 125 cycles at C/2 for a Na-storage capacity of 525 mA h g^{-1}. *In situ* XRD indicated amorphization also in this case during sodiation/desodiation, but preliminary evidence suggested the possible formation of Na_3Sb directly, instead of going *via* the intermediate phase. Nevertheless, *in situ* XRD, as well as *in situ* Mössbauer spectroscopy, suggested that sodiation of the SbSn alloy does not correspond to mere sodiation of Sb, with 'extraction' of Sn, as one might otherwise expect. Similar to Sb, during the discharge cycle, SbSn reacts with Na, leading to the formation of amorphous Na_xSb and Sn. Following on from that, a combination of *in situ*

XRD and *in situ* Mössbauer studies allowed obtaining improved insights into the sodiation/desodiation mechanism of SbSn electrodes.[199] It was found that Sb (of the SbSn alloy) first forms Na_3Sb upon sodiation, which is then followed by the 'extraction' of Sn, but in the form of nanocrystalline α-Sn (and not β-Sn), which is otherwise not known to be stable under ambient conditions. α-Sn gets further sodiated to form $Na_{15}Sn$, unlike what can be achieved during lithiation. In this work it was believed that the stepwise sodiation (and concomitantly gradual volume change), in addition to the amorphization (as mentioned earlier), allows better retention of mechanical integrity upon sodiation/desodiation, thus providing enhanced cycle stability, as compared to the case of lithiation. Furthermore, the structural and cycle stabilities of SbSn were found to further improve when SbSn was combined with a 3D graphene network, presumably acting as a 'buffer' material[200] (see Section 4.1). Again, all the above interesting aspects definitely encourage further studies by means of *in situ* monitoring of stress development during electrochemical lithiation and sodiation of such 'alloying reaction' based anode materials.

7.4. *In situ* Raman spectroscopy

One of the advantages of Raman spectroscopy over XRD is that unlike XRD, it can extract information from crystalline and amorphous phases. For performing *in situ* Raman spectroscopy during electrochemical cycling, the working electrode is usually coated on a mesh-type current collector, which allows optical access to the active material *via* a top quartz/glass window of the custom-designed cell. The *in situ* Raman cell design is often similar to that used for *in situ* stress measurement with the MOSS set-up (see Section 3.2) and is also sometimes a modified coin cell, but in this case optical access to the active material is also needed, which is aided by the mesh-type current collector. *In situ* Raman spectroscopy has been used to detect phase transformations, understand reaction mechanisms and also estimate strain/stress development during electrochemical cycling of various electrode materials, such as Si,[215–217] graphite/graphene,[138,218] and V_2O_5.[219,220]

While performing *in situ* Raman studies during electrochemical cycling of crystalline Si nanoparticles, Zeng *et al.*[215] and Tardif *et al.*[216] observed that with increase in the degree of

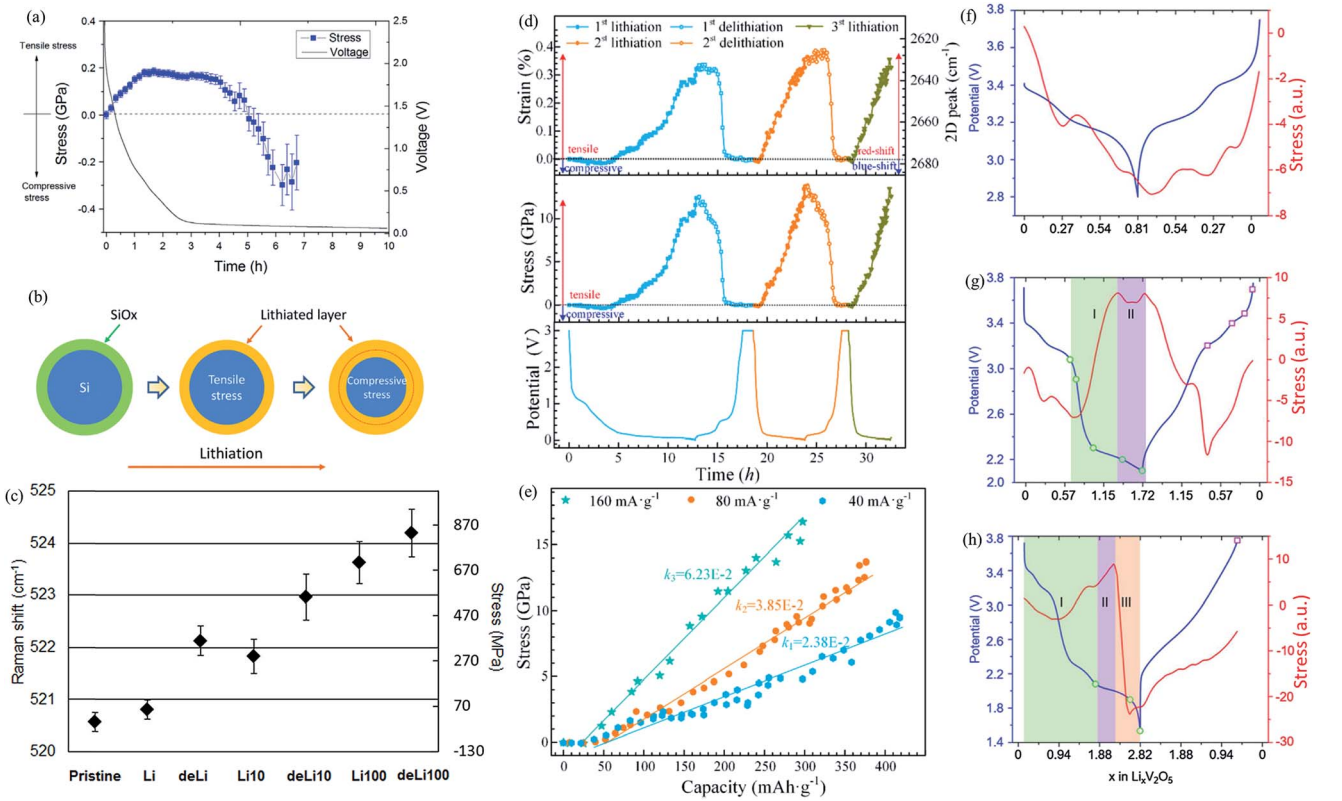

Fig. 20 A few examples of the estimation of strain/stress *via in situ* Raman spectroscopy during electrochemical cycling. (a) Stress development during the first 6.5 h of lithiation of Si nanoparticles. (b) Schematic representation of the lithiation process and stress development in Si nanoparticles having a thin native oxide layer on the surface (reproduced with permission.[215] Copyright 2016, Elsevier). (c) Variations in the Raman shift and associated stress development in Si nanoparticles at the end of the 1st, 10th and 100th lithiation and delithiation cycles (reproduced with permission.[216] Copyright 2017, American Chemical Society). (d) The variations in Raman peak shift (for 2D peak) and development of micro-strain and micro-stress during the first two full cycles and the 3rd lithiation cycle of graphene nano-platelet based electrodes. (e) Stress development during the lithiation half cycles (conducted at current densities of 160, 80 and 40 mA g^{-1}) of graphene nano-platelets (reproduced with permission.[138] Copyright 2018, Elsevier). Stress development in the V_2O_5 film electrode during lithiation/delithiation cycle with lower cut-off voltages of (f) 2.8 V (for the 1st cycle), (g) 2.1 V (for the 3rd cycle), and (h) 1.5 V (for the 5th cycle) (reproduced with permission.[219] Copyright 2017, Elsevier).

lithiation, the intensity of the signature 1st order peak at ~520 cm^{-1} of c-Si nanoparticles decreased. The associated stress development in the Si particles was estimated using the relation $\Delta\omega = -4.4\sigma$, where $\Delta\omega$ is the Raman peak shift (cm^{-1}), σ is the stress (GPa) and the (−) sign indicates the compressive nature of the stress.[215] It was observed that prior to lithiation of Si, the native oxide layer present on the surface is lithiated and the 1st order Raman peak shifts towards a lower wave number, which corresponds to a peak tensile stress of (+)0.2 GPa in the c-Si nanoparticle. Furthermore, during the actual lithiation of Si, pristine c-Si develops a core–shell structure, with the core being made of c-Si and shell being made of amorphous Li_xSi. Accordingly, the tensile stress developed earlier due to the lithiation of the native oxide layer decreased upon actual lithiation of Si. Eventually, with increase in the degree of lithiation of Si, the 1st order Raman peak was observed to shift to higher wave numbers, corresponding to a tensile-to-compressive stress transition (see Fig. 20a and b), leading to a peak compressive stress of (−)0.3 GPa after 6.5 h of lithiation. It was also hypothesized that the development of compressive stress in the c-Si core and tensile stress in the amorphous Li_xSi shell during lithiation of Si particles may induce fracturing/cracking during the lithiation step itself, unlike for the Si film electrodes which experience cracking primarily during the delithiation.[11,17,31,102] Using Raman studies, Tardif *et al.*[216] estimated a peak compressive stress development of (−)0.14 GPa during the first delithiation half cycle of Si and also found that the magnitude of compressive stress increases with continuous electrochemical cycling, eventually nearing (−)0.9 GPa after 100 lithiation/delithiation cycles (Fig. 20c). It may be pointed out here that even though the magnitude of the lithiation induced stresses estimated from *in situ* Raman data is less compared to the 'external stresses' measured *via* the substrate curvature method with continuous Si film electrodes, they are fairly close to those measured with patterned Si film electrodes[50] and slightly greater than those measured with the 'porous composite' particle-based electrodes.[14] In the later context, it may be noted that the stress estimated from Raman data is likely to be a combination of 'internal' and 'external' stresses, whereas those measured from substrate curvature is primarily 'external' in nature. In a different study with pristine and carbon coated Si nanowires (SiNWs), Krause *et al.*[217] showed that the decrease in the intensity of the 1st order Raman peak during lithiation was due to a combination of SEI layer formation on the Si surface and amorphization of bulk Si, but with the 'skin effect' from the thick SEI layer formation playing a more dominant role. Furthermore, the SEI layer formation and, accordingly, the 'skin effect', could be suppressed by a thin carbon coating on the SiNWs.

Using *in situ* Raman studies, Xie *et al.*[138] studied the kinetics of Li-storage (*i.e.*, charge/discharge rates), the strain/stress development and the associated mechanical deformations at the microscopic levels for graphene nano-platelets during lithiation/delithiation. The in-plane biaxial strain (ε) and stress (σ) developed in the graphene nano-platelets during lithiation were estimated by monitoring the shift in the 2D peak position using the relations $\varepsilon = -\Delta\omega/13500$ and $\sigma = -E\Delta\omega/13500(1-\nu)$ where $\Delta\omega$ is the Raman peak shift associated with the 2D peak, E is the elastic modulus and ν is the Poisson's ratio of graphene. Interestingly, it was found that the stress development at the microscale, as estimated based on the *in situ* Raman data, was found to be tensile during lithiation (Fig. 20d). This was very different from the observations made with the other *in situ* techniques, such as substrate curvature, DIC, XRD and also *ex situ* Raman spectroscopy,[218] where the overall nature of the stress development during lithiation of graphite/graphene was found to be compressive. Here, it may be recalled that unlike in the case of Raman, the stresses measured *via* substrate curvature are primarily 'external' in nature and usually averaged out over the entire electrode. Nevertheless, to start with, the contribution from SEI layer formation was found to be compressive in nature, *viz.*, (−)0.12 GPa, which qualitatively agreed with the observations made with *in situ* substrate curvature techniques.[20,21] However, with increasing degree of lithiation of graphene, the C–C bonds get elongated due to the formation of various Li-GICs. Accordingly, compressive strain got converted to tensile strain, which rapidly increased to a peak strain of ~0.32% by the end of the 1st lithiation half cycle, with the peak strain further increasing to ~0.354%, corresponding to a peak tensile stress of ~(+)13 GPa in the subsequent cycles. During delithiation, the strain profile appeared to be sigmoidal, remaining almost flat until the voltage went up to 0.3 V (*vs.* Li/Li^+). This was associated with the extraction of Li from graphene layers being difficult initially, causing the lithiated graphene to experience a kind of 'flow' deformation. Subsequently, due to rapid Li extraction, the built-in strain decreases at a faster pace, but again slows down towards the end of delithiation. An important observation was that the stress/strain development is fully reversible even at microscopic levels, with no evidence of residual stress/strain. It was also observed in the same work that the stress development is fairly sensitive to the applied charge/discharge rates due to the varying steepness of Li-concentration gradients from surface/edges to inside of graphene layers. In a qualitative sense, this observation is very similar to the observations made by Tavassol *et al.*[106] while monitoring the stress development in graphitic carbon electrodes using the cantilever technique (*viz.*, *via* the substrate curvature methodology). Accordingly, at three different current densities, *viz.*, 160, 80 and 40 mA g^{-1}, the stress magnitudes estimated from the *in situ* Raman data were (+)16.7, 13.7 and 9.7 GPa, respectively (Fig. 20e). Accordingly, a higher current density is expected to cause mechanical degradation of graphenic/graphitic carbon based electrodes at the microscale, which, in turn, qualitatively aggress with the inferences based on our study related to *in situ* stress measurement using the MOSS for few layer graphene based film electrodes.[23]

In situ Raman studies, coupled with *in situ* interferometry, have been used to understand the stress development and structural evolution during electrochemical cycling of V_2O_5-based cathode materials.[219,220] During lithiation, V_2O_5 was found to undergo multiple phase transformations to various $Li_xV_2O_5$ phases, *viz.*, α-, ε-, δ-, γ-, and ω-V_2O_5 at $x = 0$, 0.4, 1.0, 1.4, and 2.0, respectively. It was also observed that the structure of $Li_xV_2O_5$ remains fairly stable and reversible upon the

formation of α-, ε-, and δ-phases (*i.e.*, down to 2.8 V *vs.* Li/Li^+) (see Fig. 20f). However, the formation of γ-$Li_xV_2O_5$ (and beyond) with increasing lithiation (down to 2.1 V) causes the structure to become puckered/curled. More importantly, it was estimated that during the α- to δ-phase transformation, a tensile stress of up to ~0.2 GPa got developed due to the shrinkage of the lattice parameter along the *a*-axis (see Fig. 20g). Furthermore, similar to observations quite often made with the substrate curvature based techniques (see Sections 4 and 5),[18,24,25,55] anomalous stress fluctuations (or 'stress release') were observed during the co-existence of two $Li_xV_2O_5$ phases, with the stress fluctuations being very sensitive to the Li-concentration and applied current density, with structural degradation being more likely at the higher current densities.[220] With regard to the reversibility of stress development, it was observed that the compressive stress development during lithiation was fully reversible during delithiation upon cycling between 3.75 and 2.1 V (*i.e.*, up to γ-$Li_xV_2O_5$), whereas lithiation below 2.1 V caused the compressive stress to drop suddenly and become tensile in nature due to the formation of ω-$Li_xV_2O_5$ (see Fig. 20h). The above two examples highlight the versatility of the *in situ* Raman technique towards evaluating and understanding the strain/stress response of electrode materials during lithiation/delithiation. With respect to the more important cathode materials like $LiCoO_2$, $LiNi_x$-$Mn_yCo_{1-x-y}O_2$, and $LiNi_xAl_yCo_{1-x-y}O_2$, even though a host of useful information, including Li-transport/kinetics, has been obtained by conducting *in situ* Raman studies during electrochemical cycling,[221–223] aspects concerning the development of strain/stress as a function of states-of-charge are yet to be studied in detail.

7.5. Digital image correlation (DIC) in real-time

In the case of DIC, digital images of the electrode surface exposed through a transparent (quartz) window are captured *via* a CCD/CMOS camera in real-time during electrochemical cycling and reconstructed in 2D/3D *via* computational tools/algorithms. This aids in the evaluation and estimation of the deformations taking place during electrochemical cycling. Using such a technique, Qi and Harris[224] measured the microstructural strain developed in 'porous composite' graphite electrodes during lithiation/delithiation. The strains associated with swelling of the composite electrode and rigid body/particle motion were estimated to be ~1% and ~3–4%, respectively. Additionally, the stiffness of graphite was found to increase with the degree of lithiation to ~3 times that of pristine graphite upon complete lithiation. In another work, it was also found that the thickness of the current collector is also likely to influence the strain development during electrochemical cycling of the graphite electrode.[225] The bi-axial strain was found to be ~2 times greater for the graphite electrode on a thinner Cu substrate, as compared to that on a thicker Cu substrate due to the greater overall rigidity of the thicker substrate (Fig. 21a and b).

DIC studies with a SiO@C electrode indicated that an irreversible (residual) strain of ~0.8 gets developed during the first cycle itself, and increases with electrochemical cycles.[226] Such an observation is in sync with the irreversible increase in height detected for Si-based electrodes by *in situ* AFM studies.[167] On a similar note, ~0.13% residual strain was estimated also for the $LiMn_2O_4$-based cathode material during

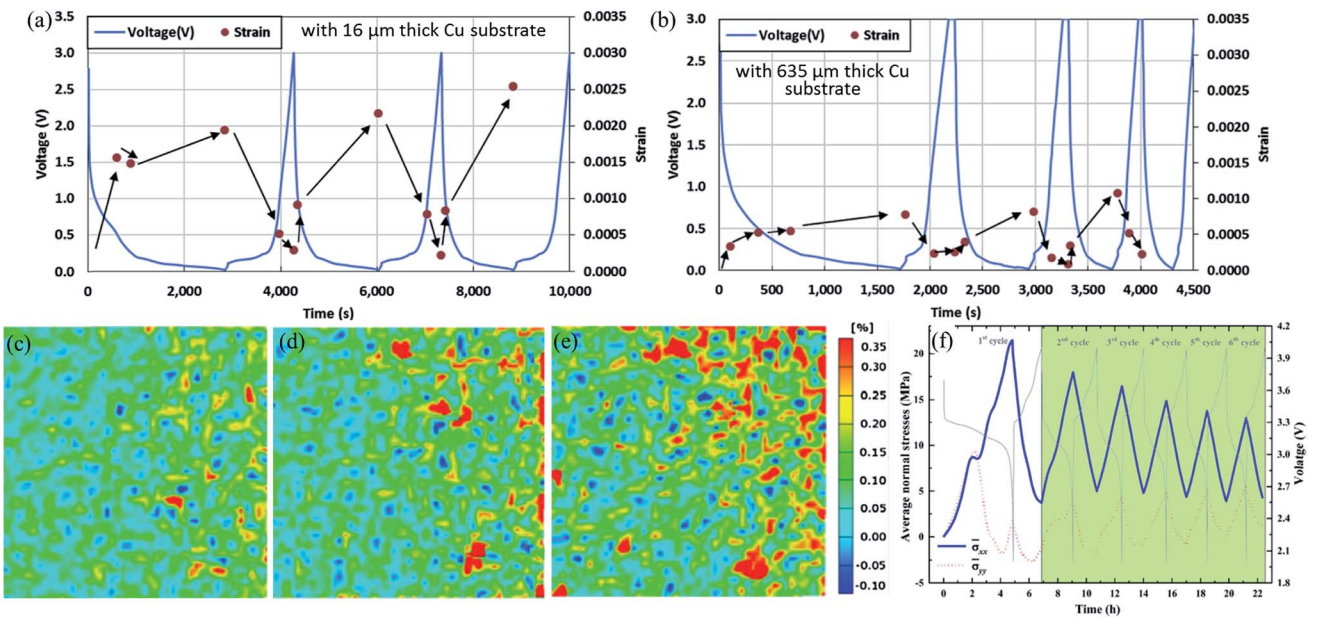

Fig. 21 A few examples of strain/stress measurements *via* the *in situ* digital image correlation (DIC) technique. Strain development during galvanostatic lithiation/delithiation cycles of the composite graphite electrode on (a) 16 μm and (b) 635 μm thick Cu current collectors (reproduced with permission.[225] Copyright 2014, Elsevier). Real-time strain maps for a Li-ion cell having a $LiCoO_2$ cathode and a graphite anode at 100% SOC for the (c) 1st cycle, (d) 25th cycle and (e) 50th cycle (reproduced with permission.[227] Copyright 2016, Elsevier). (f) Variations in the residual stress and in-plane normal stress with respect to the time during lithiation/delithiation of the V_2O_5 electrode (reproduced with permission.[228] Copyright 2018, Elsevier).

the 1st cycle, which was attributed to surface reactions and the removal of the native oxide layer from the cathode surface.[25] DIC has also been used to conduct strain measurement during prolonged electrochemical cycling of pouch-type commercial Li-ion batteries comprising a carbon based anode and $LiCoO_2$ as the cathode.[227] Such measurements showed that the principal strain at the surface of the cell increased with the number of cycles, reaching a maximum value of ~0.35% after 55 cycles (see Fig. 21c–e). Additionally, the measurement of the rate of change in overall volume indicates a maximum rate of ~4.27% at the end of 52 cycles.

Strain/stress studies *via* DIC during electrochemical cycling of V_2O_5 (ref. 228) revealed that during lithiation, heterogeneous in-plane compressive strain gets developed due to the shrinkage of lattice cell volume during δ- to γ-$Li_xV_2O_5$ phase transformation. This strain was also found to be not fully recoverable during the delithiation cycle.[228,229] The average in-plane strains in the *x*- and *y*-directions (*i.e.*, ε_{xx} and ε_{yy}) were estimated to be ~(−)1.8% and (−)2.5%, respectively. The component of the average normal stress in the *x*-direction ($\bar{\sigma}_{xx}$) increased during lithiation and decreased during delithiation, with the magnitudes being estimated to be ~21.4 and ~3.7 MPa, respectively. However, the component in the *y*-direction ($\bar{\sigma}_{yy}$) showed fluctuations (Fig. 21f). Wang *et al.*[229] also reported similar observations with 20 wt% MWCNT-containing V_2O_5, but the in-plane strains were tensile and compressive in nature during lithiation and delithiation cycles, respectively. Additionally, in the presence of MWCNT networks, the strain magnitudes were smaller as compared to the pristine V_2O_5.

7.6. *In situ* SEM and *in situ* FIB-SEM

As one of the pioneering studies, Orsini *et al.*[230] performed *in situ* SEM observations during electrochemical cycling of pouch type Li-metal batteries. With Li metal as the anode, upon prolonged cycling at a current density equivalent to ~C/5, the formation of a mossy type product (SEI) was observed, which adversely affected the Li/separator interface and caused fading. However, when the cell was cycled at 1C, Li dendrites were observed to form at the Li/separator interface, which may negatively affect the safety aspects (due to possible short circuiting[231]). Obtaining such first-hand information on the formation of a mossy-type product or sharper Li dendrites was possible due to the *in situ* SEM observations. Again, in the context of a Li-metal cell having a solid-polymer-electrolyte (SPE), Golozar *et al.*[232] observed that during the initial cycles, regions with a higher stress concentration form, leading to

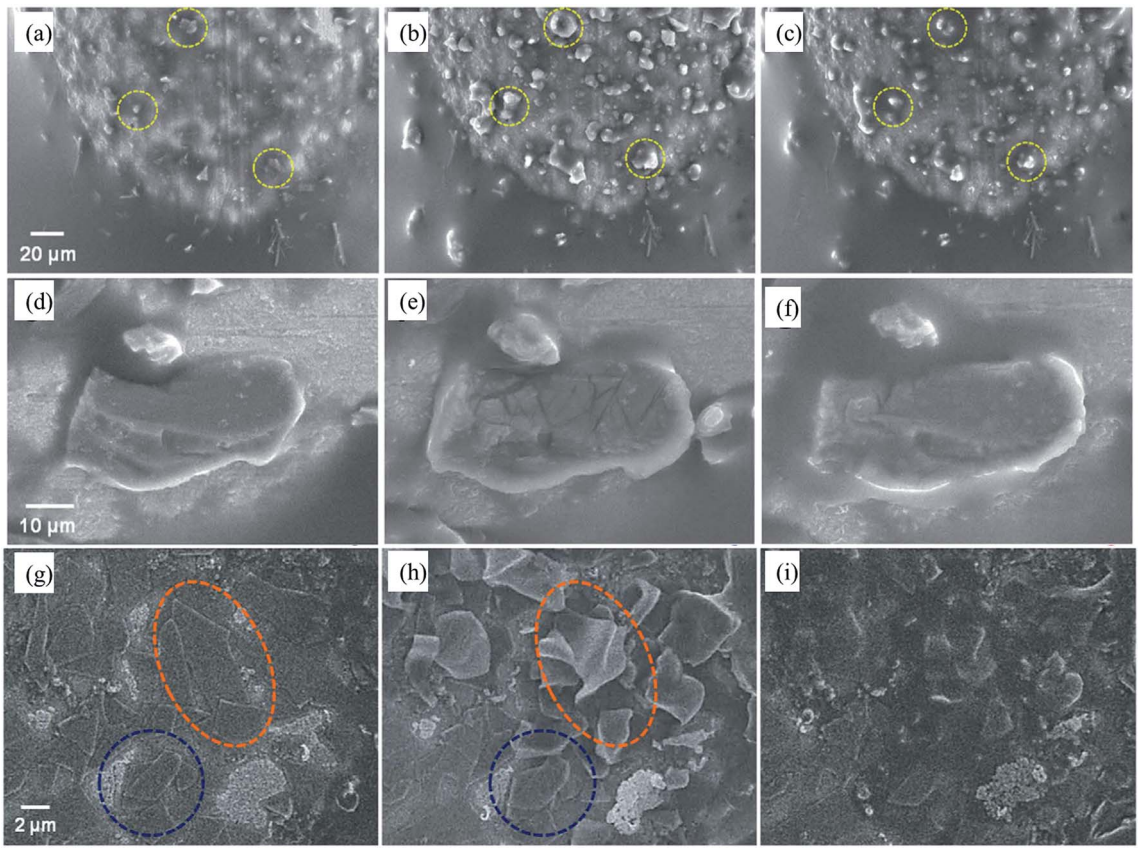

Fig. 22 *In situ* SEM observations of different Si structures at various stages of lithiation/delithiation, when cycled against $LiCoO_2$ as the cathode (reproduced with permission.[233] Copyright 2016, The Author(s), Creative Commons license). For Si micron-sized particles: (a and d) before cycling, (b and e) at the end of the 1st charge (or lithiation) half cycle and (c and f) at the end of the 1st discharge (or delithiation) half cycle. For thin Si flakes: during the 3rd cycle, (g) prior to cycling, (h) at the end of the 3rd charge half cycle, (i) at the end of the 3rd discharge half cycle. Unlike for the Si micron-sized particles (a–f), cracking is not observed during the cycling of thin Si flakes.

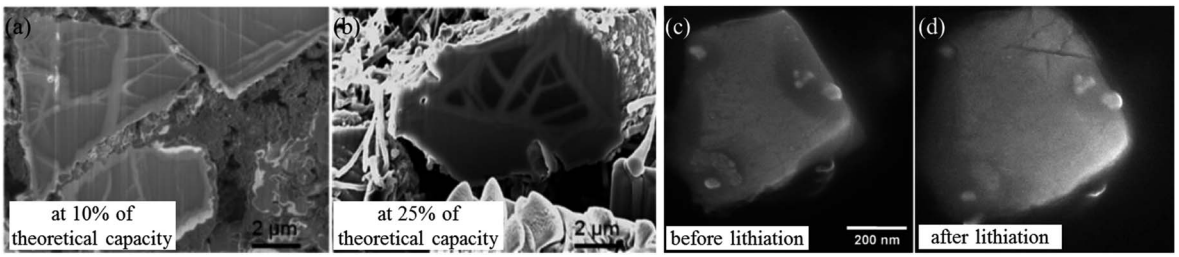

Fig. 23 SEM observations during lithiation/delithiation of Si particles *in situ* in FIB-SEM, (a) at 10% of its theoretical capacity, and (b) at 25% of its theoretical capacity (reproduced with permission.[236] Copyright 2016, American Chemical Society). SEM images of SnO_2 particles obtained *in situ* in FIB-SEM (c) before start of lithiation and (d) at the end of the 1st lithiation half cycle (reproduced with permission.[238] Copyright 2011, Elsevier).

cracking in the SPE, eventually causing Li to protrude as a needle-like structure through the cracks.

In situ SEM observations made during electrochemical cycling of Si particles indicated that the occurrence of cracking is highly dependent on the initial shape and size of Si.[233–235] While performing *in situ* SEM studies during electrochemical cycling of three types of Si nanostructures (*viz.*, micron-sized Si particles, nanoparticle agglomerates and thin flakes), Chen *et al.*[233] observed that the micron-sized Si particles got severely cracked/pulverized, with some of the particles losing electrical contact within only a few cycles (see Fig. 22a–f). By contrast, Si nanoparticle aggregates and thin Si flakes do not experience cracking during electrochemical cycling (see Fig. 22g–i). This agrees with the size-dependent stress response observed during *in situ* monitoring of stress development with a continuous and patterned Si film electrode.[50] Observations made by Hovington *et al.*[234] indicated that 'electrochemical sintering' of smaller Si nanoparticles (up to 100 nm in size) during lithiation leads to the formation of a rigid continuous network structure, which gets fractured during cycling. It was also observed that the fracturing/cracking of the Si particles can be mitigated by raising the lower cut off voltage, which is primarily to avoid the formation of the c-$Li_{15}Si_4$ phase (despite sacrificing the capacity), as discussed in Section 7.3.[188,190,191] Bordes *et al.*[236] performed *in situ* FIB studies, coupled with time of flight secondary ion mass spectrometry (TOF-SIMS), during electrochemical cycling to 'map' the lithiation mechanism in Si and the associated structural evolution during the first cycle. The *in situ* elemental mapping revealed that during the initial lithiation (*viz.*, up to a SOC of ~5%), a major portion of the incoming Li is consumed in surface reactions. With increasing SOC, the Si particles adopt a core–shell structure (*viz.*, unlithiated core and lithiated shell), as also reported in the cases of *in situ* TEM and Raman studies,[144,215] with cracking getting initiated at ~50% SOC. In the unlithiated core, a continuous network of lithiated Si is formed which acts as the Li-diffusion pathway (Fig. 23a and b).

Zhou *et al.*,[237] in their study with micron-sized Sn particles, revealed that volume change after complete lithiation is ~386%, which to some extent agrees with the theoretical predictions.[1] Additionally, cracks were observed to appear on the surface at much early stages of lithiation (*viz.*, at ~20% lithiation), which grew from the surface to core of the Sn particle with further lithiation. During contraction upon delithiation, nanopores were observed to form and grow with increasing delithiation, finally leading to severe pulverization. Nevertheless, it was also observed that the mechanical degradation of Sn can be controlled/minimized by limiting the degree of lithiation. *In situ* SEM observations during cycling of SnO_2 particles revealed that bigger SnO_2 particles are more prone to cracking and formation of Sn/Sn–Li extrusions, as compared to the smaller particles of sizes below ~100 nm (Fig. 23c and d).[238]

7.7. *In situ* X-ray absorption spectroscopy (XAS) and *in situ* Mössbauer spectroscopy

While the use of X-ray diffraction is limited to crystalline or semi-crystalline materials (*viz.*, necessitating long-range ordering), techniques like X-ray absorption spectroscopy (XAS) enable obtaining valuable information even from the local environment of atoms of choice present in electrode materials, irrespective of them being crystalline or amorphous. XAS uses X-ray radiation (of energy between 3 and 35 keV) to measure the absorption edge of a particular element. In terms of sensitivity, XAS is capable of obtaining information from very short range ordering (of even ~4–5 Å). In XAS, specific absorbed energies (known as 'absorption edges'), which are similar to the characteristic binding energies of specific elements, get probed. The technique can be further sub-divided into X-ray absorption near edge spectroscopy (XANES; before and after the edge region) and extended X-ray absorption fine structure (EXAFS; the post edge region). While XANES provides information on the electronic transition and oxidation state of the concerned element, EXAFS allows obtaining information concerning the local structure around an atom, with respect to the coordination number, bond-length and bond distortions. In a classic review paper, McBreen *et al.*[239] discussed in more detail about conducting *in situ* XAS, applicability of the same towards electrochemical energy storage, and the associated advantages and limitations. The cell design for conducting *in situ* XAS during electrochemical cycling can be quite similar to the set-up used for *in situ* XRD, as described earlier (in Section 7.3), *viz.*, usually a coin cell having a suitably placed hole covered with either Kapton tape or a beryllium window.

By observing the changes (shifts) of transition metal (T_M) K- or L-edges in real-time, *in situ* XAS has been regularly used for probing the changes in oxidation states of T_Ms in Li-T_M-oxide

and also Na-T_M-oxide based cathode materials during charge and discharge in Li- or Na- 'half cells'.[240,241,243,244] The same has also been used for confirmation of non-participation of Mn^{4+} during charge and partial reduction of the same during discharge.[71,243,244] *In situ* XAS also allows probing the oxidation states and structures with depth from the surface of the electrode particles upon using the T_M L-edges and either the Auger electron yield (AEY; for a depth of up to ~2 nm), total electron yield (TEY; for depths between ~2 and 5 nm) or fluorescence yield (FY; for depths up to ~50 nm).[245] Looking beyond the oxidation states of T_Ms, *in situ* (or *ex situ*) XAS has been one of the more important characterization techniques that has allowed obtaining confirmation and insights into the occurrence/non-occurrence of oxygen-ion redox (*i.e.*, anionic redox or oxidation of O^{2-}) and the associated structural changes to allow for enhanced Li-extraction (or Na-extraction), typically towards the end of the charge cycle for many (Li-rich) Li-T_M-oxides and also T_M-deficit Na-T_M-oxides.[72,73,242,246,247] Such information and understanding are usually obtained by correlating the changes (shifts and intensity variations) in the O K-edge with those for T_M K-/L-edges and also the local structure around T_Ms (including lengths/distortion of T_M–T_M bonds, as obtained from EXAFS). Here, it is intriguing that the present literature base is presently devoid of any systematic study performed to correlate the aforementioned local structural changes with the stress development (monitored in real-time).

Mössbauer spectroscopy is a technique based on nuclear γ-resonance and usually contains four specific features, *viz.*, isomeric shift and quadrupole splitting (related to the oxidation state and coordination state), line width (related to particle size and crystallinity) and absorber (related to spin and bond strength).[248] This technique is very sensitive towards the local electronic structure and magnetic environment of an atom present in a compound and is, thus, finding increasing usage for probing the structure and electronic state of battery cathode materials at different states-of-charges (often in combination with XAS).

For example, *in situ* Mössbauer spectroscopy has allowed probing the reversible changes in oxidation states of Fe in Li_x-$Ni_{1-y}Fe_yO_2$ (ref. 249) and $Li(Fe_{1-x}Mn_x)SO_4F$[250] based cathode materials for Li-ion batteries during charge and discharge. In fact, the *in situ* Mössbauer studies for $Li(Fe_{0.8}Mn_{0.2})SO_4F$ showed complete reversibility of $Fe^{2+} \leftrightarrow Fe^{3+}$ during the charge and discharge cycles, with just ~0.6% volume change between the lithiated and delithiated triplite phases, in contrast to ~10.4% volume change between the tavorite phases (*i.e.*, $LiFeSO_4F \leftrightarrow FeSO_4F$). This indicates the superior stability of the former. Mössbauer spectroscopy has also been used for obtaining (complementary) insights into the occurrence/non-occurrence of oxygen release, as for Li-rich Li–Fe–Te–O based cathode materials,[253] where the oxidation state of Fe was found to remain unchanged during charge. However, quadrupole splitting suggested that ~24% of the Fe atoms were in a distorted local environment towards the end of the charge cycle, with the distortion happening primarily close to the surface of the particles due to oxygen release. With respect to the anode materials, Mössbauer spectroscopy has been used to detect the phase transformations and structural changes during electrochemical lithiation/delithiation, sodiation/desodiation and now potassiation/depotassiation of Sn-based electrodes (such as Sn, SnSb, Sn_2Fe, SnO_2 *etc.*).[198,199,254–258]

7.8. *In situ* dilatometry and nanoindentation

While *in situ* dilatometry can aid in observing changes in the dimensions of electrode materials in real-time during electrochemical cycling, *in situ* nanoindentation helps evaluate the changes in mechanical properties. For example, *in situ* dilatometry studies performed with Si and Si/metal multilayer films (metal = Ti, Al, and Zn) revealed that the volume expansion at a given SOC is less for the multi-layered films, as compared to Si.[259] The expansions at the end of lithiation for Si, Si/Ti, Si/Zn and Si/Al films were measured to be ~140%, ~3%, ~4.5% and ~16%, respectively. *In operando* nanoindentation measurements with the Si film electrode (performed inside an Ar filled glove-box) indicated that the elastic modulus and hardness decreased by ~52% and ~78% during lithiation.[260] The above, in turn, agrees with the theoretical predictions concerning elastic softening of Si upon lithiation.

8. Inferences possible beyond stress development and integrity of electrodes

In addition to providing insights into the mechanical properties/behavior and loss in integrity of electrode materials as functions of composition, cell voltage, state-of-charge and number of cycles during electrochemical lithiation/delithiation, the data obtained from *in situ* monitoring of stress development can be carefully analyzed for obtaining quite a few other information pertaining to the lithiation/delithiation process. One of the important features of electrochemical cycling is the gap or hysteresis between the discharge and charge potential profiles (*viz.*, lithiation and delithiation here), where the discharge potential is below the 'equilibrium' potential and the charge potential is above the same. As per the more conventional understanding of electrochemical processes, such a hysteresis is caused due to a combination of electrochemical overpotential associated with the concerned overall electrochemical reaction(s) (including charge transfer at the electrode/electrolyte interface and other associated processes) and resistance losses (*i.e.*, 'IR effect') for sustaining a given current density. However, when there is an associated stress, the elastic strain energy stored in the electrode material is also likely to influence the hysteresis loss (*i.e.*, further lower/raise the discharge/charge curves)[30,57,58] (see Fig. 1b).

In fact, the presence of stress is expected to alter the very chemical potential (μ_i) of the concerned electro-active species (i), as per the following relation:[58,59]

$$\mu_i = \mu_i^0 + RT \ln[\gamma_i N_i / \sum N_i] + z_i F\phi + V\sigma_{jj}(\delta\varepsilon_{jj}/\delta N_j)_{T,P} \quad (11)$$

where μ_i^0 is the reference chemical potential of i, R is the universal gas constant, T is the temperature under

consideration (in absolute scale), γ_i is the activity co-efficient of i, N_i is the number of moles of i, z_i is the charge of i, F is Faraday's constant, ϕ is the electrical potential, V is the total volume of the electrode material under consideration, and σ_{jj} and ε_{jj} are the elastic stress and strain tensors. It is to be noted here that the last term on the right hand side of eqn (11), *viz.*, $V\sigma_{jj}(\delta\varepsilon_{jj}/\delta N_i)_{T,P}$, accounts for the elastic strain energy present in the material under stress. Incorporation of this last term into the Nernst equation can allow for estimation of the influence of stress on the open-circuit electrode potential ($\Delta\phi_0$ or OCV, *viz.*, at 0 current). This can then be modified to suit a film electrode containing a uniformly distributed electroactive species (i) having partial molar volume of V_i (say, ~9 cm^3 mol^{-1}, as for Li in Si), as per the following relation proposed by Soni *et al.*;[58]

$$\Delta\phi_0 \approx -(RT/F)\ln[\gamma_i x/(1+x)] + (2F/3)V_i\langle\sigma_{jj}\rangle \quad (12)$$

where x is the content of electroactive species (i) in the electrode (as in the composition of Li_xSi for lithiated Si) and $\langle\sigma_{jj}\rangle$ is the equi-biaxial in-plane stress in the film electrode. It may be noted here again that the last term of eqn (12) predicts the influence of stress on the open circuit potential. A similar formulation by Sethuraman *et al.*,[30] starting with the Larché and Cahn chemical potential for solid solution,[59,60] had also led to a similar relation for the effect of bi-axial stress in the Si film electrode (upon lithiation) on the electrochemical potential, as in the following:

$$\Delta\phi_0 = (\nu_{Si}\eta\Delta\sigma_{jj})/(3F) \quad (13)$$

where η is the rate of change of volumetric strain of Si due to lithiation (~0.7) and ν_{Si} is the molar volume of silicon (~12.7 cm^3 mol^{-1}). In light of the bi-axial stresses (within the elastic regime) measured in Si film electrodes *in situ* during lithiation/delithiation using the substrate curvature methodology (*viz.*, between 1 and 2 GPa; see Section 4), the above formulations predict a change in the OCV, just due to the influence of the stresses by ~60–120 mV, *i.e.*, a 'stress–potential coupling' by ~62 mV GPa^{-1}.[30] In fact, a systematic set of experimental studies conducted by carefully varying the stress while, at the same time, monitoring the potential at different states-of-charge during electrochemical delithiation of Li_xSi also indicated a fairly similar 'stress–potential coupling' of 100–125 mV GPa^{-1}. Here it may be noted that even though the above studies have been done with Si as the electrode material, the generic formulations and methodologies (based on substrate curvature and associated *in situ* stress measurements) can be used for predicting and observing the influence of electrode stress on the electrochemical potential during lithiation/delithiation of other materials as well (including cathode materials, some of which may have more locked-in elastic stresses, but lower V_i). Such information, having roots at basic thermodynamic principles, will provide valuable information concerning the expected cell voltages and energy efficiencies of different cell chemistries involving insertion-based electrodes.

Another formulation, again invoking basic thermodynamic principles, suggests that stress development may have influence on the ease of lithiation, which will then influence the overall Li-storage capacity obtained with a particular electrode at a given current density. In this regard, an expression for the overall free energy change (ΔG) for the reaction concerning lithiation of any host (H) (*viz.*, Li + $1/x$H ⇔ $1/x$$Li_x$H) can be written as[17,61]

$$\Delta G = \Delta G_i - e\phi + \Delta G_{stress} \quad (14)$$

where ΔG_i is the chemical free energy change for lithiation of H, the term $e\phi$ is associated with the effects of electrical potential (ϕ) (e being the charge on one electron for insertion of one Li^+) and, again, the rightmost term ΔG_{stress} denotes the contributions from work done by stress towards the ΔG. At any stage of lithiation, when the un-lithiated host (H) co-exists with lithiated H (*viz.*, Li_xH), ΔG_{stress} can be denoted as

$$\Delta G_{stress} = 1/x(\langle\sigma\rangle_H\Omega_H - \langle\sigma\rangle_{Li_xH}\Omega_{Li_xH}) \quad (15)$$

where $\langle\sigma\rangle$ is the bi-axial stress in either H or Li_xH and Ω is the atomic volume. A combination of the above eqn (14) and (15) indicates that the compressive stress (which has a 'negative' sign) in the lithiated region (*viz.*, $\langle\sigma\rangle_{Li_xH}\Omega_{Li_xH}$) is likely to lessen the driving force for further lithiation (*i.e.*, ΔG will be rendered less negative).

The above logic has been invoked in our work[17] to explain the lower Li-storage capacity (by about half) obtained in Si film electrodes (see Fig. 5a, b and d), which develop greater compressive stress per degree of lithiation (as per *in situ* stress measurements), as compared to similar Si film electrodes, but have a graphene-based interlayer, under identical electrochemical conditions (see Fig. 24a). This view-point is also supported by observations concerning slowing down of the deformation of Si-based composite electrode (in the form of a cantilever) with increased Li-concentration, as made by Xie *et al.*,[62] who associated this partly to the diffusion of Li getting suppressed due to the development of compressive stresses (see Fig. 24b). With regard to amorphous Ge (a-Ge) based film electrodes, *in situ* stress measurements during potentiostatic and galvanostatic intermittent titrations (*viz.*, PITT and GITT) indicated that the Li-diffusion coefficient increases with increasing Li-concentration.[63] More importantly, in support of the above discussion, the Li-diffusion coefficient was found to be strongly influenced by the nature of the stress developed (*i.e.*, compressive or tensile) in a-Ge film, with tensile stress (during delithiation) promoting Li-diffusion and *vice versa*. Similar observations concerning compressive stress retarding lithiation and *vice versa* were also noted for Ge nanowires *via in situ* TEM observations, coupled with chemo-mechanical modelling.[64] However, *ab initio* molecular dynamics calculations by Pan *et al.*[65] indicated that in the case of lithiation of Si, Li-diffusivity can be enhanced in the presence of both tensile stress (*via* enhanced free volume) and compressive stress (*via* changes in the local structure). However, even with respect to the Li-diffusivity values estimated in that work, for a given level/magnitude of hydrostatic stress, the diffusivity was found to be greater in the case of tensile stress by factor of ~2, as compared to that in the case of compressive stress. With respect to the possible impact of stress on the

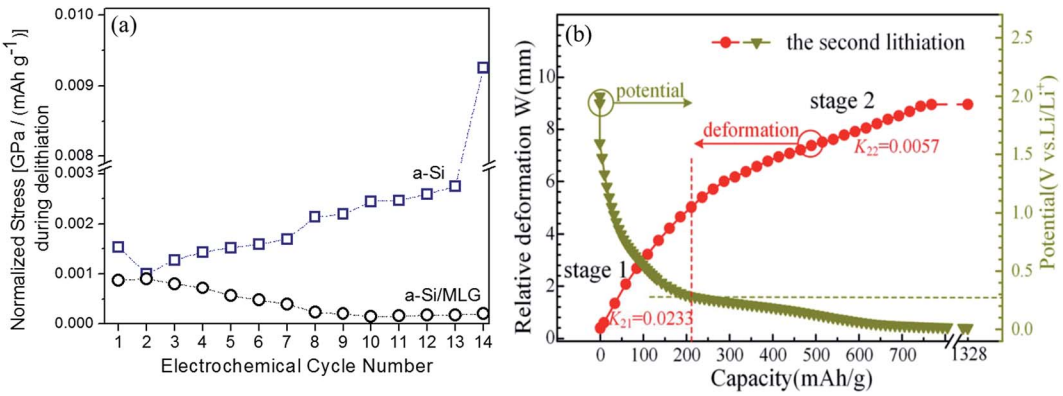

Fig. 24 Variations, with the electrochemical cycle number, of the in-plane nominal stress developed upon electrochemical lithiation/delithiation of a-Si film electrodes, in the absence and presence of the MLG interlayer, as normalized by the respective Li-storage capacity (reproduced with permission.[17] Copyright 2016, Elsevier). (b) Variations of relative deformation and potential with respect to capacity (*i.e.*, Li-content) during the 2nd lithiation half cycle of the Si-based composite electrode (reproduced with permission.[62] Copyright 2016, The Electrochemical Society).

composition of an insertion electrode, considering that, as per eqn (12), the presence of stress (*i.e.*, $\langle\sigma_{jj}\rangle$) is likely to alter the composition (*i.e.*, x) at a given potential (*i.e.*, ϕ), Soni *et al.*[58] estimated the same based on the flow stress obtained during *in situ* measurements of stress development in the Si film electrode during lithiation. Interestingly, it was found that the Li-content was indeed lower in the presence of compressive stress, but with stress having a fairly modest impact on the Li-content for this system. Such a modest influence of stress was explained on the basis of the fairly large enthalpy (and hence, free energy) of mixing of Li in Si.

From a more generic perspective, it may be noted that the voltage/current profiles recorded during electrochemical lithiation/delithiation are manifestations of various interlinked phenomena, such as equilibrium potential, electrochemical overpotential, effects of concentration of the electroactive species at the electrode/electrolyte interface, resistance effects, surface/bulk features of the electrode materials and also stress development in the electrode (see above). Hence, very reliable and specific information on some of the aspects, such as the Li-content in the electrode at a given instant, may be challenging to obtain just from the electrochemical data. By contrast, the stress profiles are primarily dependent on the Li-content of the electrode, especially in the cases where bi-axial stresses in film electrodes are measured *in situ* using substrate curvature, albeit only when the deformation is elastic in nature. Accordingly, *in situ* stress profiles simplify the process of obtaining information on the above aspect(s), as has been partly utilized in some of the aforementioned studies related to information on materials properties and composition as a function of the Li-content and electrochemical potential.[6,58,66,67]

In addition to the above analyses, due to the dependence of the stress state primarily on the Li-content (within the elastic regime), *in situ* stress measurements can be used for determination of various kinetic aspects associated with electrochemical lithiation/delithiation. For example, stress measurements during potentiostatic lithiation of Sn film electrodes allowed Chen *et al.*[68] to estimate the Li-diffusivity in the first Sn–Li intermetallic phase (*i.e.*, Li_2Sn_5), which was found to be of the order of 10^{-12} cm^2 s^{-1}. Furthermore, in the same work, another very important kinetic parameter, *viz.*, the 'reaction rate co-efficient', which relates the velocity of the phase transformation front to the local supersaturation of the reacting species (Li, here) at the interface between the parent and new phases, could be estimated from the stress response, which was found to be of the order of 10^{-6} cm^4 mol^{-1} s^{-1} for Sn $\rightarrow$ Li_2Sn_5 transformation.

In the above contexts, it may be mentioned here that monitoring of the changes in stress states of electrode materials can also be used to analyse the kinetic aspects of spontaneous delithiation or desodiation (*i.e.*, self-discharge/relaxation) of some electrode materials believed to undergo such changes (such as $Na_4Ti_3O_7$ or $Na_2Ti_3O_7$ in the Na-ion battery system[69,193]). It may be noted that despite such aspects having lot of significance in the context of electrochemical performance and cycle stability, they are very challenging to study *via* conventional electrochemical means. Furthermore, the *in situ* stress measurements can also be used for thoroughly studying the aspects concerning oxygen evolution and creation of oxygen vacancies within the lattice of the Li-T_M-oxide (T_M: transition metal) based cathode materials (such as $LiNi_xMn_yCo_{1-x-y}O_2$ and Li–Mn-excess Li-T_M-oxides[70–74]) upon charging to higher cell voltages (*i.e.*, beyond ~4.4 V *vs.* Li/Li^+). Even though such studies were initiated by Nation *et al.*,[26] more systematic sets of studies are needed to arrive at a comprehensive understanding of the associated stress response and the exact role(s) of the creation of lattice vacancies towards the same. In this context, it needs to be mentioned that earlier Mandowara and Sheldon[75] had demonstrated the possibility of using such a substrate curvature methodology for monitoring the stress development due to oxygen release from CeO_2 films *in situ* during exposure to high temperature and associating the same to the creation of oxygen vacancies in the lattice.

9. Summary and outlook

9.1. Summary

The occurrences of dimensional/structural changes, phase transformations and irreversible surface phenomena during electrochemical lithiation/delithiation of electrode materials for Li-ion batteries lead to stress development in the electrodes. Such stresses have pronounced influences, not only on the integrity of the electrodes upon repeated lithiation/delithiation, but also on various aspects related to the electrochemical behavior (including voltage hysteresis). Accordingly, they play significant roles towards determining (often, limiting) the cycle life and other electrochemical performances of electrodes, and, in turn, of the electrochemical cells, as a whole. This has been one of the major bottlenecks towards the successful development of Li-ion cells possessing considerably improved energy density, power density and safety aspects. In order to evaluate and better understand such electro-chemo-mechanical responses of electrode materials, numerous studies have focused on *in situ* monitoring of stress development in electrodes during electrochemical cycling; more commonly using different manifestations of the substrate curvature methodology.

Such measurements have been instrumental towards finding the absolute values of the stresses, the stress evolution patterns and the mechanical behavior/integrity (including occurrence/non-occurrence of plastic flow, cracking *etc.*) at various states-of-charges and different electrochemical cycles.[6,7,11–13,17,18,20,22–27,30,31,50,55,56,61,87,102,103,261] They have also served as the basis for evaluating and understanding the effects of presence of different components of the electrodes, including binders[27] and 'buffer' interlayers (such as graphene)[17] on the stress development and integrity of the electrode upon repeated electrochemical lithiation/delithiation. In addition to stress and integrity related aspects, such measurements have also provided complementary and valuable information concerning the electro-chemical phenomena (including chemical potential, voltage hysteresis *etc.*), associated mass transport processes and the structural/phase changes that take place in the electrode materials during the course of lithiation/delithiation.[6,17,26,30,57–75] In fact, understanding of the effects of 1st order phase transformations in the electrode materials on the overall stress development, integrity and electrochemical performance of the electrode could only be possible due to the ability to monitor the stress development in real-time during lithiation/delithiation.[18,19,24–26,55]

Such *in situ* experiments have also served as an indirect means towards studying the impacts of the formation of passivation layer (*i.e.*, solid electrolyte interface; SEI) on the surface of electrodes, usually during the first few cycles.[20–23,54,80] Here it may be recalled that at any stage (or instant), the net stress measured by the substrate curvature methodology is the overall (average) in-plane stress developed in the electrode. This may, in turn, have contributions from the actual reversible process of charge storage within the bulk/surface, the associated structural changes and irreversible surface phenomena (including the formation of the SEI layer). In this context, as demonstrated by the aforementioned studies that report on the stress associated with the formation of SEI layer,[20–23,54,80] the respective contributions from the actual reversible intercalation/deintercalation phenomena and irreversible 'surface' processes towards the overall stress development can be de-convoluted *via* systematic and clever designing of experiments, combined with careful analysis of the as-recorded stress data.

On another note, the *in situ* stress measurements have been duly complemented by other *in situ* characterization studies, such as *in situ* X-ray diffraction (including synchrotron diffraction),[54,156,183–196] Raman spectroscopy,[138,215–223] TEM,[96,142–162] dilatometry[259] *etc.* A combination of the inferences obtained from all such *in situ* studies has led to fairly comprehensive understandings of the various compositional/structural/dimensional changes, stress development, associated integrity and electrochemical performances of electrode materials upon repeated electrochemical cycling. A comprehensive summary of all the *in situ* techniques discussed in this review article, the main observations/inferences that can be made upon their usage and some of the electrode materials that have been subjected to such investigations (along with the corresponding references) have been presented in Table 3. Upon further expansion of *in situ* capabilities with more 'modern day' and more advanced facilities, like *via* the usage of synchrotron XRD,[54,193] high pressure TEM *etc.*, additional information and concomitant understanding can be obtained, which has so far eluded the research community.

9.2. Outlook and perspectives

A closer look into the literature base still indicates considerable differences in the results and interpretations across different studies, even when investigating the evolution of stresses in a particular type of electrode material. The reasons for the same may be summarized, as in the following. First, the types of stresses measured with the different techniques are often not the same. For example, while substrate curvature based techniques directly measure the average overall in-plane stresses, X-ray diffraction and Raman spectroscopy can be used to measure the local (or micro-) strains/stresses. Second, the set-ups and area/volume of the electrode probed are different for different techniques. Third, the type (*viz.*, film *vs.* 'porous composite') and dimension/thickness of the electrode under consideration often vary, even when the same technique is used. These influence the development of stresses during electrochemical cycling of even the same material-type. Finally, some of the studies have been seen to better de-convolute the stresses that arise due to irreversible surface phenomena (refer to Section 6) and reversible charge storage in the bulk, and also take care of the aspects concerning deformation in the elastic or plastic regime and other changes in the associated physical/mechanical properties of the electrodes (such as stiffness), as compared to the other studies (which seem to neglect some of the above aspects), thus also contributing to the variations of the stresses that are measured.

Nevertheless, it is the inferences concerning mechanistic aspects associated with the electrode deformation and stress (as

Table 3 A summary of the various methodologies and techniques used for *in situ* monitoring of stress development and associated dimensional/structural/phase changes in electrode materials (as a function of Li-content/states-of-charge) during electrochemical cycling has been presented. The main observations and/or inferences that may be obtained and some of the electrode materials looked into with the use of the respective techniques have also been summarized

Type of *in situ* methodology/technique		Main observation(s)/inference(s) (in real-time during the occurrence of electrochemical lithiation/delithiation)	Some electrode materials looked into and the associated references
Substrate curvature	Cantilever method	Observations concerning in-plane stress development in film and 'porous composite' electrodes, primarily due to the constraining effect of the substrate (or the current collector) and other electrode components	'Porous composite' electrodes of Si,[62,104,110,266] SiO_2,[115,117] Sn,[119,120] SnO_x,[120] graphitic carbon,[105,106,124] Ge,[112] and Li-T_M-oxide (T_M = transition metal)[27]
		Inferences on the effects of internal stress development due to the occurrences of phase transformations, structural changes, changes in materials properties (such as stiffness) and Li-concentration gradients in 'active' electrode materials	Film electrode of Si[111,112,127]
	Multi-beam optical stress sensor (MOSS)	Inferences on loss in mechanical integrity (such as cracking and plastic deformation) and enhancement of voltage hysteresis	'Porous composite' electrodes of Si,[14,32] graphitic carbon,[5] and Li-T_M-oxide[27] Film electrodes of Si,[6,7,11–13,30,31,49,50,58,65,66,101,102,108,109,264,265] SiO_x (ref. 116) Si/graphene,[17] Sn,[18,19,56,68] Sn/Sn–Cu intermetallic,[56] Al,[55] Ge,[63,67,76,125,126] graphitic/graphenic carbon,[20–23,53,249,267] and Li-T_M-oxide[24–26]
Transmission electron microscopy (TEM)		Observations of dimensional, structural, and phase changes and cracking of 'active' electrode materials	Si,[142–146,268,269] Sn,[149] SnO_2,[96,147] Al,[150] Ge,[151,158] TiO_2,[152,153] Li-T_M-oxide,[159,160] and Li-T_M-phosphate[161,162]
Atomic force microscopy (AFM)		Observations of dimensional changes of 'active' electrode materials/structures	Si,[80,81,165,167,171,172] Si/Sn,[164,165] Sn,[166,173,274] graphitic/graphenic carbon,[174,179,272–275] and Li-T_M-oxide[180,274,276]
X-ray diffraction (XRD)		Inferences concerning the occurrences of phase and structural changes in 'active' electrode materials, as well as changes in lattice parameters	Graphite,[187,195,196] Si,[188,190,191,216] Sn,[156,192] Sb (and SnSb),[197–200] Ge,[185] SnO_x,[189] MnO_2,[288] Li-T_M-oxide,[194] high Ni-containing Li-T_M-oxide,[201–205] and Li-T_M-phosphate[287]
Raman spectroscopy		Inferences on strain and/or stress development in 'active' electrode materials, including kinetics of Li-storage	Graphite,[218,289] graphene,[138] Si,[216,217] Sb,[262,278] Li-T_M-oxide,[221] and V_2O_5 [219–220,279]
Digital image correlation (DIC)		Mapping and estimation of strain of 'active' electrode materials and electrodes	Graphite,[224,225] Si-oxide,[226] V_2O_5,[228,229] and Li-T_M-oxide[227,277]
Scanning electron microscopy (SEM) and focussed-ion beam (FIB)		Observations of dimensional changes and cracking	Li,[232,280] Si,[233–236,284] Ge,[285] C,[230,281] SnO_2,[237] V_2O_5,[219,220,286] Li-T_M-oxide,[230,282–284] and Li-T_M-phosphate[232]
X-ray absorption spectroscopy and Mössbauer spectroscopy		Inferences on electronic states and local structures associated with specific atoms	Sn-based,[254–257] Li-T_M-oxide,[240–245,249,253] Li-T_M-sulphate,[250] Li-T_M-phosphate,[251,252] and Na-T_M-oxide[246]
Dilatometry		Observations of dimensional changes of electrode materials and electrodes	Si,[259] Si/M multilayer (M = Ti, Al, or Zn),[259] and graphite[78]
Nanoindentation		Estimation of changes in the mechanical properties of electrode materials and electrodes	Si[260]

obtained in real-time with the techniques described here), which are of greater importance, rather than the absolute magnitude of the stresses. For example, it is only upon usage of the substrate curvature methodology for *in situ* monitoring of stress development in electrodes during electrochemical lithiation/delithiation that the phenomena concerning occurrence/non-occurrence of plastic (or viscous) deformation of electrode materials (such as Si, Sn, Al *etc.*) at certain stages of lithiation/delithiation, the effects of characteristic dimensions towards the same, effects of phase transformations on the electrode deformation/integrity, changes in mechanical properties of the electrodes as functions of Li-content (or state-of-charge), effects of buffer interlayers on the stress developmental patterns, stress development due to irreversible surface processes (such as, SEI layer formation), and so on, could be detected (identified) and studied. Such phenomena and associated knowledge are inherent to the electrode material(s) and electrochemical condition(s) under consideration, and thus, in

principle, are applicable to any electrode architecture. It is the knowledge of these aspects that are presently contributing towards better selection of the form/type/dimension of the electrode material and electrochemical conditions for achieving improved electrochemical performance.

However, some of the aspects, such as stress development during delithiation of Si film electrodes (compare ref. 7, 11–13 and 30 with ref. 17 and 104), the very nature of the stress development associated with SEI formation (compare ref. 18–21 and 23 and ref. 68 and 124), effects of stress on the Li-transport (compare ref. 17, 61 and 62 with ref. 58, 63 and 65) and the causes for observations concerning 'flattening' of stress response and 'stress release' in the case of the transition metal oxide based cathode materials (compare ref. 24–27) are yet to be fully understood and the associated debates settled. In fact, the differences in the stress responses recorded with simple film electrodes and 'porous composite' electrodes (*viz.*, those having binders and conducting additives) are yet to be properly understood.

On a different note, some of the very important aspects, such as effects of creation of oxygen vacancies (and surface structural reorganization) on the stress development in the case of the Li-T_M-oxide based cathode materials, the associated chemo-mechanical response, self-discharge and micro-cracking of electrodes,[26,70–74,181] have not yet received the extent of focus, in terms of conducting systematic sets of experiments related to *in situ* stress measurement, that is needed. Furthermore, it has been 'observed' that the presence of suitable substituents (like Mg, Cu, or Ti) suppresses the deleterious shrinkage of the *c*-axis parameter (*i.e.*, collapse of the layered structure) for high Ni-containing Li-T_M-oxides at deep states of delithiation[201–205] and the deleterious phase/structural transformations during electrochemical desodiation/sodiation of Na-T_M-oxides.[206–211] These aspects and the associated beneficial effects concerning suppression of cracking and improved cyclic stability necessitate further understanding by conducting *in situ* monitoring of the stress development during electrochemical cycling of the concerned electrodes. On similar lines, even though *in situ* XRD studies have revealed different pathways for lithiation/delithiation and sodiation/desodiation of some of the 'alloying reaction' based anode materials, including pathways which involve intermediate amorphization and thus potentially reduce the severity of stresses (otherwise associated with solid–solid phase transformation),[268–271] systematic and thorough *in situ* monitoring of stress development directed towards understanding of such aspects have not yet been performed.

Furthermore, the influences of prior (internal) stress state or externally imposed stress on the electrochemical performance (including polarization and potential hysteresis) and cycle stability is another aspect which has not yet been subjected to thorough observation/analysis and understanding. Such an understanding may pave the way towards tuning the performance of electrodes *via* imposition of stresses (at optimized levels) prior to and during electrochemical cycling, as was demonstrated in one of our previous studies.[55] Here, it may be pointed out that many a times deterioration of the performance of electrodes is observed upon moving from a coin cell (where external stress is imposed during cell assembly/fabrication) to pouch cell configuration (which does not necessitate application of stress during cell assembly/fabrication). Nevertheless, it is expected that with increasing expertise, capabilities and understanding in this area, coupled with the development of and better exposure to complementary *in situ* techniques, more valuable insights into some of the aforementioned grey areas will be obtained in the near future.

Conflicts of interest

There are no conflicts to declare.

References

1 A. Mukhopadhyay and B. W. Sheldon, *Prog. Mater. Sci.*, 2014, **63**, 58–116.
2 M. R. Palacin and A. de Guibert, *Science*, 2016, **351**, 1253292.
3 X. Cheng and M. Pecht, *Energies*, 2017, **10**, 591.
4 V. Etacheri, R. Marom, R. Elazari, G. Salitra and D. Aurbach, *Energy Environ. Sci.*, 2011, **4**, 3243–3262.
5 V. A. Sethuraman, N. Van Winkle, D. P. Abraham, A. F. Bower and P. R. Guduru, *J. Power Sources*, 2012, **206**, 334–342.
6 V. A. Sethuraman, M. J. Chon, M. Shimshak, N. Van Winkle and P. R. Guduru, *Electrochem. Commun.*, 2010, **12**, 1614–1617.
7 S. K. Soni, B. W. Sheldon, X. Xiao and A. Tokranov, *Scr. Mater.*, 2011, **64**, 307–310.
8 U. Kasavajjula, C. Wang and A. J. Appleby, *J. Power Sources*, 2007, **163**, 1003–1039.
9 M. N. Obrovac, L. Christensen, D. B. Le and J. R. Dahn, *J. Electrochem. Soc.*, 2007, **154**, A849–A855.
10 M. N. Obrovac and L. Christensen, *Electrochem. Solid-State Lett.*, 2004, **7**, A93–A96.
11 S. P. V. Nadimpalli, V. A. Sethuraman, G. Bucci, V. Srinivasan, A. F. Bower and P. R. Guduru, *J. Electrochem. Soc.*, 2013, **160**, A1885–A1893.
12 V. A. Sethuraman, M. J. Chon, M. Shimshak, V. Srinivasan and P. R. Guduru, *J. Power Sources*, 2010, **195**, 5062–5066.
13 S. K. Soni, B. W. Sheldon, X. Xiao, A. F. Bower and M. W. Verbrugge, *J. Electrochem. Soc.*, 2012, **159**, A1520–A1527.
14 R. Kumar, J. H. Woo, X. Xiao and B. W. Sheldon, *J. Electrochem. Soc.*, 2017, **164**, A3750–A3765.
15 M. T. McDowell, S. W. Lee, W. D. Nix and Y. Cui, *Adv. Mater.*, 2013, **25**, 4966–4985.
16 M. T. McDowell, S. Xia and T. Zhu, *Extreme Mech. Lett.*, 2016, **9**, 480–494.
17 M. K. Jangid, F. J. Sonia, R. Kali, B. Ananthoju and A. Mukhopadhyay, *Carbon*, 2017, **111**, 602–616.
18 A. Mukhopadhyay, R. Kali, S. Badjate, A. Tokranov and B. W. Sheldon, *Scr. Mater.*, 2014, **92**, 47–50.
19 A. Vemulapally, R. Kali, T. K. Bhandakkar and A. Mukhopadhyay, *J. Phys. Chem. C*, 2018, **122**, 16561–16573.

20 A. Mukhopadhyay, F. Guo, A. Tokranov, X. Xiao, R. H. Hurt and B. W. Sheldon, *Adv. Funct. Mater.*, 2013, **23**, 2397–2404.
21 A. Mukhopadhyay, A. Tokranov, X. Xiao and B. W. Sheldon, *Electrochim. Acta*, 2012, **66**, 28–37.
22 A. Mukhopadhyay, A. Tokranov, K. Sena, X. Xiao and B. W. Sheldon, *Carbon*, 2011, **49**, 2742–2749.
23 F. J. Sonia, B. Ananthoju, M. K. Jangid, R. Kali, M. Aslam and A. Mukhopadhyay, *Carbon*, 2015, **88**, 206–214.
24 V. Malav, M. K. Jangid, I. Hait and A. Mukhopadhyay, *ECS Electrochem. Lett.*, 2015, **4**, A148–A150.
25 J. Sheth, N. K. Karan, D. P. Abraham, C. C. Nguyen, B. L. Lucht, B. W. Sheldon and P. R. Guduru, *J. Electrochem. Soc.*, 2016, **163**, A2524–A2530.
26 L. Nation, J. Li, C. James, Y. Qi, N. Dudney and B. W. Sheldon, *J. Power Sources*, 2017, **364**, 383–391.
27 S. P. V. Nadimpalli, V. A. Sethuraman, D. P. Abraham, A. F. Bower and P. R. Guduru, *J. Electrochem. Soc.*, 2015, **162**, A2656–A2663.
28 W. H. Woodford, Y.-M. Chiang and W. C. Carter, *J. Electrochem. Soc.*, 2010, **157**, A1052–A1059.
29 J. O. Besenhard, J. Yang and M. Winter, *J. Power Sources*, 1997, **68**, 87–90.
30 V. A. Sethuraman, V. Srinivasan, A. F. Bower and P. R. Guduru, *J. Electrochem. Soc.*, 2010, **157**, A1253–A1261.
31 M. J. Chon, V. A. Sethuraman, A. McCormick, V. Srinivasan and P. R. Guduru, *Phys. Rev. Lett.*, 2011, **107**, 045503.
32 V. A. Sethuraman, A. Nguyen, M. J. Chon, S. P. V. Nadimpalli, H. Wang, D. P. Abraham, A. F. Bower, V. B. Shenoy and P. R. Guduru, *J. Electrochem. Soc.*, 2013, **160**, A739–A746.
33 H. Wang, Y.-I. Jang, B. Huang, D. R. Sadoway and Y.-M. Chiang, *J. Electrochem. Soc.*, 1999, **146**, 473–480.
34 J. N. Reimers and J. R. Dahn, *J. Electrochem. Soc.*, 1992, **139**, 2091–2097.
35 T. Ohzuku and A. Ueda, *J. Electrochem. Soc.*, 2006, **141**, 2972–2977.
36 Y. J. Kim, J. Cho, T.-J. Kim and B. Park, *J. Electrochem. Soc.*, 2003, **150**, A1723–A1725.
37 Z. Chen and J. R. Dahn, *Electrochem. Solid-State Lett.*, 2002, **5**, A213–A216.
38 A. Yano, M. Shikano, A. Ueda, H. Sakaebe and Z. Ogumi, *J. Electrochem. Soc.*, 2017, **164**, A6116–A6122.
39 Y. Zhao, P. Stein, Y. Bai, M. Al-Siraj, Y. Yang and B.-X. Xu, *J. Power Sources*, 2019, **413**, 259–283.
40 M. K. S. Verma, S. Basu, K. S. Hariharan, S. M. Kolake, T. Song and J. Jeon, *J. Electrochem. Soc.*, 2017, **164**, A3426–A3439.
41 F. Hao, X. Gao and D. Fang, *J. Appl. Phys.*, 2012, **112**, 103507.
42 T. K. Bhandakkar and H. T. Johnson, *J. Mech. Phys. Solids*, 2012, **60**, 1103–1121.
43 S. Zhang, K. Zhao, T. Zhu and J. Li, *Prog. Mater. Sci.*, 2017, **89**, 479–521.
44 R. Xu and K. Zhao, *J. Electrochem. Energy Convers. Storage*, 2016, **13**, 030803.
45 Z. Jia and W. K. Liu, *Appl. Phys. Lett.*, 2016, **109**, 163903.
46 W. Wang and P. K. Kumta, *ACS Nano*, 2010, **4**, 2233–2241.
47 R. Krishnan, T.-M. Lu and N. Koratkar, *Nano Lett.*, 2011, **11**, 377–384.
48 E. Chason and B. W. Sheldon, *Surf. Eng.*, 2003, **19**, 387–391.
49 H. Haftbaradaran, S. K. Soni, B. W. Sheldon, X. Xiao and H. Gao, *J. Appl. Mech.*, 2012, **79**, 031018.
50 S. K. Soni, B. W. Sheldon, X. Xiao, M. W. Verbrugge, D. Ahn, H. Haftbaradaran and H. Gao, *J. Electrochem. Soc.*, 2012, **159**, A38–A43.
51 S. P. V. Nadimpalli, V. A. Sethuraman, S. Dalavi, B. Lucht, M. J. Chon, V. B. Shenoy and P. R. Guduru, *J. Power Sources*, 2012, **215**, 145–151.
52 X. Su, K. Guo, T. Ma, P. A. Tamirisa, H. Ye, H. Gao and B. W. Sheldon, *ACS Energy Lett.*, 2017, **2**, 1729–1733.
53 A. Tokranov, B. W. Sheldon, P. Lu, X. Xiao and A. Mukhopadhyay, *J. Electrochem. Soc.*, 2014, **161**, A58–A65.
54 T. Ramireddy, R. Kali, M. K. Jangid, V. Srihari, H. K. Poswal and A. Mukhopadhyay, *J. Electrochem. Soc.*, 2017, **164**, A2360–A2367.
55 R. Kali, S. Badjate and A. Mukhopadhyay, *J. Appl. Electrochem.*, 2017, **47**, 479–486.
56 R. Kali, Y. Krishnan and A. Mukhopadhyay, *Scr. Mater.*, 2017, **130**, 105–109.
57 T. Ichitsubo, S. Yukitani, K. Hirai, S. Yagi, T. Uda and E. Matsubara, *J. Mater. Chem.*, 2011, **21**, 2701–2708.
58 B. W. Sheldon, S. K. Soni, X. Xiao and Y. Qi, *Electrochem. Solid-State Lett.*, 2011, **15**, A9–A11.
59 F. C. Larchè and J. W. Cahn, *Acta Metall.*, 1985, **33**, 331–357.
60 F. Larchè and J. W. Cahn, *Acta Metall.*, 1973, **21**, 1051–1063.
61 K. Zhao, M. Pharr, Q. Wan, W. L. Wang, E. Kaxiras, J. J. Vlassak and Z. Suo, *J. Electrochem. Soc.*, 2012, **159**, A238–A243.
62 H. Xie, W. Qiu, H. Song and J. Tian, *J. Electrochem. Soc.*, 2016, **163**, A2685–A2690.
63 R. Tripuraneni, S. Rakshit and S. P. V. Nadimpalli, *J. Electrochem. Soc.*, 2018, **165**, A2194–A2202.
64 M. Gu, H. Yang, D. E. Perea, J.-G. Zhang, S. Zhang and C.-M. Wang, *Nano Lett.*, 2014, **14**, 4622–4627.
65 J. Pan, Q. Zhang, J. Li, M. J. Beck, X. Xiao and Y.-T. Cheng, *Nano Energy*, 2015, **13**, 192–199.
66 G. Bucci, S. P. V. Nadimpalli, V. A. Sethuraman, A. F. Bower and P. R. Guduru, *J. Mech. Phys. Solids*, 2014, **62**, 276–294.
67 M. Pharr, Y.-S. Choi, D. Lee, K. H. Oh and J. J. Vlassak, *J. Power Sources*, 2016, **304**, 164–169.
68 C.-H. Chen, E. Chason and P. R. Guduru, *J. Electrochem. Soc.*, 2017, **164**, A574–A579.
69 J. Xu, C. Ma, M. Balasubramanian and Y. S. Meng, *Chem. Commun.*, 2014, **3**, 12564–12567.
70 A. R. Armstrong, M. Holzapfel, P. Novak, C. S. Johnson, S.-H. Kang, M. M. Thackeray and P. G. Bruce, *J. Am. Chem. Soc.*, 2006, **128**, 8694–8698.
71 A. Manthiram, J. C. Knight, S.-T. Myung, S.-M. Oh and Y.-K. Sun, *Adv. Energy Mater.*, 2016, **6**, 1501010.
72 P. K. Nayak, E. M. Erickson, F. Schipper, T. R. Penki, N. Munichandraiah, P. Adelhelm, H. Sclar, F. Amalraj, B. Markovsky and D. Aurbach, *Adv. Energy Mater.*, 2018, **8**, 1702397.
73 G. Assat and J.-M. Tarascon, *Nat. Energy*, 2018, **3**, 373–386.

74 R. Jung, M. Metzger, F. Maglia, C. Stinner and H. A. Gasteiger, *J. Electrochem. Soc.*, 2017, **164**, A1361–A1377.
75 S. Mandowara and B. W. Sheldon, *ECS Trans.*, 2008, **11**, 191–196.
76 S. P. V. Nadimpalli, R. Tripuraneni and V. A. Sethuraman, *J. Electrochem. Soc.*, 2015, **162**, A2840–A2846.
77 P. Lian, X. Zhu, S. Liang, Z. Li, W. Yang and H. Wang, *Electrochim. Acta*, 2010, **55**, 3909–3914.
78 D. Sauerteig, S. Ivanov, H. Reinshagen and A. Bund, *J. Power Sources*, 2017, **342**, 939–946.
79 J. Li, A. K. Dozier, Y. Li, F. Yang and Y.-T. Cheng, *J. Electrochem. Soc.*, 2011, **158**, A689–A694.
80 A. Tokranov, R. Kumar, C. Li, S. Minne, X. Xiao and B. W. Sheldon, *Adv. Energy Mater.*, 2016, **6**, 1502302.
81 A. Tokranov, B. W. Sheldon, C. Li, S. Minne and X. Xiao, *ACS Appl. Mater. Interfaces*, 2014, **6**, 6672–6686.
82 Y. He and H. Hu, *Phys. Chem. Chem. Phys.*, 2015, **17**, 23565–23572.
83 L. B. Freund and S. Suresh, *Thin Film Materials: Stress, Defect Formation and Surface Evolution*, Cambridge University Press, Cambridge, UK, 2004.
84 F. X. Hart and J. B. Bates, *J. Appl. Phys.*, 1998, **83**, 7560–7566.
85 J. M. Foster, X. Huang, M. Jiang, S. J. Chapman, B. Protas and G. Richardson, *J. Power Sources*, 2017, **350**, 140–151.
86 X. H. Liu, L. Zhong, S. Huang, S. X. Mao, T. Zhu and J. Y. Huang, *ACS Nano*, 2012, **6**, 1522–1531.
87 K. Zhao, M. Pharr, S. Cai, J. J. Vlassak and Z. Suo, *J. Am. Ceram. Soc.*, 2011, **94**, 226–235.
88 J. Park, W. Lu and A. M. Sastry, *J. Electrochem. Soc.*, 2011, **158**, A201–A206.
89 J. Christensen and J. Newman, *J. Solid State Electrochem.*, 2006, **10**, 293–319.
90 R. E. García, Y.-M. Chiang, W. Craig Carter, P. Limthongkul and C. M. Bishop, *J. Electrochem. Soc.*, 2005, **152**, A255–A263.
91 A. F. Bower, E. Chason, P. R. Guduru and B. W. Sheldon, *Acta Mater.*, 2015, **98**, 229–241.
92 L. Ji and Z. Guo, *Acta Mech. Sin.*, 2018, **34**, 187–198.
93 T. K. Bhandakkar and H. Gao, *Int. J. Solids Struct.*, 2010, **47**, 1424–1434.
94 Y. Hu, X. Zhao and Z. Suo, *J. Mater. Res.*, 2010, **25**, 1007–1010.
95 D. Wang, X. Wu, Z. Wang and L. Chen, *J. Power Sources*, 2005, **140**, 125–128.
96 J. Y. Huang, L. Zhong, C. M. Wang, J. P. Sullivan, W. Xu, L. Q. Zhang, S. X. Mao, N. S. Hudak, X. H. Liu, A. Subramanian, H. Fan, L. Qi, A. Kushima and J. Li, *Science*, 2010, **330**, 1515–1520.
97 A. J. Leenheer, K. L. Jungjohann, K. R. Zavadil and C. T. Harris, *ACS Nano*, 2016, **10**, 5670–5678.
98 G. G. Stoney, *Proc. R. Soc. A*, 1909, **82**, 172–175.
99 X. Feng, Y. Huang and A. J. Rosakis, *J. Appl. Mech.*, 2007, **74**, 1276–1281.
100 W. D. Nix, *Metall. Trans. A*, 1989, **20**, 2217–2245.
101 M. Pharr, Z. Suo and J. J. Vlassak, *Nano Lett.*, 2013, **13**, 5570–5577.
102 K. Zhao, G. A. Tritsaris, M. Pharr, W. L. Wang, O. Okeke, Z. Suo, J. J. Vlassak and E. Kaxiras, *Nano Lett.*, 2012, **12**, 4397–4403.
103 M. Pharr, K. Zhao, X. Wang, Z. Suo and J. J. Vlassak, *Nano Lett.*, 2012, **12**, 5039–5047.
104 H. Xie, Q. Zhang, H. Song, B. Shi and Y. Kang, *J. Power Sources*, 2017, **342**, 896–903.
105 W. Zeng, J. Xing, J. C.-M. Chen, K. Y. S. Ng, K. Oshihara and M. M.-C. Cheng, *Electrochim. Acta*, 2018, **281**, 282–291.
106 H. Tavassol, E. M. C. Jones, N. R. Sottos and A. A. Gewirth, *Nat. Mater.*, 2016, **15**, 1182–1188.
107 Y. Ha, Z. Zeng, C. J. Barile, J. Chang, R. G. Nuzzo, J. Greeley and A. A. Gewirth, *J. Electrochem. Soc.*, 2016, **163**, A2679–A2684.
108 M. Pharr, Z. Suo and J. J. Vlassak, *J. Power Sources*, 2014, **270**, 569–575.
109 X. Xiao, P. Liu, M. W. Verbrugge, H. Haftbaradaran and H. Gao, *J. Power Sources*, 2011, **196**, 1409–1416.
110 D. Li, Y. Wang, J. Hu, B. Lu, Y.-T. Cheng and J. Zhang, *J. Power Sources*, 2017, **366**, 80–85.
111 J. J. Brown, S.-H. Lee, J. Xiao and Z. Wu, *Phys. Status Solidi A*, 2016, **213**, 2156–2168.
112 A. Al-Obeidi, D. Kramer, C. V. Thompson and R. Mönig, *J. Power Sources*, 2015, **297**, 472–480.
113 V. B. Shenoy, P. Johari and Y. Qi, *J. Power Sources*, 2010, **195**, 6825–6830.
114 H. Kim, C.-Y. Chou, J. G. Ekerdt and G. S. Hwang, *J. Phys. Chem. C*, 2011, **115**, 2514–2521.
115 J. Zhang, J. Zhang, D. Wang, X. Xie and B. Xia, *Mater. Lett.*, 2017, **190**, 79–82.
116 S. Rakshit, R. Tripuraneni and S. P. V. Nadimpalli, *Exp. Mech.*, 2018, **58**, 537–547.
117 J. Zhang, J. Zhang, T. Bao, X. Xie and B. Xia, *J. Power Sources*, 2017, **348**, 16–20.
118 M. K. Jangid, S. Sinha, A. S. Lakhnot, F. J. Sonia, A. Kumar, R. O. Dusane and A. Mukhopadhyay, *Electrochim. Acta*, 2019, **297**, 381–391.
119 H. Mukaibo, T. Momma, Y. Shacham-Diamand, T. Osaka and M. Kodaira, *Electrochem. Solid-State Lett.*, 2007, **10**, A70–A73.
120 H. Tavassol, M. W. Cason, R. G. Nuzzo and A. A. Gewirth, *Adv. Energy Mater.*, 2015, **5**, 1400317.
121 E. Peled and S. Menkin, *J. Electrochem. Soc.*, 2017, **164**, A1703–A1719.
122 S. J. An, J. Li, C. Daniel, D. Mohanty, S. Nagpure and D. L. Wood III, *Carbon*, 2016, **105**, 52–76.
123 D. Aurbach, Y. Ein-Eli, O. Chusid, Y. Carmeli, M. Babai and H. Yamin, *J. Electrochem. Soc.*, 1994, **141**, 603–611.
124 L. Mickelson, H. Castro, E. Switzer and C. Friesen, *J. Electrochem. Soc.*, 2014, **161**, A2121–A2127.
125 X. Wang, A. Yang and S. Xia, *J. Electrochem. Soc.*, 2016, **163**, A90–A95.
126 S. P. V. Nadimpalli and R. Tripuraneni, in *Proceedings of the ASME 2015 International Mechanical Engineering Congress and Exposition*, 2015.
127 Z. Choi, D. Kramer and R. Mönig, *J. Power Sources*, 2013, **240**, 245–251.

128 Z. Li, K. Jiang, F. Khan, A. Goswami, J. Liu, A. Passian and T. Thundat, *Sci. Adv.*, 2019, **5**, eaav2820.
129 G. G. Amatucci, J. M. Tarascon and L. C. Klein, *Solid State Ionics*, 1996, **83**, 167–173.
130 M. Inaba, T. Uno and A. Tasaka, *J. Power Sources*, 2005, **146**, 473–477.
131 H. Gabrisch, R. Yazami and B. Fultz, *Electrochem. Solid-State Lett.*, 2002, **5**, A111–A114.
132 G. Chen, X. Song and T. J. Richardson, *Electrochem. Solid-State Lett.*, 2006, **9**, A295–A298.
133 Z. Xu, M. M. Rahman, L. Mu, Y. Liu and F. Lin, *J. Mater. Chem. A*, 2018, **6**, 21859–21884.
134 S. Xia, L. Mu, Z. Xu, J. Wang, C. Wei, L. Liu, P. Pianetta, K. Zhao, X. Yu, F. Lin and Y. Liu, *Nano Energy*, 2018, **53**, 753–762.
135 L. Mu, R. Lin, R. Xu, L. Han, S. Xia, D. Sokaras, J. D. Steiner, T. C. Weng, D. Nordlund, M. M. Doeff, Y. Liu, K. Zhao, H. L. Xin and F. Lin, *Nano Lett.*, 2018, **18**, 3241–3249.
136 Y. Zhang, Y. Luo, C. Fincher, S. McProuty, G. Swenson, S. Banerjee and M. Pharr, *Energy Storage Mater.*, 2019, **16**, 491–497.
137 E. Peled, D. Golodnitsky, A. Ulus and V. Yufit, *Electrochim. Acta*, 2004, **50**, 391–395.
138 H. Xie, H. Song, J.-g. Guo, Y. Kang, W. Yang and Q. Zhang, *Carbon*, 2019, **144**, 342–350.
139 K. Edström, T. Gustafsson and J. O. Thomas, *Electrochim. Acta*, 2004, **50**, 397–403.
140 G. Cherkashinin, K. Nikolowski, H. Ehrenberg, S. Jacke, L. Dimesso and W. Jaegermann, *Phys. Chem. Chem. Phys.*, 2012, **14**, 12321–12331.
141 S. Fang, D. Jackson, M. L. Dreibelbis, T. F. Kuech and R. J. Hamers, *J. Power Sources*, 2018, **373**, 184–192.
142 X. H. Liu, H. Zheng, L. Zhong, S. Huang, K. Karki, L. Q. Zhang, Y. Liu, A. Kushima, W. T. Liang, J. W. Wang, J. H. Cho, E. Epstein, S. A. Dayeh, S. T. Picraux, T. Zhu, J. Li, J. P. Sullivan, J. Cumings, C. Wang, S. X. Mao, Z. Z. Ye, S. Zhang and J. Y. Huang, *Nano Lett.*, 2011, **11**, 3312–3318.
143 M. T. McDowell, I. Ryu, S. W. Lee, C. Wang, W. D. Nix and Y. Cui, *Adv. Mater.*, 2012, **24**, 6034–6041.
144 M. T. McDowell, S. W. Lee, J. T. Harris, B. A. Korgel, C. Wang, W. D. Nix and Y. Cui, *Nano Lett.*, 2013, **13**, 758–764.
145 C.-M. Wang, X. Li, Z. Wang, W. Xu, J. Liu, F. Gao, L. Kovarik, J.-G. Zhang, J. Howe, D. J. Burton, Z. Liu, X. Xiao, S. Thevuthasan and D. R. Baer, *Nano Lett.*, 2012, **12**, 1624–1632.
146 M. Gu, Y. Li, X. Li, S. Hu, X. Zhang, W. Xu, S. Thevuthasan, D. R. Baer, J.-G. Zhang, J. Liu and C. Wang, *ACS Nano*, 2012, **6**, 8439–8447.
147 C.-M. Wang, W. Xu, J. Liu, J.-G. Zhang, L. V. Saraf, B. W. Arey, D. Choi, Z.-G. Yang, J. Xiao, S. Thevuthasan and D. R. Baer, *Nano Lett.*, 2011, **11**, 1874–1880.
148 L. Wang, Z. Xu, S. Yang, X. Tian, J. Wei, W. Wang and X. Bai, *Sci. China: Technol. Sci.*, 2013, **56**, 2630–2635.
149 Q. Li, P. Wang, Q. Feng, M. Mao, J. Liu, S. X. Mao and H. Wang, *Chem. Mater.*, 2014, **26**, 4102–4108.
150 Y. Liu, N. S. Hudak, D. L. Huber, S. J. Limmer, J. P. Sullivan and J. Y. Huang, *Nano Lett.*, 2011, **11**, 4188–4194.
151 X. Lu, E. R. Adkins, Y. He, L. Zhong, L. Luo, S. X. Mao, C.-M. Wang and B. A. Korgel, *Chem. Mater.*, 2016, **28**, 1236–1242.
152 M. Zhang, K. Yin, Z. D. Hood, Z. Bi, C. A. Bridges, S. Dai, Y. S. Meng, M. P. Paranthaman and M. Chi, *J. Mater. Chem. A*, 2017, **5**, 20651–20657.
153 S. J. Kim, S. Y. Noh, A. Kargar, D. Wang, G. W. Graham and X. Pan, *Chem. Commun.*, 2014, **50**, 9932–9935.
154 Y.-T. Cheng and M. W. Verbrugge, *J. Power Sources*, 2009, **190**, 453–460.
155 K.-J. Zhao, Y.-G. Li and L. Brassart, *Acta Mech. Sin.*, 2013, **29**, 379–387.
156 K. J. Rhodes, R. Meisner, M. Kirkham, N. Dudney and C. Daniel, *J. Electrochem. Soc.*, 2012, **159**, A294–A299.
157 J. W. Wang, X. H. Liu, S. X. Mao and J. Y. Huang, *Nano Lett.*, 2012, **12**, 5897–5902.
158 X. H. Liu, S. Huang, S. T. Picraux, J. Li, T. Zhu and J. Y. Huang, *Nano Lett.*, 2011, **11**, 3991–3997.
159 Z. Yang, P.-V. Ong, Y. He, L. Wang, M. E. Bowden, W. Xu, T. C. Droubay, C. Wang, P. V. Sushko and Y. Du, *Small*, 2018, **14**, 1803108.
160 S. Hwang, S. M. Kim, S.-M. Bak, S. Y. Kim, B.-W. Cho, K. Y. Chung, J. Y. Lee, E. A. Stach and W. Chang, *Chem. Mater.*, 2015, **27**, 3927–3935.
161 O. M. Karakulina, A. Demortière, W. Dachraoui, A. M. Abakumov and J. Hadermann, *Nano Lett.*, 2018, **18**, 6286–6291.
162 B. Wei, X. Lu, F. Voisard, H. Wei, H.-c. Chiu, Y. Ji, X. Han, M. L. Trudeau, K. Zaghib, G. P. Demopoulos and R. Gauvin, *ACS Appl. Energy Mater.*, 2018, **1**, 3180–3189.
163 D. Aurbach and Y. Cohen, *J. Electrochem. Soc.*, 1996, **143**, 3525–3532.
164 L. Y. Beaulieu, V. K. Cumyn, K. W. Eberman, L. J. Krause and J. R. Dahn, *Rev. Sci. Instrum.*, 2001, **72**, 3313–3319.
165 L. Y. Beaulieu, T. D. Hatchard, A. Bonakdarpour, M. D. Fleischauer and J. R. Dahn, *J. Electrochem. Soc.*, 2003, **150**, A1457–A1464.
166 L. Y. Beaulieu, S. D. Beattie, T. D. Hatchard and J. R. Dahn, *J. Electrochem. Soc.*, 2003, **150**, A419–A424.
167 C. R. Becker, K. E. Strawhecker, Q. P. McAllister and C. a. Lundgren, *ACS Nano*, 2013, **7**, 9173–9182.
168 B. Jerliu, E. Hüger, L. Dörrer, B. K. Seidlhofer, R. Steitz, V. Oberst, U. Geckle, M. Bruns and H. Schmidt, *J. Phys. Chem. C*, 2014, **118**, 9395–9399.
169 Y. He, X. Yu, G. Li, R. Wang, H. Li, Y. Wang, H. Gao and X. Huang, *J. Power Sources*, 2012, **216**, 131–138.
170 L. Y. Beaulieu, K. W. Eberman, R. L. Turner, L. J. Krause and J. R. Dahn, *Electrochem. Solid-State Lett.*, 2001, **4**, A137–A140.
171 R. Kumar, A. Tokranov, B. W. Sheldon, X. Xiao, Z. Huang, C. Li and T. Mueller, *ACS Energy Lett.*, 2016, **1**, 689–697.
172 B. Breitung, P. Baumann, H. Sommer, J. Janek and T. Brezesinski, *Nanoscale*, 2016, **8**, 14048–14056.
173 I. T. Lucas, E. Pollak and R. Kostecki, *Electrochem. Commun.*, 2009, **11**, 2157–2160.

174 K. A. Hirasawa, T. Sato, H. asahina, S. Yamaguchi and S. Mori, *J. Electrochem. Soc.*, 2006, **144**, L81–L84.
175 F. Single, B. Horstmann and A. Latz, *J. Electrochem. Soc.*, 2017, **164**, E3132–E3145.
176 S. J. Harris and P. Lu, *J. Phys. Chem. C*, 2013, **117**, 6481–6492.
177 P. Lu, C. Li, E. W. Schneider and S. J. Harris, *J. Phys. Chem. C*, 2014, **118**, 896–903.
178 M. Steinhauer, M. Stich, M. Kurniawan, B.-K. Seidlhofer, M. Trapp, A. Bund, N. Wagner and K. A. Friedrich, *ACS Appl. Mater. Interfaces*, 2017, **9**, 35794–35801.
179 F. P. Campana, R. Kötz, J. Vetter, P. Novák and H. Siegenthaler, *Electrochem. Commun.*, 2005, **7**, 107–112.
180 J. Park, S. Kalnaus, S. Han, Y. K. Lee, G. B. Less, N. J. Dudney, C. Daniel and A. M. Sastry, *J. Power Sources*, 2013, **222**, 417–425.
181 E.-J. Lee, Z. Chen, H.-J. Noh, S. C. Nam, S. Kang, D. H. Kim, K. Amine and Y.-K. Sun, *Nano Lett.*, 2014, **14**, 4873–4880.
182 S. Kobi and A. Mukhopadhyay, *J. Eur. Ceram. Soc.*, 2018, **38**, 4707–4718.
183 W. Zhu, Y. Wang, D. Liu, V. Gariépy, C. Gagnon, A. Vijh, M. Trudeau and K. Zaghib, *Energies*, 2018, **11**, 2963.
184 M. Morcrette, Y. Chabre, G. Vaughan, G. Amatucci, J. Leriche, S. Patoux, C. Masquelier and J.-M. Tarascon, *Electrochim. Acta*, 2002, **47**, 3137–3149.
185 F. J. Q. Cortes, M. G. Boebinger, M. Xu, A. Ulvestad and M. T. McDowell, *ACS Energy Lett.*, 2018, **3**, 349–355.
186 T. Alemu and F.-M. Wang, *J. Synchrotron Radiat.*, 2018, **25**, 151–165.
187 A. H. Whitehead, K. Edström, N. Rao and J. R. Owen, *J. Power Sources*, 1996, **63**, 41–45.
188 T. D. Hatchard and J. R. Dahn, *J. Electrochem. Soc.*, 2004, **151**, A838–A842.
189 I. A. Courtney and J. R. Dahn, *J. Electrochem. Soc.*, 1997, **144**, 2045–2052.
190 J. Li and J. R. Dahn, *J. Electrochem. Soc.*, 2007, **154**, A156–A161.
191 S. Misra, N. Liu, J. Nelson, S. S. Hong, Y. Cui and M. F. Toney, *ACS Nano*, 2012, **6**, 5465–5473.
192 N. Oehl, G. Schmuelling, M. Knipper, R. Kloepsch, T. Placke, J. Kolny-Olesiak, T. Plaggenborg, M. Winter and J. Parisi, *CrystEngComm*, 2015, **17**, 8500–8504.
193 H. S. Bhardwaj, T. Ramireddy, A. Pradeep, M. K. Jangid, V. Srihari, H. K. Poswal and A. Mukhopadhyay, *ChemElectroChem*, 2018, **5**, 1219–1229.
194 J. N. Reimer and J. R. Dahn, *J. Electrochem. Soc.*, 1992, **139**, 2091–2097.
195 H. He, C. Huang, C.-W. Luo, J.-J. Liu and Z.-S. Chao, *Electrochim. Acta*, 2013, **92**, 148–152.
196 N. A. Cañas, P. Einsiedel, O. T. Freitag, C. Heim, M. Steinhauer, D.-W. Park and K. A. Friedrich, *Carbon*, 2017, **116**, 255–263.
197 A. Darwiche, C. Marino, M. T. Sougrati, B. Fraisse, L. Stievano and L. Monconduit, *J. Am. Chem. Soc.*, 2012, **134**, 20805–20811.
198 A. Darwiche, M. T. Sougrati, B. Fraisse, L. Stievano and L. Monconduit, *Electrochem. Commun.*, 2013, **32**, 18–21.
199 M. Fehse, M. T. Sougrati, A. Darwiche, V. Gabaudan, C. L. Fontaine, L. Monconduit and L. Stievano, *J. Mater. Chem. A*, 2018, **6**, 8724–8734.
200 J. Qin, T. Wang, D. Liu, E. Liu, N. Zhao, C. Shi, F. He, L. Ma and C. He, *Adv. Mater.*, 2018, **30**, 1704670.
201 W. Li, H. Y. Asl, Q. Xie and A. Manthiram, *J. Am. Chem. Soc.*, 2019, **141**, 5097–5101.
202 K. Ishidzu, Y. Oka and T. Nakamura, *Solid State Ionics*, 2016, **288**, 176–179.
203 J. Li, R. Shunmugasundaram, R. Doig and J. R. Dahn, *Chem. Mater.*, 2016, **28**, 162–171.
204 H. Li, M. Cormier, N. Zhang, J. Inglis, J. Li and J. R. Dahn, *J. Electrochem. Soc.*, 2019, **166**, A429–A439.
205 Q. Xie, W. Li and A. Manthiram, *Chem. Mater.*, 2019, **31**, 938–946.
206 N. Tapia-Ruiz, W. M. Dose, N. Sharma, H. Chen, J. Heath, J. W. Somerville, U. Maitra, M. S. Islam and P. G. Bruce, *Energy Environ. Sci.*, 2018, **11**, 1470–1479.
207 X. Li, Y. Wang, D. Wu, L. Liu, S.-H. Bo and G. Ceder, *Chem. Mater.*, 2016, **28**, 6575–6583.
208 D. Sehrawat, S. Cheong, A. Rawal, A. M. Glushenkov, H. E. A. Brand, B. Cowie, E. Gonzalo, T. Rojo, P. J. P. Naeyaert, C. D. Ling, M. Avdeev and N. Sharma, *CrystEngComm*, 2019, **21**, 172–181.
209 P.-F. Wang, H.-R. Yao, X.-Y. Liu, J.-N. Zhang, L. Gu, X.-Q. Yu, Y.-X. Yin and Y.-G. Guo, *Adv. Mater.*, 2017, **29**, 1700210.
210 L. Wang, Y.-G. Sun, L.-L. Hu, J.-Y. Piao, J. Guo, A. Manthiram, J. Ma and A.-M. Cao, *J. Mater. Chem. A*, 2017, **5**, 8752–8761.
211 K. Kubota, Y. Yoda and S. Komaba, *J. Electrochem. Soc.*, 2017, **164**, A2368–A2373.
212 A. O. Kondrakov, H. Geßwein, K. Galdina, L. de Biasi, V. Meded, E. O. Filatova, G. Schumacher, W. Wenzel, P. Hartmann, T. Brezesinski and J. Janek, *J. Phys. Chem. C*, 2017, **121**, 24381–24388.
213 H. Kang, Y. Liu, K. Cao, Y. Zhao, L. Jiao, Y. Wang and H. Yuan, *J. Mater. Chem. A*, 2015, **3**, 17899–17913.
214 E. Irisarri, A. Ponrouch and M. R. Palacin, *J. Electrochem. Soc.*, 2015, **162**, A2476–A2482.
215 Z. Zeng, N. Liu, Q. Zeng, S. W. Lee, W. L. Mao and Y. Cui, *Nano Energy*, 2016, **22**, 105–110.
216 S. Tardif, E. Pavlenko, L. Quazuguel, M. Boniface, M. Maréchal, J.-S. Micha, L. Gonon, V. Mareau, G. Gebel, P. Bayle-Guillemaud, F. Rieutord and S. Lyonnard, *ACS Nano*, 2017, **11**, 11306–11316.
217 A. Krause, O. Tkacheva, A. Omar, U. Langklotz, L. Giebeler, S. Dörfler, F. Fauth, T. Mikolajick and W. M. Weber, *J. Electrochem. Soc.*, 2019, **166**, A5378–A5385.
218 D. Liu, Y. Wang, Y. Xie, L. He, J. Chen, K. Wu, R. Xu and Y. Gao, *J. Power Sources*, 2013, **232**, 29–33.
219 H. Jung, K. Gerasopoulos, A. A. Talin and R. Ghodssi, *Electrochim. Acta*, 2017, **242**, 227–239.
220 H. Jung, K. Gerasopoulos, A. A. Talin and R. Ghodssi, *J. Power Sources*, 2017, **340**, 89–97.
221 J. Lei, F. McLarnon and R. Kostecki, *J. Phys. Chem. B*, 2005, **109**, 952–957.

222 Q. Shi, Y. Takahashi, J. Akimoto, I. C. Stefan and D. A. Scherson, *Electrochem. Solid-State Lett.*, 2005, **8**, 521–524.
223 T. Nishi, H. Nakai and A. Kita, *J. Electrochem. Soc.*, 2013, **160**, 1785–1788.
224 Y. Qi and S. J. Harris, *J. Electrochem. Soc.*, 2010, **157**, A741–A747.
225 J. Chen, A. K. Thapa and T. A. Berfield, *J. Power Sources*, 2014, **271**, 406–413.
226 C. Dai, C. Li, H. Huang, Z. Wang, X. Zhu, X. Liao, X. Chen, Y. Pan and D. Fang, *Solid State Ionics*, 2019, **331**, 56–65.
227 J. Luo, C. Y. Dai, Z. Wang, K. Liu, W. G. Mao, D. N. Fang and X. Chen, *Measurement*, 2016, **94**, 759–770.
228 W. Mao, Z. Wang, C. Li, X. Zhu, C. Dai, H. Yang, X. Chen and D. Fang, *J. Power Sources*, 2018, **402**, 272–280.
229 Z. Wang, H. Huang, L. Zeng, Y. Wang, L. Lv, C. Dai, W. Mao, X. Chen and D. Fang, *Electrochim. Acta*, 2019, **305**, 101–115.
230 F. Orsini, A. Du Pasquier, B. Beaudoin, J. M. Tarascon, M. Trentin, N. Langenhuizen, E. De Beer and P. Notten, *J. Power Sources*, 1998, **76**, 19–29.
231 A. Mukhopadhyay and M. K. Jangid, *Science*, 2018, **359**, 1463.
232 M. Golozar, P. Hovington, A. Paolella, S. Bessette, M. Lagacé, P. Bouchard, H. Demers, R. Gauvin and K. Zaghib, *Nano Lett.*, 2018, **18**, 7583–7589.
233 C.-Y. Chen, T. Sano, T. Tsuda, K. Ui, Y. Oshima, M. Yamagata, M. Ishikawa, M. Haruta, T. Doi, M. Inaba and S. Kuwabata, *Sci. Rep.*, 2016, **6**, 36153.
234 P. Hovington, M. Dontigny, A. Guerfi, J. Trottier, M. Lagacé, A. Mauger, C. M. Julien and K. Zaghib, *J. Power Sources*, 2014, **248**, 457–464.
235 H. Shi, X. Liu, R. Wu, Y. Zheng, Y. Li, X. Cheng, W. Pfleging and Y. Zhang, *Appl. Sci.*, 2019, **9**, 956.
236 A. Bordes, E. De Vito, C. Haon, A. Boulineau, A. Montani and P. Marcus, *Chem. Mater.*, 2016, **28**, 1566–1573.
237 X. Zhou, T. Li, Y. Cui, Y. Fu, Y. Liu and L. Zhu, *ACS Appl. Mater. Interfaces*, 2019, **11**, 1733–1738.
238 D. Chen, S. Indris, M. Schulz, B. Gamer and R. Mönig, *J. Power Sources*, 2011, **196**, 6382–6387.
239 J. McBreen, W. E. O'Grady and K. I. Pandya, *J. Power Sources*, 1988, **22**, 323–340.
240 C. Dräger, F. Sigel, R. Witte, R. Kruk, L. Pfaffmann, S. Mangold, V. Mereacre, M. Knapp, H. Ehrenbergad and S. Indrisad, *Phys. Chem. Chem. Phys.*, 2019, **21**, 89–95.
241 M. Balasubramanian, X. Sun, X. Q. Yang and J. McBreen, *J. Electrochem. Soc.*, 2000, **147**, 2903–2909.
242 J. Xu, M. Sun, R. Qiao, S. E. Renfrew, L. Ma, T. Wu, S. Hwang, D. Nordlund, D. Su, K. Amine, J. Lu, B. D. McCloskey, W. Yang and W. Tong, *Nat. Commun.*, 2018, **9**, 947.
243 M. G. Kim, H. J. Shin, J.-H. Kim, S.-H. Park and Y.-K. Sun, *J. Electrochem. Soc.*, 2005, **152**, A1320–A1328.
244 Y. W. Tsai, B. J. Hwang, G. Ceder, H. S. Sheu, D. G. Liu and J. F. Lee, *Chem. Mater.*, 2005, **17**, 3191–3199.
245 F. Lin, I. M. Markus, D. Nordlund, T.-C. Weng, M. D. Asta, H. L. Xin and M. M. Doeff, *Nat. Commun.*, 2014, **5**, 1–9.
246 C. Ma, J. Alvarado, J. Xu, R. J. Clément, M. Kodur, W. Tong, C. P. Grey and Y. S. Meng, *J. Am. Chem. Soc.*, 2017, **139**, 4835–4845.
247 B. M. de Boisse, S. -i. Nishimura, E. Watanabe, L. Lander, A. Tsuchimoto, J. Kikkawa, E. Kobayashi, D. Asakura, M. Okubo and A. Yamada, *Adv. Energy Mater.*, 2018, **8**, 1800409.
248 Z. Shadike, E. Zhao, Y.-N. Zhou, X. Yu, Y. Yang, E. Hu, S. Bak, L. Gu and X.-Q. Yang, *Adv. Energy Mater.*, 2018, **8**, 1702588.
249 J. R. Mueller-Neuhaus, R. A. Dunlap and J. R. Dahn, *J. Electrochem. Soc.*, 2000, **147**, 3598–3605.
250 P. Barpanda, M. Ati, B. C. Melot, G. Rousse, J.-N. Chotard, M.-L. Doublet, M. T. Sougrati, S. A. Corr, J.-C. Jumas and J.-M. Tarascon, *Nat. Mater.*, 2011, **10**, 772–779.
251 K. K. Halankar, B. P. Mandal, M. K. Jangid, A. Mukhopadhyay, S. S. Meena, R. Acharya and A. K. Tyagi, *RSC Adv.*, 2018, **8**, 1140–1147.
252 A. Yamada, S. C. Chung and K. Hinokuma, *J. Electrochem. Soc.*, 2001, **148**, A224–A229.
253 E. McCalla, A. S. Prakash, E. Berg, M. Saubanère, A. M. Abakumov, D. Foix, B. Klobes, M.-T. Sougrati, G. Rousse, F. Lepoivre, S. Mariyappan, M.-L. Doublet, D. Gonbeau, P. Novak, G. V. Tendeloo, R. P. Hermann and J.-M. Tarascon, *J. Electrochem. Soc.*, 2015, **162**, A1341–A1351.
254 A. Aboulaich, F. Robert, P. E. Lippens, L. Aldon, J. Olivier-Fourcade, P. Willmann and J.-C. Jumas, *Hyperfine Interact.*, 2006, **167**, 733–738.
255 K. K. D. Ehinon, S. Naille, R. Dedryvère, P.-E. Lippens, J.-C. Jumas and D. Gonbeau, *Chem. Mater.*, 2008, **20**, 5388–5398.
256 R. A. Dunlap, O. Mao and J. R. Dahn, *Phys. Rev. B*, 1999, **59**, 3494–3500.
257 I. Sandua, T. Broussea, D. M. Schleicha and M. Danot, *J. Solid State Chem.*, 2004, **177**, 4332–4340.
258 V. Gabaudan, R. Berthelot, M. T. Sougrati, P.-E. Lippens, L. Monconduit and L. Stievano, *J. Mater. Chem. A*, 2019, **7**, 15262–15270.
259 H. Pan, J. Zhang, Y. Chen, X. Zhuo and Y. Yang, *Thin Solid Films*, 2010, **519**, 778–783.
260 L. S. de Vasconcelos, R. Xu and K. Zhao, *J. Electrochem. Soc.*, 2017, **164**, A3840–A3847.
261 K. Zhao, W. L. Wang, J. Gregoire, M. Pharr, Z. Suo, J. J. Vlassak and E. Kaxiras, *Nano Lett.*, 2011, **11**, 2962–2967.
262 J. H. Ryu, J. W. Kim, Y.-E. Sung and S. M. Oh, *Electrochem. Solid-State Lett.*, 2004, **7**, A306–A309.
263 M. Gu, L. R. Parent, B. L. Mehdi, R. R. Unocic, M. T. McDowell, R. L. Sacci, W. Xu, J. G. Connell, P. Xu, P. Abellan, X. Chen, Y. Zhang, D. E. Perea, J. E. Evans, L. J. Lauhon, J.-G. Zhang, J. Liu, N. D. Browning, Y. Cui, I. Arslan and C.-M. Wang, *Nano Lett.*, 2013, **13**, 6106–6112.
264 J. H. Yang, J. C. M. Chen and M. M. C. Cheng, *Transducers*, Barcelona, 2013.
265 A. Al-Obeidi, D. Kramer, S. T. Boles, R. Mönig and C. V. Thompson, *Appl. Phys. Lett.*, 2016, **109**, 071902.

266 H. Xie, Y. Kang, H. Song and Q. Zhang, *J. Power Sources*, 2019, **424**, 100–107.
267 B. W. Sheldon and A. Tokranov, *Extreme Mech. Lett.*, 2016, **9**, 379–385.
268 C. Shen, M. Ge, L. Luo, X. Fang, Y. Liu, A. Zhang, J. Rong, C. Wang and C. Zhou, *Sci. Rep.*, 2016, **6**, 31334.
269 X. H. Liu, L. Q. Zhang, L. Zhong, Y. Liu, H. Zheng, J. W. Wang, J.-H. Cho, S. A. Dayeh, S. T. Picraux, J. P. Sullivan, S. X. Mao, Z. Z. Ye and J. Y. Huang, *Nano Lett.*, 2011, **11**, 2251–2258.
270 Y.-M. Chiang, *Science*, 2010, **330**, 1485.
271 L. Wang, Z. Xu, S. Yang, X. Tian, J. Wei, W. Wang and X. Bai, *Sci. China: Technol. Sci.*, 2013, **56**, 2630–2635.
272 C. Shen, S. Wang, Y. Jin and W.-Q. Han, *ACS Appl. Mater. Interfaces*, 2015, **7**, 25441–25447.
273 X. Deng, X. Liu, H. Yan, D. Wang and L. Wan, *Sci. China: Chem.*, 2014, **57**, 178–183.
274 M. Inaba, S.-K. Jeong and Z. Ogumi, *Electrochem. Soc. Interface*, 2011, **20**, 55–59.
275 L. Wang, D. Deng, L. C. Lev and S. Ng, *J. Power Sources*, 2014, **265**, 140–148.
276 R. Vidu, F. T. Quinlan and P. Stroeve, *Ind. Eng. Chem. Res.*, 2002, **41**, 6546–6554.
277 Ö. Ö. Çapraz, S. Rajput, S. White and N. R. Sottos, *Exp. Mech.*, 2018, **58**, 561–571.
278 N. E. Drewett, I. M. Aldous, J. Zou and L. J. Hardwick, *Electrochim. Acta*, 2017, **247**, 296–305.
279 C. M. Burba and R. Frech, *Appl. Spectrosc.*, 2006, **60**, 490–493.
280 M. Motoyama, M. Ejiri, T. Yamamoto and Y. Iriyama, *J. Electrochem. Soc.*, 2018, **165**, A1338–A1347.
281 C.-Y. Tang and S. J. Dillon, *J. Electrochem. Soc.*, 2016, **163**, A1660–A1665.
282 T. Sui, B. Song, J. Dluhos, L. Lu and A. M. Korsunsky, *Nano Energy*, 2015, **17**, 254–260.
283 B. Song, T. Sui, S. Ying, L. Li, L. Lu and A. M. Korsunsky, *J. Mater. Chem. A*, 2015, **3**, 18171–18179.
284 J. Z. Lee, T. A. Wynn, Y. S. Meng and D. Santhanagopalan, *J. Visualized Exp.*, 2018, **133**, e56259.
285 X. Zhou, T. Li, Y. Cui, M. L. Meyerson, C. B. Mullins, Y. Liu and L. Zhu, *ACS Appl. Energy Mater.*, 2019, **2**, 2441–2446.
286 E. Strelcov, J. Cothren, D. Leonard, A. Y. Borisevich and A. Kolmakov, *Nanoscale*, 2015, **7**, 3022–3027.
287 B. E. Wilson, W. H. Smyrl and A. Stein, *J. Electrochem. Soc.*, 2014, **161**, A700–A703.
288 Z. Yang, L. Trahey, Y. Ren, M. K. Y. Chan, C. Lin, J. Okasinski and M. M. Thackeray, *J. Mater. Chem. A*, 2015, **3**, 7389–7398.
289 T. Nonaka, H. Kawaura, Y. Makimura, Y. F. Nishimura and K. Dohmae, *J. Power Sources*, 2019, **419**, 203–207.